$\Lambda^\circ$ POLARIZATION IN $pp \rightarrow p\Lambda^\circ K^+\left(\pi^+\pi^-\right)^N$, $N = 1,2,3,4$ , AT 27.5 $GeV$

A Dissertation

B y

JULIAN FELIX-VALDEZ

Submitted to the Instituto de Física

Universidad de Guanajuato

In partial fulfillment of the requirements for the degree of

DOCTOR OF PHILOSOPHY

December 1993
University of Massachusetts, Amherst MA, USA

$\Lambda^{\bullet}$ POLARIZATION IN $pp \to p\Lambda^{\bullet}\mathrm{K}^+\left(\pi^+\pi^-\right)^N$, $N=1,2,3,4$, AT 27.5 *GeV*

A Dissertation

By

JULIAN FELIX-VALDEZ

Approved as to style and content by:

**Michael N. Kreisler-Chair**
Professor of Physics
University of Massachusetts
Amherst, MA, USA

**Octavio Obregón**
Professor of Physics
Universidad de GTO.
León, GTO. MEXICO

**Angel Dacal**
Professor of Physics
UNAM
México D.F. MEXICO

**Edward P. Hartouni**
Assistant Professor of Physics
University of Massachusetts
Amherst, MA, USA

**Gerardo Moreno**
Assistant Professor of Physics
Universidad de GTO.
León, GTO. MEXICO

**José Luis Lucio**
Professor of Physics
Universidad de GTO.
Leon, GTO. MEXICO

**Luis Villaseñor**
Assistant Professor of Physics
UMSNH
Morelia, Mich. MEXICO

December 1993

iii

$\Lambda^\circ$ POLARIZATION IN $pp \to p\Lambda^\circ K^+\left(\pi^+\pi^-\right)^N$, $N=1,2,3,4$, AT 27.5 $GeV$

A Dissertation

By

JULIAN FELIX-VALDEZ

Approved as to style and content by:

Michael N. Kreisler-Chair
Professor of Physics
University of Massachusetts
Amherst, MA, USA

Octavio Obregón
Professor of Physics
Universidad de GTO.
León, GTO. MEXICO

Angel Dacal
Professor of Physics
UNAM
México D.F. MEXICO

Edward P. Hartouni
Assistant Professor of Physics
University of Massachusetts
Amherst, MA, USA

Gerardo Moreno
Assistant Professor of Physics
Universidad de GTO.
León, GTO. MEXICO

José Luis Lucio
Professor of Physics
Universidad de GTO.
Leon, GTO. MEXICO

Luis Villaseñor
Assistant Professor of Physics
UMSNH
Morelia, Mich. MEXICO

December 1993

iii

# ABSTRACT

Since most studies of $\Lambda^0$ polarization have involved $\Lambda^0$'s produced inclusively, little is known about the contributions to the polarization from specific final states. In order to study this aspect of the polarization phenomenon, we measured $\Lambda^0$ polarization in the exclusive final states $pp \rightarrow p\Lambda^0 K^+(\pi^+\pi^-)^N$, $N = 1, 2, 3, 4$, at $27.5\,GeV$. We measured the polarization as a function of the transverse momentum of the $\Lambda^0$ $(P_r)$ and as a function of the longitudinal momentum of the $\Lambda^0$ in the center of mass of event $(P_z)$. We have observed a striking dependence of the sign of the polarization on $P_z$. $\Lambda^0$'s with $P_z > 0$ had polarization, as a function of the transverse momentum, that agrees with inclusive polarization measurements. However, for $P_z < 0$, in the final states with $N = 1$ and $N = 2$, there is a surprising change in the sign of the polarization. The $\Lambda^0$'s in this kinematic region have a polarization which is mirror symmetric to that of $\Lambda^0$'s with $P_z > 0$. We discuss this observation in detail. Another surprise was revealed when the analysis in the $P_z < 0$ region was extended to the final states with $N = 3$ and $N = 4$. In that region, the $\Lambda^0$'s do not seem to be polarized. These observations are the first showing a kinematic dependence of the phenomenon. The effect is most likely due to the difficulty in determining which interacting proton produced the $\Lambda^0$ at high multiplicities.

For final states with $N = 2$, we examined also $\Lambda^0$ polarization as a function of various kinematic relationships and as a function of the invariant mass of the $\Lambda K$, $\Lambda K(\pi^+\pi^-)$, and $\Lambda K 2(\pi^+\pi^-)$ systems. We studied the effect, on the observed polarization, due to $\Lambda^0$'s not produced directly in the proton

proton collision, i.e., those $\Lambda^0$'s which were the decay products of another particle (the $\Sigma^0$) or a resonance ($\Sigma^{*-}$, and the $\Sigma^{*+}$).

# ACKNOWLEDGMENTS

It seems impossible to thank all the persons and all the institutions involved with this thesis research. They constitute a very delicate human machinery, where each part, human or Institution, played an inestimable role. As human beings, we are very complex. Therefore Physics is a deep and complex human activity, where a collage of hopes, ups, and downs are involved. Encouraging words, helpful hands, and money are inevitable necessities. They came from many philanthropists and altruist persons outside or inside key institutions. I'll mention thanks for all of them from a historical point of view, i.e., as my development occurred.

This trek began in Cd. Obregón Sonora, México. The support was from **Dora Elia García de Fuller, Irma Beatriz Enciso de Espinoza,** and **Beatriz Marina Bours de Pineda.** These three wonderful women were central to my early development. I thank them and their respective families. I thank also the **Bours-Muñoz** family from the same home city. From this city, I thank **ICE del Estado de Sonora México.** I appreciate the support from its Director, **Cecilia Miloslavish,** and from its last Director, Mrs. **Concepción Valencia Fontes de Encinas.**

Second and later on, in the Instituto de Física, Universidad de Guanajuato, México, I received help from the late **Dr. C. Avilez V.** Thanks to him wherever he is now.

# TABLE OF CONTENTS

xiii

# LIST OF TABLES

# LIST OF FIGURES

# CHAPTER 1

## INTRODUCTION

### 1.1   Foreword

Because the spin of the $\Lambda^0$ hyperon is not zero, $\Lambda^0$ hyperons can be created with their spins pointing statistically in a certain direction. It would seem impossible to make a measurement of the existence of such a phenomenon since spin is not easy to observe. But because $\Lambda^0$ decays weakly into $p$ and $\pi^-$, we can use the weak decay process, which does not conserve parity, to determine $\Lambda^0$ polarization, where the polarization of a particle is the expectation value of its spin along a particular axis.

The existence of $\Lambda^0$ polarization in high energy collisions was first observed by A. Lesnik et al. [1] in the channel $p + p \rightarrow \Lambda^0 + X$ at 6 $GeV$ at Argonne National Laboratory in 1975. The same year, G. Bunce et al. [2] observed significant polarization in the channel $p + Be \rightarrow \Lambda^0 + X$ at 300 $GeV$ at Fermilab, where both the beam proton and the target proton were unpolarized. These results contradicted the intuitive picture that spin plays an unimportant role in high energy hadron production processes. It had been thought that since high energy collisions involve many final state particles, no coherent interference of amplitudes would be possible. Therefore, no polarization would be present. The existence of polarization in channels such as $p + nucleus \rightarrow \Lambda^0 + X$ may reflect a certain simplicity in the particle

1

production process. Because polarization requires coherence between at least two spin-dependent amplitudes, its existence suggests that only a few amplitudes contribute to the production process. If this is true, $\Lambda^0$ polarization measurements constitute a delicate probe of reaction dynamics.

Since $\Lambda^0$ polarization was discovered, there have been many experiments studying the polarization phenomenon [3,...,14]. There has also been theoretical activity trying to explain this phenomenon and attempting to understand the sources of polarization [15,...,19]. Unfortunately, there is not a simple explanation of the origin of $\Lambda^0$ polarization, despite the enormous theoretical activity.

Most of the experimental studies of $\Lambda^0$ polarization have investigated $\Lambda^0$'s produced inclusively. These studies use any $\Lambda^0$ produced in a high energy proton-target collision independently of the rest of the particles created. There have been few attempts to study $\Lambda^0$'s in exclusive reactions [20], i.e., reactions where all the final state particles are measured. Therefore, our knowledge of the contributions to inclusive $\Lambda^0$ polarization from specific final states is quite limited. The present thesis is an attempt to clarify this situation.

The main goal of this dissertation is to search for $\Lambda^0$ polarization in specific final states. We examine four reactions in detail. We investigate the kinematic dependence of the polarization in each reaction and compare the polarization between different final states.

We present with more detail below how final state reactions are classified and what variables, from a kinematic point of view, are useful in

studying $\Lambda^0$ polarization. We explain how $\Lambda^0$ polarization is measured, outline the main features of the experiments that have studied $\Lambda^0$ polarization and their results, and describe the theoretical models that have been proposed to explain $\Lambda^0$ polarization.

In chapter 2 we describe BNL E766, which scientists from Columbia University, the University of Massachusetts at Amherst, the Universidad de Guanajuato, México, the University of Texas A & M, and the Fermi National Laboratory designed and ran. The data for this dissertation is from this experiment. In chapter 3 we describe how we selected the data sample. In chapter 4 we describe how we determined $\Lambda^0$ polarization. In chapters 5 and 6 we present the results and conclusions.

## 1.2    Some Definitions

In high energy physics, we distinguish between inclusive reactions and exclusive reactions. An inclusive reaction has the form $a+b \rightarrow c+X$. We study $c$ and ignore the rest of the reaction, $X$. An exclusive reaction can be written as: $a+b \rightarrow c+d_1+d_2+...+d_n$. We study $c$ in the particular channel that includes the specific set of particles $d_1, d_2, ..., d_n$.

In order to characterize the reactions of interest, we consider three different particle production models: i) Single diffraction dissociation (SDD), ii) Double diffraction dissociation (DDD), and iii) Double pomeron exchange (DPE). In Figure 1, we represent the idea of these processes. Equations 1, 2, and 3 represent these processes respectively.

$$h_1 + h_2 \rightarrow X + h \qquad (1)$$

$$h_1 + h_2 \rightarrow X + Y \qquad (2)$$

$$h_1 + h_2 \rightarrow X + h_1 + h_2 \qquad (3)$$

where $h_1$ represents the incoming beam particle, $h_2$ represents the target particle, $h$ represents either $h_1$ or $h_2$ in the final state, and $X$ and $Y$ represent the collection of diffractively produced particles in the final state. For example, consider that $h_1$ and $h_2$ are colliding protons. Equation 1 represents the case when one proton breaks up (either the beam proton or the target proton) and the other remains unaltered (Figure 1a). Equation 2 represents the case when both protons break up and two diffractive branches appear ($X$ and $Y$) (Figure 1b). Equation 3 represents the case when both protons remain unaltered and something extra ($X$) is created (Figure 1c).

The appropriate variables to use in describing the reaction final state particles in the center-of-mass system (CM) of the event are the Feynman scaling variable ($X_F$), the transverse momentum ($P_T$), and the mass of the diffractively produced system ($M_x$). $X_F$ is defined as the ratio of the longitudinal momentum of the particle, $P_z$, to the maximum longitudinal momentum of the particle, $P_{zmax}$. i.e.,

$$X_F = \frac{P_z}{P_{zmax}}.$$

In what follows, the variable $P_z$ will refer to the longitudinal momentum of the $\Lambda^0$ in the center-of-mass of the event and $P_T$ to the transverse momentum of the $\Lambda^0$, unless stated otherwise. Additionally we choose that $c = 1$ and $\hbar = 1$.

4

## 1.3 $\Lambda^0$ and $K_s^0$

$\Lambda^0$ hyperons and $K_s^0$ mesons, both, have two body decays, have similar lifetimes, and are often produced with similar momenta. Even though the decay kinematics are not quite the same, similar experimental biases -- if any -- should affect the measurement of each decay. Since $K_s^0$ has zero spin, it is a convenient test particle to determine if the technique to measure the polarization of $\Lambda^0$ is correct. A parallel analysis of $K_s^0$ polarization using the techniques to study $\Lambda^0$ must reveal that the $K_s^0$ polarization is zero. Otherwise the procedure to analyze $\Lambda^0$ polarization is flawed.

## 1.4 Polarization of $\Lambda^0$

### 1.4.1 Introduction

It is well known that strong interactions conserve parity. Parity conservation implies that a $\Lambda^0$ must be created with its spin normal to the creation plane [21]. The creation plane is defined as the plane formed by the momentum of the beam particle ($\vec{P}_{beam\,particle}$) and the momentum of $\Lambda^0$ ($\vec{P}_\Lambda$), in the laboratory system. See Figure 2. This figure shows the relation between the laboratory coordinate system and the creation plane, it also shows the coordinate system that we used to determine the $\Lambda^0$ polarization. The normal to the creation plane can be taken as the spin quantization axis. Therefore, we take this direction to define $\Lambda^0$ polarization. If we take $N_\uparrow$ and $N_\downarrow$ as the number of $\Lambda^0$'s with spin pointing along the normal to the creation

5

plane and the number of $\Lambda^0$'s with spin pointing along the opposite direction respectively, the polarization of $\Lambda^0$ is defined by

$$\wp_\Lambda = \frac{N_\uparrow - N_\downarrow}{N_\uparrow + N_\downarrow}.$$

In other words,

$$\wp_\Lambda = \left\langle \hat{\sigma}_\Lambda \cdot \left( \frac{\vec{P}_{beam\ particle} \times \vec{P}_\Lambda}{|\vec{P}_{beam\ particle} \times \vec{P}_\Lambda|} \right) \right\rangle.$$

### 1.4.2 Review of Experimental Results

Many $\Lambda^0$ polarization studies use a beam that hits a target at an angle. A neutral beam is obtained by sweeping charged particles out of the beam. Then the neutral beam is collimated. The $\Lambda^0$'s are collected and analyzed through its decay $p\pi^-$, using conventional spectrometers. Since the $\Lambda^0$'s are detected at some distance from the target, this technique tends to select energetic $\Lambda^0$'s rather than low momentum $\Lambda^0$'s. If we observe in the CM of event, it means that $\Lambda^0$'s are selected preferentially in the $P_z > 0$ hemisphere.

Experiments [2,..,14, 22] have shown that $\Lambda^0$ polarization in inclusive reactions has the following properties.

1. $\Lambda^0$ polarization seems to be a linear function of transverse momentum. It decreases from 0 at $P_T = 0$ to below -0.20 at $P_T = 1.6\,GeV$ [8].

2. For $P_T$ below $\sim 1.3\,GeV$, $\Lambda^0$ polarization is approximately linear with $P_T$ with a slope increasing with $X_F$ [22].

6

3. For $P_T$ above $\sim 1.3\,GeV$ $\Lambda^0$ polarization is independent of $P_T$ up to $P_T \sim 3.5\,GeV$ and approximately linear with $X_r$ [22].

4. $\Lambda^0$ polarization does not depend strongly on the beam particle's energy. The $P_T$ dependence of $\Lambda^0$ polarization is the same in the beam particle energy interval (6.0, 2000) $GeV$ [6, 7].

5. The $\Lambda^0$ polarization does not depend significantly on the nature of the target; $Be$, $Pt$, $Ir$, $W$, $p$, $H_2$, $D_2$, and $C$ have been used as targets [2,..., 12].

In Figure 3 we plot some of the results of previous experiments. This figure shows roughly that $\Lambda^0$ polarization is independent of target nature and the beam energy.

### 1.4.3  Review of Theoretical Models

$\Lambda^0$ polarization has been treated theoretically by several authors [15,...,19]. The main assumptions of the theoretical models treating $p + Target \rightarrow \Lambda^0 + anything$ are:

1. The wave function of $\Lambda^0$ is $|\Lambda^0\rangle = |ud\rangle|s\rangle$, where $|ud\rangle$ comes from the proton valence quarks. The $|ud\rangle$ diquark is in the S=0 state. The spin of $\Lambda^0$ is determined by the spin of the s-quark. It gives polarization to $\Lambda^0$.

2. The $s$-quark may appear from two alternative sources:
   i)   From the initial proton's quark sea.
   ii)  Produced during the collision from a gluon decaying into an $s\bar{s}$ pair $(g \rightarrow s\bar{s})$.

7

It is also assumed that the energy of $s$-quark in the CM system is low and depends little on the incident energy of the beam particle. The $\Lambda^0$ energy is thus given essentially by the energy of the ud-diquark. The differences between the models are the mechanisms proposed to polarize the $s$-quark state.

In the J. Szwed [19] model for inclusive and exclusive processes, the $s$-quark obtains transverse momentum by multiple scattering on quark-gluon matter. Since the $s$-quark has non-zero mass, it becomes polarized in this process.

In the K. Heller et al. [8] model for inclusive processes, the u-quark from the proton that disintegrates radiates a gluon that produces an $s\bar{s}$ pair. If the gluon is polarized in a bremsstrahlung mechanism, so is the $s\bar{s}$. This polarization is the same as $\Lambda^0$ polarization, and it is correlated with the transverse momentum direction of the $\Lambda^0$.

The B. Andersson et al. [18] model is a semi-classical one. The mechanism that produces the polarization of the $s$-quark is a soft process. In this kind of process perturbative QCD is not applicable. The quark anti-quark pairs ($s\bar{s}$) are produced by a tunneling process in the color field. During the process, parallel spins of $s$ and of $\bar{s}$ are balanced by angular momentum according to local angular momentum conservation. The correlation between the transverse momentum of the $s\bar{s}$-quarks (which is measured with respect to the momentum of the $s\bar{s}$ pair) and the spin of the $s\bar{s}$-quarks will make the $s\bar{s}$-quarks polarized.

8

In the T. DeGrand et al. [16] model for inclusive reactions, the origin of the $\Lambda^0$ polarization is explained in terms of the Thomas precession of the $s$-quarks spins during the recombination processes. The parton-recombination model plus SU(6) symmetry is used to relate the baryon's polarization to the polarization of the underlying constituents -- the $s$-quark.

In S.M. Troshin et al. [15], a $\Lambda^0$ polarization mechanism is not suggested. Instead a single time dynamical equation for the amplitude of $\Lambda^0$ polarization is proposed. They assume that the production of $\Lambda^0$ particles is the result of the decay of an excited proton state, $|uud(s\bar{s})\rangle$, containing a $(s\bar{s})$ pair in the **P** state. Since the $|uud\rangle$ quark state is not polarized, they suppose that the $(s\bar{s})$ pair is polarized. They do not propose a mechanism to polarize the $(s\bar{s})$.

In the Muller-Regge model, other ideas for $\Lambda^0$ polarization arise. In a Muller-Regge model with simple poles, $\Lambda^0$ polarization is identically zero. K.J.M. Moriarty et al. [17] proposed a model where the polarization results from Regge-cut contributions.

## 1.5 Dissertation Research Goals

The main goals for this dissertation research are the following:

1.  To study and measure $\Lambda^0$ polarization in the following exclusive reactions, where the $\Lambda^0 \to p\pi^-$ decay is detected:

    i)   $pp \to p\Lambda^0 K^+ \pi^+ \pi^-$,                                     6 track events

    ii)  $pp \to p\Lambda^0 K^+ \pi^+ \pi^- \pi^+ \pi^-$,                          8 track events

    iii) $pp \to p\Lambda^0 K^+ \pi^+ \pi^- \pi^+ \pi^- \pi^+ \pi^-$,             10 track events

    iv)  $pp \to p\Lambda^0 K^+ \pi^+ \pi^- \pi^+ \pi^- \pi^+ \pi^- \pi^+ \pi^-$, 12 track events

    The above reactions are produced in $27.5\,GeV$ proton-proton collisions.

2.  To determine, in each case, the $\Lambda^0$ polarization as a function of $P_T$ and as a function of $P_z$.

3.  To compare the polarization of $\Lambda^0$'s from the above reactions.

# CHAPTER 2

## EXPERIMENT BNL E766

### 2.1 Introduction

The goal of Brookhaven National Laboratory (BNL) experiment E766 is to study strong interaction processes in proton-proton and neutron-proton interactions. No model concerning this kind of interaction suggested these studies. The experiment was designed to measure, on an event by event basis, completely accurately, and with high statistics, high multiplicity final states.

Since no restrictive triggers were imposed and since very large amounts of data were collected, it has proved to be possible to study a variety of physics topics including: strange particle production [23], search for charmed particles [24], production of strange baryons [25], study of diffractive dissociation [26], and others.

In this section, we give a brief description of the beam line, the target, BNL E766's spectrometer, the drift chambers, the scintillation counters, the Cherenkov counter, the trigger system, and the first three steps in the data analysis. For construction details of the detector, for a detailed description of the multiparticle spectrometer and its drift chamber system, and for a description of the readout system, see Reference 24.

11

## 2.2    The Beam Line

The Alternating Gradient Synchrotron (AGS) at BNL in Upton, NY, provided the beam for E766. The beam proton from this machine has a typical energy of $28.5\,GeV$. The usual beam flux in the extracted beam line, B5, is 300 million protons per pulse. A beam pulse occurred for 1.2 seconds every 3 seconds. For more details see Reference 27.

The $28.5\,GeV$ beam used in the 1986 proton run was spread out by passing it through a copper target and then through a brass attenuator. This resulted in a beam of protons with an average kinetic energy of 27.5 $GeV$ and a mean flux of ~ 20 million protons per pulse. The beam was run through a collimator and two quadrupole magnets before it was measured in a beam spectrometer. The beam was measured to have an average momentum vector of $(-0.275, -0.03, 27.5)\,GeV$ and an ellipsoidal shape. The width was about 1.7 inches on the $X$ (horizontal) axis and 2.0 inches on the $Y$ (vertical) axis. The $Z$-momentum component spectrum of the proton beam is shown in Figure 4. The spectrum peaks at 27.5 $GeV$ and has a full width half maximum of 300 $MeV$ corresponding to a gaussian with $\sigma = 130$ $MeV$, approximately 0.5% of the mean momentum. Since the extracted beam has a momentum spread of approximately the same size, it is clear that the resolution of the beam chambers was adequate.

## 2.3    The $H_2$ Target

E766's target was liquid $H_2$ contained in a 3 inch diameter, 12 inch long cylinder. The $H_2$ container was made of 0.006693 inch (170 $\mu$) thick mylar.

12

The probability, (see Reference 28), for an interaction of the incoming proton, when it has traveled $x\ cm$ across the $H_2$ target is:

$$P(x) = 1 - e^{(-\gamma x/l)},$$

where $\gamma = 0.0708\ g/cm^3$ is the liquid $H_2$ density at 4.3 $K°$ and 1.1 atmosphere, and $l = 50.8\ g/cm^2$ is the nuclear interaction length in $H_2$.

## 2.4 The Spectrometer Magnet

The Jolly Green Giant (JGG) analyzing magnet is the structural base of the detector. It is a large dipole magnet that contains five drift chambers and the Middle Hodoscope. See Figure 5. The dimensions of its aperture are: 86.75 inches in width, 49 inches in vertical height, and 104 inches in length along the beam. The JGG has four independent coils. Each coil was run at 1500 amperes. The JGG did not provide a uniform magnetic field. When the magnetic coils are carrying 1500 amperes, the magnetic field in the center of the magnet is roughly 10 kG. This gives charged particles that move through it a 350 $MeV$ kick of transverse momentum.

The coordinate system for the experiment is fixed in the center of the magnet; i.e., $(0,0,0)$ of the coordinate system is in the center of the magnet. This coordinate system is a left handed one, with the positive $Z$-direction being downstream along the beam direction, the positive $Y$-direction up, and the positive $X$-direction is chosen so that a left handed coordinate system is defined. The coordinate system is shown in Figure 2, and in Figure 5.

13

## 2.5  The Drift Chambers

The drift chamber system consists of 6 drift chambers located inside the magnetic field of the Jolly Green Giant dipole magnet. The chamber's construction and operation details are described in References 24, and 29.

The drift chamber's main characteristics are:

1. Minimal material. Each drift chamber's material corresponds to 0.15% of a radiation length. This minimizes multiple scattering and particle re-interactions.

2. High segmentation. Each chamber has four planes of signal wires with very narrow spacing.

3. A large spatial aperture and acceptance over a large range of momenta.

4. High efficiency. The single plane efficiency exceeds 99%. This increased the capability to reconstruct particle trajectories, and therefore, it increased the number of events that could be completely reconstructed.

5. Large angular acceptance. Measured from the center of the target, the aperture of chamber 1 corresponds to an angle of ±36.47° in the X-direction, and ±23.92° in the Y-direction; the aperture of chamber 6 corresponds to an angle of ±18.14° in the X-direction, and ±12.32° in the Y-direction.

The drift chamber system's main purposes are:

1. To provide an optimum momentum measurement for all final state charged particles.

2. To determine all the final state charged particle trajectories. The measurement of a particle's trajectory and the measurements of the magnetic field of the magnet provide a mass independent measurement of the particle's momentum. An item by item description of the reconstruction algorithm and of the momentum measurements is provided in Reference 23.

The drift chamber system had 11,264 signal wires, all of them electronically instrumented. The description of the drift chamber system electronics is in Reference 24.

## 2.6 The Scintillation Counters

BNL E766 had 4 scintillation counter arrays: a target counter, the veto counter array, the Middle Hodoscope array, and the Rear Hodoscope array.

### 2.6.1 The Target Counter

The target counter is a square piece of scintillator attached to a photomultiplier, upstream of the target, (the beam proton hits the target counter before entering the target). This scintillator counter, like the other scintillators, is covered with aluminum foil and plastic electrical tape. The

15

dimensions of the scintillator are $2 \times 2 \times 3/32$ inches. Its main purpose is to detect the incoming beam proton.

### 2.6.2  The Veto Counters

There were 12 veto counters trapezoidally shaped that formed a truncated pyramid detector. This pyramidal detector surrounded the target with its main axis along the $Z$-direction. Each veto counter is made from four pieces of lead and five pieces of scintillator. Each one of the pieces was 1/8 inch thick. They alternate in a sandwich array. When neutral particles cross one of the lead pieces, charged particles are usually produced. These charged particles are detected by the next scintillators. For details of construction and electronics, see References 24 and 29.

### 2.6.3  The Middle and the Rear Hodoscopes

The Middle Hodoscope covers the aperture of chamber 4. The Rear Hodoscope covers the aperture of chamber 6. The purpose of the hodoscopes is to count the number of particles produced and to measure particle time of flight. The Middle Hodoscope, the Rear Hodoscope, and the target counter form the time-of-flight system (TOF). This system measures the velocity of the particles. When combined with the momentum measurements, the TOF is used to identify the mass of particles that have momentum below $2\,GeV$.

## 2.7   The Cherenkov Counter

The details of the Cherenkov counter design and construction are in References 24 and 27.

The main use of the Cherenkov counter is to identify relativistic particles. The Cherenkov counter's design is based on the Cherenkov effect. Charged particles in a medium will radiate light if the velocity of the particle is greater than the speed of light in that medium.

The gas of the E766 Cherenkov is $C_2Cl_2F_4$ (Freon 114) at atmospheric pressure. This gas has an index of refraction, $n = 1.0015$. A charged particle with a velocity greater than $0.9985c = c/n$ will radiate light inside the Cherenkov counter.

We used the Cherenkov counter in two different ways to identify relativistic particles. First we used it as a threshold counter to detect the light from a radiating particle. The threshold momentum is the momentum value of the particle at which it begins to radiate. Different types of particles have different threshold momentum values. This momentum depends on the particle's mass since the Cherenkov effect depends on the speed of the particle. The threshold momentum in Freon 114 for pions is $2.6\,GeV$. For kaons it is $9.0\,GeV$, and for protons it is $17.1\,GeV$. The second way was by measuring the light's intensity. The intensity of the light radiated by a particle is related to its velocity. This measurement improves the particle identification.

## 2.8    The Trigger System

It is not possible, even when using the fastest data acquisition system available, to read out every event.   Because of this, E766 -- and every experiment -- requires some type of trigger system.   A trigger's main objective is to accept only events that are candidates for the final objective.   In E766, the trigger rejects events that could not be fully reconstructed, determines if a proton interacts with a target proton, and detects an incoming beam proton.

We used the target counter to detect the incoming beam proton, and the Middle Hodoscope and the Rear Hodoscope to determine if the beam proton had collided with a target proton producing charged particles.   We used the veto counter around the hydrogen target to detect particles that escaped the detector before these particles could be measured.   The hardware processor, the different trigger conditions for selecting the data sample, and the multiplicity triggers are described in Reference 25.   The readout system is described in Reference 24.

## 2.9    The Data Analysis

Each stage reduces the number of events by discarding those events that are not going to be identified as exclusive.   Each step was known as PASS. Each step was not specific for any particular final state.

### 2.9.1 PASS1 - Track Reconstruction

The main task of PASS1 is to reconstruct particle trajectories. This task was performed by a specially constructed hardware computational system, the hardware processor. A detailed description of the algorithms used is in Reference 23. We distinguish three kinds of particle trajectories: six chamber trajectories (tracks passing through all six drift chambers), four upstream chamber trajectories (tracks passing through the first four drift chambers), and four downstream chamber trajectories (tracks passing through the last four drift chambers).

The trajectories of the particles were reconstructed from the Jolly Green Giant drift chamber information. Each drift chamber had four views. The hardware processor was programmed to obtain particle tracks in all four views. This information was used to reject the occasional tracks which were incorrect or false tracks. The ability to form 3 dimensional trajectories from pairs of views was very successful in rejecting incorrect tracks. The final 3-D trajectory used the information from all 4 views.

PASS1 also determined $P_{z_j}$ (the particle momentum component along the beam's momentum) for each particle. Events with

$$\sum_{j=1}^{n} P_{z_j} \geq 19.9 \, GeV,$$

where $n$ is the number of final state particles, were recorded for the next analysis step, PASS2. This cut rid the data of many non-exclusive candidate events.

### 2.9.2 PASS2 - Vertex Reconstruction

The general task of PASS2 is to reconstruct event vertices by looking for particle trajectories that intersect.

There are two kinds of vertices: the primary vertex and secondary vertices. We defined the primary vertex as the vertex where the proton-proton collision occurred. We found it by looking for the intersection formed by at least three different particle trajectories. We defined secondary vertices as the points where particles decay. We found these points (separated from the primary vertex) by looking for the intersections formed by at least two particle trajectories.

PASS2 reconstructed three-chamber tracks (tracks that passed through only three drift chambers) and provided better momentum measurement for all particles in an event.

Another task of PASS2 was to select events that satisfied the condition $\sum_{j=1}^{n} P_{z_j} \geq 26.5 \, GeV$ indicating that were few missing particles because the initial momentum along the $Z$-direction was 27.5 $GeV$. The average $X$-momentum component was -0.275 $GeV$ and the average $Y$-momentum component was -0.030 $GeV$. Since we are interested in exclusive events, PASS2 also accepted events with $P_T^2 \leq 0.02 \, (GeV)^2$, where

$$P_T^2 = \left[ \sum_{j=1}^{n} P_{x_j} - (-0.275) \right]^2 + \left[ \sum_{j=1}^{n} P_{y_j} - (-0.030) \right]^2$$

and $P_{x_j}$, and $P_{y_j}$ are the components of the momentum of particle $j$ perpendicular to the $Z$-axis. For PASS2 details see Reference 27.

20

The primary vertex reconstruction was then improved using the information from the trajectory of the beam particle (only events with one interacting beam proton in the target were used). This new point was used to improve the reconstruction of the final state particle trajectories. After this improvement, the $P_T^2$ cut was changed to $P_T^2 \leq 0.01\,(GeV)^2$ and the sum of the charges of the final state particles was required to equal 2.

### 2.9.3 PASS3 - Particle Identification

In the PASS3 step of the analysis, a new coordinate system is defined. The incoming proton direction is used as the new $Z$-direction. The new $Y$- and the new $X$-directions are perpendicular to each other and to the new $Z$-direction. As the beam proton direction changes slightly every event, each event has its own coordinate system.

The first step of PASS3 was to discard events that were not exclusive. In order to do that, the following cuts were imposed. It was required that all tracks were assigned to a vertex, except the beam proton track; that the total electric charge equaled 2; that the total longitudinal momentum was greater than $26.5\,GeV$; and that the total squared transverse momentum was less than $0.01\,(GeV)^2$, see next equation.

$$P_T^2 = \left( \sum_{j=1}^{a} P_{X_j} \right)^2 + \left( \sum_{j=1}^{a} P_{Y_j} \right)^2 \leq 0.01\,(GeV)^2$$

The $P_T^2$ cut was then tightened to $P_T^2 \leq 0.002\,(GeV)^2$ to improve the selection of exclusive final state events.

21

Figure 6 shows $P_T^2$ distribution for the 8 track final state sample; the $P_T^2$-cut is shown.

Another important task of PASS3 was to identify particles by using the information from the drift chambers (indirect particle identification), and by using the time-of-flight system and Cherenkov counter information (direct particle identification).

PASS3 programs were run on a Digital Equipment Corporation VAX Station 3200.

PASS3 details can be found in Reference 27.

### 2.9.3.1 $\Delta(E - Pl)$-Indirect Particle Identification

The initial state consists of two colliding protons; one at rest, the other with a momentum along the Z-direction of $\sim 27.5\, GeV$.

To reconstruct and to identify the final state events, we use many conservation laws: energy and momentum, charge, baryon number, strangeness, and lepton number.

The particles were identified as follows. In an event, an identity $(\pi^+, \pi^-, p, \bar{p}, K^+, \text{or } K^-)$ is assigned to each of the final state particles. In the assigning processes, the above mentioned conservation laws had to be satisfied, except the conservation of strangeness that was allowed to be violated by at most 1 unit. This is because strange particles might not have decayed at the point they were detected. Many combinations are possible. Each assignment was required to be self-consistent. For example, if the second

22

vertex were identified as a $\Lambda^0$, only assignments consistent with $p$ and $\pi^-$ as the decay products were taken. In principle, one assignment (the solution) is correct. In practice it is often difficult to select only one set of assignments. To find the most likely correct assignment, we used the $\Delta(E-Pl)$ technique (basically, energy-momentum conservation). Let $E$ be the total energy of the event and $Pl$ the total longitudinal momentum of the event along the beam proton direction. Then:

$$\Delta(E-Pl)=(E-Pl)_f-(E-Pl)_i$$

where $f$ means final state and $i$ means initial state.

If we require energy-momentum conservation in the reaction, this quantity,

$$\Delta(E-Pl)=\left(\sum_{j=1}^{n}(E_j-Pl_j)\right)_f-\left(\sum_{j=1}^{2}(E_j-Pl_j)\right)_i,$$

must be zero when we get the correct combination; where $n$ is the number of final state particles.

PASS3 kept all the solutions with $\Delta(E-Pl)$-values within $-0.028\,GeV$ to $0.032\,GeV$.

At times, there was more than one solution which satisfied $\Delta(E-Pl)$. For further discussion about this, see Chapter 3. Also see Reference 25.

### 2.9.3.2 TOF-Cerenkov-Direct Particle Identification

The direct particle identification consists in determining the particle's mass. To determine a particle's mass, we used its momentum and velocity

measurements. For relativistic particles (those with velocities greater than $0.99c$), the particle's velocity was determined using the Cherenkov counter. For slow particles (those with velocity below $0.99c$) the particle's velocity was determined using the TOF system. The momentum measurements were provided by the JGG's drift chambers system, for both, relativistic and non-relativistic particles.

Figure 7 shows $\Delta(E - Pl)$ distribution, in the interval (-0.028, 0.032) $GeV$ for the 8 track sample, without direct particle identification and with direct particle identification. From this figure we can see the improvement of the particle identification; the background is reduced roughly by half, using direct particle identification.

# CHAPTER 3

## $\Lambda^0$ POLARIZATION

In this chapter we show how we selected the data sample for $\Lambda^0$ polarization studies. This step in the data analysis was called PASS4. Also, we show how we defined the coordinate system that we used to determine $\Lambda^0$ polarization.

### 3.1    $\Lambda^0$ Sample Selection

The E766 collaboration collected $\sim 3.1 \times 10^8$ raw data events. ~2.7 million events passed all the cuts imposed in PASS1, PASS2, and PASS3. These events were identified as exclusive events. Roughly 10% of this data was identified as containing $\Lambda^0$ events. The last cuts of PASS2 and PASS3 described in sections 2.9.2 and 2.9.3 reduced this sample by roughly a factor of two.

For polarization studies, we used this sample (roughly 5% of the 2.7 million event data). Table 1 lists the features of this sample. In this table, the average number of solutions shown corresponds to the $\Delta(E - Pl)$ interval of $(-0.028, 0.032)$ $GeV$.

The $\Lambda^0$ sample has the following characteristics:

1)  The number of vertices equals 2. The primary vertex must be located inside the target. The secondary vertex must be consistent with being a $\Lambda^0$ decay. This requirement includes those secondary vertices which were consistent with both $\Lambda^0$ and $K_s^0$.

2)  All the tracks must be assigned to the primary vertex (that means, the primary vertex is a point on each those tracks). Exceptions to this are the beam track, which is not assigned, and the tracks created by the decay particles. In the last case, the tracks must be assigned to the secondary vertex and the projection of the composite (the track formed by the decay particle trajectories) track must be assigned to the primary vertex.

We selected the solutions for a particular final state, $pp \rightarrow p\Lambda^0 K^+ \left(\pi^+\pi^-\right)^N$ with $\Lambda^0 \rightarrow p\pi^-$ and $N=1,2,3,4$, in the following way. We checked that the solutions for a particular final state were consistent with the Cherenkov information and the TOF information. Solutions were rejected if they were inconsistent with the Cherenkov information. A Cherenkov inconsistency is a Cherenkov cell with no light and more than five photoelectrons predicted, or a Cherenkov cell with more than one photoelectron observed and none predicted. The solutions were also discarded if they were inconsistent with TOF information. A TOF inconsistency is a difference between the predicted time value and the observed one which exceeds the counter's resolution by three standard deviations.

Despite the elimination of solutions not consistent with the Cherenkov or the TOF information, the number of solutions per event remained roughly the same. In order to reduce the number of solutions per event and to improve the probability of getting the right solution, we tightened $\Delta(E-Pl)$ cut. Since we are interested in exclusive $\Lambda^0$ polarization measurements, improving the probability of getting the right solution is very important.

We selected the values of the $\Delta(E-Pl)$ cut in the following way. The $\Delta(E-Pl)$ cuts from PASS3 are -0.028 and 0.032 $GeV$. Considering only the solutions that passed all cuts -- except Cherenkov and TOF cuts -- the $\Delta(E-Pl)$ distributions for each final state sample peak roughly at $0.003\,GeV$. We discard the background of the distribution and fit the peak to a gaussian. In this way we get the standard deviation of the distribution's peak. We put a cut in $\Delta(E-Pl)$ values of two standard deviations. The limits are -0.008 and 0.013 $GeV$ (see Figure 7). A $\Delta(E-Pl)$ cut of two standard deviations around the value where $\Delta(E-Pl)$ distribution peaks assures that we have >90% probability of picking the right solution. See Reference 29 for a detailed description of this procedure.

The tight $\Delta(E-Pl)$ cut and direct-particle identification reduce the background roughly to half (see Figure 7). We call the <u>background</u> of the sample those remaining solutions which are not really $p\Lambda^0 K^+(\pi^+\pi^-)^N$.

The background comes from many sources.

1.  There can be several assignments of identities of the tracks that satisfy all the cuts (more than one solution). For example, the $K^+$ may be

27

interchanged with the $p$ or the $p$ with a $\pi^+$; if the event survives all the cuts (when we interchange the identities of the tracks), we have no way to decide which is the correct solution. Therefore, we take both.

2. There might be one missing neutral particle. This contribution should be suppressed by the $P_T^2$ and $\Delta(E - Pl)$ cuts.

3. An event of a different final state which accidentally happens to have a solution consistent with $p\Lambda^0 K^+ (\pi^+\pi^-)^N$.

4. Mis-measurements of particle trajectories could result in a non-exclusive final state satisfying the cuts.

Table 2 lists a rough estimate of the percent of background for each sample.

The fraction of the events passed the $\Delta(E - Pl)$ cut is ~89%. The average number of solutions per event after all cuts is approximately one. If an event has more than one solution we select just one and discard the rest. (This procedure does not affect our $\Lambda^0$ polarization measurements, because if we have one event with two solutions the identity of $\Lambda^0$ decay products does not change.) Table 3 lists the characteristics of the sample that we used to study $\Lambda^0$ polarization.

A typical event from the 8 track final state, that passed all the cuts, is shown in Figures 8 and 9. In Figure 8 many detector elements are represented. We can see the tracks and the primary and secondary vertices. Track 8 is the negative pion and track 6 is the proton that comes from the $\Lambda^0$. The proton track curves to the negative $X$-direction and the pion track curves

28

to the positive $X$-direction. The primary vertex is very close to the upstream end of the target. The secondary vertex is between the second and third chamber. Two views of the same event are presented in Figure 9; the primary vertex and the secondary vertex are more evident.

We ran PASS4 programs on a Digital Equipment Corporation VAX Station 3200.

## 3.2    $\Lambda^\circ$ Polarization

We explain the definitions and the conventions that we use to determine $\Lambda^0$ polarization.

The polarization of $\Lambda^0$ is defined as:

$$\wp_\Lambda \equiv \langle \hat{\sigma}_\Lambda \cdot \hat{n} \rangle,$$

where $\hat{\sigma}_\Lambda$ represents the spin of the $\Lambda^0$ and $\hat{n}$ defines the direction of the quantization axis.   Instead of using the spin polarization definition to measure $\Lambda^0$ polarization, we used the angular distribution of its decay -- $p$ and $\pi^-$.

Our data are analyzed in a left handed coordinate system.   In that coordinate system we define the normal to the creation plane as:

$$\hat{n} = \frac{\vec{P}_\Lambda \times \vec{P}_{beam\ proton}}{\left| \vec{P}_\Lambda \times \vec{P}_{beam\ proton} \right|}.$$

This definition is consistent with the current literature convention (see Reference 9.) We define the coordinate system where the $\Lambda^0$ polarization is

29

measured in the following way. We define the $Y$-direction along the $\hat{n}$ direction, $\hat{n}_y = (0,1,0) = \hat{n}$, the $Z$-direction as the $\vec{P}_\Lambda$ direction, $\hat{n}_z = (0,0,1) = \vec{P}_\Lambda / |\vec{P}_\Lambda|$, and the $X$-direction so that we have a left handed coordinate system, $\hat{n}_x = (1,0,0) = -\hat{n}_y \times \hat{n}_z$. In this way, each event has its own coordinate system.

In the coordinate system where the $\Lambda^0$ is at rest, the angular distribution of the proton is given by:

$$\frac{dN}{d\Omega} = \frac{N_0}{4\pi}\left(1 + \alpha \vec{\wp}_\Lambda \cdot \hat{P}_p\right), \tag{3.1}$$

where $\dfrac{dN}{d\Omega}$ is the probability of obtaining $dN$ protons inside the angular region $d\Omega$, $\alpha = 0.64 \pm 0.013$ [28] is the asymmetry parameter of $\Lambda^0$ decay, $\vec{\wp}_\Lambda$ is the polarization, and $\hat{P}_p$ is the unit momentum vector of the proton. The polarization can be considered to have three components, one along each axis. $\wp_{\Lambda x}$ is the left-right asymmetry of the $\Lambda^0$ decay proton, $\wp_{\Lambda y}$ is the up-down asymmetry, and $\wp_{\Lambda z}$ is the backward-forward asymmetry. According to parity conservation in strong interactions, $\wp_{\Lambda x} = 0$ and $\wp_{\Lambda z} = 0$.

# CHAPTER 4

## PROCEDURES TO DETERMINE POLARIZATION

### 4.1 Corrections to the Data

In every experiment, it is necessary to determine if either the apparatus or the analysis procedures affect the physics being measured. For example, a small geometrical acceptance or a series of restrictive cuts might distort an otherwise smooth distribution. Many previous measurements of $\Lambda^0$ polarization have studied and corrected for such effects using techniques including Monte Carlo [3] and the Hybrid Monte Carlo method [9].

However, we believe that experiment E766 has an important advantage over those measurements. The large geometrical acceptance of the apparatus indicates that $\Lambda^0$'s are detected well over a broad range of kinematic conditions, especially over those variables important to the determination of polarization. Although there are clearly differences in the detection probability as a function of $\Lambda^0$ momentum, there are no *a priori* arguments suggesting that the acceptance changes rapidly over variables such as $\cos\theta_y$, the distribution from which the polarization is determined. For this reason, and because any correction for apparatus-related effects would introduce additional uncertainties in the polarization, we present our results assuming that the acceptance in $\cos\theta_y$ is flat. We recognize that this assumption must be justified and we do so in Chapter 6 after we present the polarization results.

## 4.2 Coordinate Systems

The relation between the coordinate system used to measure $\Lambda^0$ polarization and the laboratory coordinate system is as follows. If we start in the $\Lambda^0$ rest frame that has its axes parallel to those in the laboratory coordinate system (obtained with a boost from the laboratory coordinate system to the $\Lambda^0$ rest frame), the relationship between these two coordinate systems is given by matrix $\mathfrak{I}$.

$$\mathfrak{I} = \begin{bmatrix} VN_{xx} & VN_{xy} & VN_{xz} \\ VN_{yx} & VN_{yy} & VN_{yz} \\ VN_{zx} & VN_{zy} & VN_{zz} \end{bmatrix}$$

where:

$$VN_{xx} = -VN_{yy} \cdot VN_{zz} + VN_{yz} \cdot VN_{zy}$$

$$VN_{xy} = -VN_{yz} \cdot VN_{zx} + VN_{yx} \cdot VN_{zz}$$

$$VN_{xz} = -VN_{yx} \cdot VN_{zy} + VN_{yy} \cdot VN_{zx}$$

and

$$VN_{yx} = \frac{\left(\vec{P}_\Lambda \times \vec{P}_{beam}\right)_X}{\left|\vec{P}_\Lambda \times \vec{P}_{beam}\right|}$$

$$VN_{yy} = \frac{\left(\vec{P}_\Lambda \times \vec{P}_{beam}\right)_Y}{\left|\vec{P}_\Lambda \times \vec{P}_{beam}\right|}$$

$$VN_{yz} = \frac{\left(\vec{P}_\Lambda \times \vec{P}_{beam}\right)_Z}{\left|\vec{P}_\Lambda \times \vec{P}_{beam}\right|}$$

$$VN_{zx} = \frac{P_{\Lambda X}}{|\vec{P}_\Lambda|}$$

$$VN_{zy} = \frac{P_{\Lambda Y}}{|\vec{P}_\Lambda|}$$

$$VN_{zz} = \frac{P_{\Lambda Z}}{|\vec{P}_\Lambda|}$$

where $\vec{P}_\Lambda$ and $\vec{P}_{beam}$ are the $\Lambda^0$ momentum and the beam momentum in the laboratory coordinate system respectively.

For example, if $\vec{P}_p$ is the decay proton momentum vector in the $\Lambda^0$ rest frame, the corresponding momentum vector in the $\Lambda^0$ rest frame where we measured the polarization is given by $\vec{P}_p{}' = \Im \vec{P}_p$.

## 4.3    Polarization Determination

The procedure to determine $\Lambda^0$ polarization $\wp = (\wp_x, \wp_y, \wp_z)$, was the following. Consider the decay proton momentum in the $\Lambda^0$'s rest frame. This momentum vector can be written as $P(\cos\theta_x, \cos\theta_y, \cos\theta_z)$. We histogram the values $\cos\theta_i$, $i = x, y, z$, in 20 bins from -1 to +1. Since these distribution are supposed to follow equation 3.1, we fit each one to a straight line using the least-squares technique. An example of $\cos\theta_y$ distribution is given in Figure 41a. The slope of the straight line fit is:

$$m_i = \frac{N_{\alpha} \alpha \wp_i}{4\pi}$$

and the constant parameter is $b_i = \frac{N_{\alpha}}{4\pi}$, where $b_i$ is the value of the intercept.

33

From these equations we obtain:

$$\wp_i = \frac{m_i}{b_i \alpha}, \quad i = x, y, z.$$

The statistical errors for the polarization are given by:

$$\Delta \wp_i = \frac{m_i}{b_i \alpha} \left( \left( \frac{\sigma_{m_i}}{m_i} \right)^2 + \left( \frac{\sigma_{b_i}}{b_i} \right)^2 + \left( \frac{\sigma_\alpha}{\alpha} \right)^2 \right)^{1/2} \quad i = x, y, z.$$

See Appendix II for a detailed discussion of error propagation.

# CHAPTER 5

## RESULTS AND DISCUSSIONS

In chapters 3 and 4 we described the procedures to determine $\Lambda^0$ polarization. In this chapter we present our determination of the $\Lambda^0$ polarization and the consistency checks that we performed. We present our conclusions in the last section of Chapter 6.

### 5.1   Distributions in $P_z$ and in $P_T$

In Figure 10, we show the number of $\Lambda^0$'s observed versus $P_z$ for each of the final states. The difference in the shape of the distributions is due to the different production processes involved.

We can understand the $P_z$ shapes using the SDD model and the DDD model. The 6 and 8 track $P_z$ distributions are consistent with the SDD model (Figure 10a, and 10b, respectively). The backward peaks are consistent with $\Lambda^0$'s produced from target fragmentation and the forward peaks correspond to $\Lambda^0$'s produced from beam fragmentation. The 10 and 12 track $P_z$ distributions are consistent with the DDD model (Figure 10c, and 10d, respectively). The peaks around $P_z = 0$ correspond to $\Lambda^0$'s that are from both the target fragmentation and beam fragmentation. In this case it is difficult to separate $\Lambda^0$'s produced in target dissociation from those created by beam dissociation. Figure 11 shows $P_T$ distributions in each final state multiplicity.

## 5.2   $\Lambda^0$ Polarization in the 8 Track Final State

The accuracy of $\Lambda^0$ polarization measurements is limited by the size of the sample being studied. The number of events in each of the samples is listed in Table 3. Since the 8 track final state is the largest sample, we started our $\Lambda^0$ polarization investigation with that final state.

### 5.2.1   $P_T$ and $P_z$ Dependence

Using the entire sample, we divided the data sample into 5 $P_T$ bins. Table 4 shows these bins. In each bin of $P_T$, we determined the $\Lambda^0$ polarization along the axis perpendicular to the creation plane. Our results are in Table 5 and in Figure 12.

The polarization in this final state is consistent with zero and is independent of $P_T$. This result is extremely surprising! The result is rather different from any other study of $\Lambda^0$ polarization. Either we have discovered a particular reaction in which polarization plays no role or there is an error in our analysis procedure. An intensive investigation of all our assumptions and analyses was begun.

No errors in our procedures were found. However, we did observe that our experiment accepted $\Lambda^0$'s over a much wider range of kinematic variables than most previous experiments. But it was not immediately evident how a better acceptance could cause the polarization phenomenon to disappear.

In most fixed target experiments, only $\Lambda^0$'s produced with positive longitudinal momentum in the center of mass of the interaction ($P_z > 0$) are detected. The design of the beam line and the large separation between the detector and the $\Lambda^0$ production point select such $\Lambda^0$'s preferentially over the lower laboratory momentum $\Lambda^0$'s with $P_z < 0$. However, as shown in Figure 10, this experiment observes roughly equal numbers of events with $P_z > 0$ and with $P_z < 0$ in the 8 track final state. To determine if this was related to our surprising result, we separated the data into two $P_z$ bins -- the "backward hemisphere" ($P_z < 0$) and the "forward hemisphere" ($P_z > 0$). We divided the data in each hemisphere into 5 equal $P_T$ bins. See Table 4. In each hemisphere and in each $P_T$ bin, the $\Lambda^0$ polarization was determined. The results of those $\Lambda^0$ polarization determinations are in Table 6 and in Figure 13.

The differences between the two hemispheres are dramatic and quite unexpected. In the forward hemisphere ($P_z > 0$), the polarization decreases roughly linearly with $P_T$ -- from zero at $P_T=0$ to ~-0.23 at $P_T=1.118$ $GeV$. In sign, magnitude, and $P_T$ dependence, the polarization in this final state agrees with $\Lambda^0$ polarization measured in inclusive final states. In Figure 14, we compare our results with the results of Reference 4. The results are very similar.

However, in the backward hemisphere ($P_z < 0$), the polarization increases as $P_T$ increases -- from zero at $P_T=0$ to ~+0.18 at $P_T=1.118$ $GeV$. Within statistics, the polarization in the two hemispheres is the same in magnitude but of opposite sign. Since our 8 track final state sample has roughly equal numbers of events from each hemisphere and the backward

37

hemisphere $P_z$ ($P_T$) distribution is the same as, bin to bin, the forward hemisphere $P_z$ ($P_T$) distribution, our combined total sample had no net polarization.

Statistically, $\Lambda^0$ polarization in the forward hemisphere is mirror symmetric to $\Lambda^0$ polarization in the backward hemisphere.

The model of B. Andersson may be relevant to this observation. According to that model, in beam fragmentation the $\Lambda^0$ is formed if an $s\bar{s}$-pair is generated in the field of the (ud)-diquark (from the proton) in the $S=0$ state. The $\Lambda^0$ continues in the same direction (with the same sign of $P_z$) as the beam proton. With this production mechanism, the spin of the $\Lambda^0$ is determined by the spin of the $s$-quark. $s$ and $\bar{s}$ spins are anti-parallel to the normal of the creation plane and are balanced by the orbital angular momentum. Thus, the $\Lambda^0$ has negative polarization. During target fragmentation, the same arguments lead to positive polarization but the $\Lambda^0$ has negative $P_z$. In either case, the magnitude of $\Lambda^0$ polarization is expected to increase with increasing transverse momentum of the $\Lambda^0$.

We thought that experiments with colliding beams might have measured $\Lambda^0$ polarization in the backward hemisphere. The experiment of T. Henkes et al. [20] does partially. We discuss their results and compare with ours in the next section. The experiment of A.M. Smith et al. [11] does not observe in the backward hemisphere. They observe only in the forward hemisphere.

## 5.2.2   Dependence on Other Kinematic Variables

### 5.2.2.1   Further Investigation of the $P_z$ Dependence

Using the 8 track sample, we have studied $\Lambda^0$ polarization (for both $P_z > 0$ and $P_z < 0$) as a function of $P_T$. From those results, we have learned that the $\Lambda^0$ polarization depends strongly on $P_z$. However, important questions remain. How does the $\Lambda^0$ polarization depend on $P_z$ or $X_F$? And where (in $P_z$) does the $\Lambda^0$ polarization pass from negative to positive values? We address these questions in this section. To study $\Lambda^0$ polarization as a function of $P_z$, we divided the $P_z$ variable into 6 $P_z$ bins, see Table 7. Each $P_z$ bin covers the total $P_T$ range, $(0, 1.2) GeV$; in this way, in each $P_z$ bin our measurements are integrated over the $P_T$ variable. In each $P_z$ bin, we determined the $\Lambda^0$ polarization. The results are in Table 8 and shown in Figure 15, we plot the polarization as a function of $X_F$ ($P_{zmax} = 3.2\,GeV$). From Figure 15, we can see that $\Lambda^0$ polarization depends on $P_z$ (or $X_F$). $\Lambda^0$ polarization value is ~0.14 at $P_z = -2.6\,GeV$ and decreases roughly linearly to ~-0.23 at $P_z = +2.6\,GeV$. $P_z = 0$ is the point where $\Lambda^0$ polarization appears to change sign. This fact has been observed in a colliding beam proton experiment [20]. They have observed that $\Lambda^0$ polarization depends on $P_z$ or $X_F$ (for $X_F$ in Reference 20 is defined in the CM of the $\Lambda^0 K^+$ system, our data are not directly comparable with theirs), and the point where $\Lambda^0$ polarization, as a function of $X_F$, changes sign is approximately $X_F = -0.5$. In their words: "$P_\Lambda$ depends on $\cos\Theta$. It is positive for $\cos\Theta < -0.5$, becomes negative for $\cos\Theta > -0.5$, reaches a maximum of $(-62 \pm 10)\%$ near $\cos\Theta \sim 0.25$, and decreases again in magnitude for forward going $\Lambda^0$'s." (Here $\cos\Theta$ is equal to

$X_F$ in the CM of their $\Lambda^0 K^+$ system and $P_\Lambda$ is the polarization with respect to the normal of the creation plane.)

### 5.2.2.2 Relative Directions of $\Lambda^0$ and $K^+$ and of $\Lambda^0$ and $p$

Because we had observed such strong dependence on $P_T$ and $P_Z$, we investigated if there were other kinematic variables which were correlated with the polarization. Theoretical models [18] suggest that the relative motion between $\Lambda^0$ and other particles of the reaction affects $\Lambda^0$ polarization. For example, the model of Andersson et al. proposes that there must be a relation between the relative motion of the $\Lambda^0$ and the $K^+$ and $\Lambda^0$ polarization. This model proposes that the quarks $s$ and $\bar{s}$ are created in opposite directions when $\Lambda^0$ is polarized. Crudely, we take their directions as the directions of the $\Lambda^0$ and the $K^+$ respectively.

We investigated if $\Lambda^0$ polarization is affected by the relative motion between the $\Lambda^0$ and the $K^+$. Additionally, we searched for any dependence with the relative motion between the $\Lambda^0$ and the $p$.

In the kinematic region where the $\Lambda^0$ and the $K^+$ have the same sign of the $Z$ -component of momentum in the center of mass of the event ($Pzcm$), we separate the sample into $P_z < 0$ and $P_z > 0$ bins. In each of these regions, we chose 5 $P_T$ bins and measured the $\Lambda^0$ polarization. The results are in Table 9. For the case where the $\Lambda^0$ and the $K^+$ have the opposite sign of $Pzcm$, we repeated the above procedure. The results are in Table 10. The number of $\Lambda^0$ with the same sign of $Pzcm$ as that of the $K^+$ is ~3/5 of the sample, and the number with opposite signs is ~2/5 of the sample. The statistics in the region

where $\Lambda^0$ and $K^+$ have the same sign of *Pzcm* in the CM of event are very close to the statistics of the region where $\Lambda^0$ and $K^+$ have opposite sign of *Pzcm*. Thus, we can compare the polarization (as a function of $P_z$ and as a function of $P_T$) between those regions. We also compare with the polarization determined in the region where no conditions between $\Lambda^0$ and $K^+$ were imposed. In Figure 16 we compare these results; these measurements agree. The polarization for $(P_z > 0)$ when the $\Lambda^0$ and $K^+$ have the same sign of *Pzcm* seems to be smaller than the polarization (for $P_z > 0$) when $\Lambda^0$ and $K^+$ have the opposite sign of *Pzcm*. If we average the polarization in each case, we get -0.078 ± 0.064 and -0.163 ± 0.078 respectively. We conclude that statistically both measurements are the same. If we compare the polarization measurements in the backward hemisphere, we have similar conclusions, since the average polarization in each case is + 0.083 ± 0.056, and + 0.112 ± 0.067 respectively.

To determine if there is a dependence of $\Lambda^0$ polarization on the relative motion of the $\Lambda^0$ and the $p$, we followed a similar procedure. For the case with the opposite signs of *Pzcm*, the results are in Table 11. For the case with the same signs, the results are in Table 12. In this case we lack the statistics to measure $\Lambda^0$ polarization for $P_z > 0$. Roughly 4/5 of the events are with the $\Lambda^0$ and $p$ with the opposite signs and roughly 1/5 of the events are in the region where the $\Lambda^0$ and the $p$ have the same sign of *Pzcm*. (Most of these events are in $P_z < 0$ region.)

In the region where $\Lambda^0$ and $p$ have the opposite sign of *Pzcm*, in the forward hemisphere, and in the backward hemisphere, we do have enough data to compare the polarization with the polarization of the region where no

41

conditions were imposed between the relative directions of $\Lambda^0$ and $p$; we found that statistically they agree. See Figure 17(a). In the region where $\Lambda^0$ and $p$ have the same sign of $Pzcm$, in the forward hemisphere, we do not have enough data to compare the polarization with the polarization of the region where no conditions were imposed between the relative directions of $\Lambda^0$ and $p$. However, in the backward hemisphere we do have and we determine $\Lambda^0$ polarization, see Figure 17(b). $\Lambda^0$ polarization, in the backward hemisphere, when $\Lambda^0$ and $p$ have the same sign of $Pzcm$, seems to be consistent with zero $(0.04 \pm 0.07)$. This is most probably due to the $X_F$ distribution of the $\Lambda^0$'s in that sample, since the polarization is small near $X_F = 0$. In this region, ~ 75% of the $\Lambda^0$'s have $X_F < 0.3$. Therefore, we observe $\Lambda^0$ polarization consistent with zero.

### 5.2.2.3 $M(\Lambda K)$, $M(\Lambda K \pi^+ \pi^-)$, and $M(\Lambda K 2(\pi^+ \pi^-))$

Some authors have claimed that $\Lambda^0$ polarization depends on other variables besides $P_T$ and $P_z$. For example, in the reaction $pp \rightarrow p(\Lambda^0 K^+)$, T. Henkes et al. [20] observe that $\Lambda^0$ polarization decreases to -63 ± 4% when $M(\Lambda K)$ is 2.8 $GeV$. Following these suggestions we investigated $\Lambda^0$ polarization as a function of $M(\Lambda K)$, $M(\Lambda K \pi^+ \pi^-)$, and $M(\Lambda K 2(\pi^+ \pi^-))$.

We divided the 8 track sample into 5 $M(\Lambda K)$ bins. See Table 13. In each of these bins we determined $\Lambda^0$ polarization. The results are in Table 14. Figure 18 shows these results. From this figure we can see that $\Lambda^0$ polarization is consistent with zero and independent of $M(\Lambda K)$, in the entire sample. This is due to the effect observed in section 5.2.1 -- the mirror symmetry in $P_z$. As we did for the $P_T$ variable, we separated the sample into

$P_z < 0$ and $P_z > 0$ pieces. Each of these bins was divided into 5 bins of $M(\Lambda K)$, see Table 13. In each of these bins we determined $\Lambda^0$ polarization. The results are in Table 15. Figure 19 shows these results and compares them with Reference 20 data. From Figure 19, we see that $\Lambda^0$ polarization does depend on $M(\Lambda K)$. However, it is not clear that this dependence is not just the dependence on $P_r$ and $P_z$ discussed in section 5.2.1. Since $M(\Lambda K)$ depends directly on both variables through the equation of energy-momentum conservation. We do note that the polarization magnitude in both hemispheres is roughly ~0.13 at $M(\Lambda K) = 2.47\,GeV$. Although the reaction is not identical to the $pp \to p(\Lambda K)$ final state in Reference 20, these results do not confirm their observation of significantly enhanced polarization, but in the region of $M(\Lambda K)$ where both experiments overlap, the $\Lambda^0$ polarization measurements agree, see Figure 19. In the forward hemisphere $\Lambda^0$ polarization is negative. At $M(\Lambda K) = 1.7\,GeV$, the polarization is consistent with zero, it decreases roughly linearly to ~ $-0.16$ at $M(\Lambda K) = 2.47\,GeV$. In the backward hemisphere at $M(\Lambda K) = 1.7\,GeV$, the polarization is consistent with zero, and it increases roughly linearly to ~ $+0.11$ at $2.47\,GeV$.

We also note that these results represent the first study of $\Lambda^0$ polarization as a function of $M(\Lambda K)$ variable in the backward hemisphere.

To study $\Lambda^0$ polarization as a function of $M(\Lambda K \pi^+ \pi^-)$, we divided the 8 track sample into 5 $M(\Lambda K \pi^+ \pi^-)$ bins. See Table 16. We determined $\Lambda^0$ polarization in each of these bins. The results are in Table 17. In the entire sample, $\Lambda^0$ polarization is consistent with zero and independent of $M(\Lambda K \pi^+ \pi^-)$, as can be seen in Figure 20. Because of the symmetry in $P_z$, we separated the sample into $P_z < 0$ and $P_z > 0$ hemispheres. We divided each of

43

these bins into 5 bins of $M(\Lambda K \pi^+ \pi^-)$, see Table 16. We determined $\Lambda^0$ polarization in each of these bins. The results are in Table 18. Figure 21 shows these results. From this figure we can see that $\Lambda^0$ polarization depends on $M(\Lambda K \pi^+ \pi^-)$ variable. In the forward hemisphere $\Lambda^0$ polarization is negative. At $M(\Lambda K \pi^+ \pi^-) = 2.75\, GeV$, the polarization is consistent with zero, it decreases roughly to -0.16 at $M(\Lambda K \pi^+ \pi^-) = 3.75\, GeV$. In the backward hemisphere $\Lambda^0$ polarization is positive. At $M(\Lambda K \pi^+ \pi^-) = 2.75\, GeV$, the polarization is consistent with zero, it increases roughly to 0.06 at $M(\Lambda K \pi^+ \pi^-) = 3.75\, GeV$. In this case also, our results represent the first study of $\Lambda^0$ polarization as a function of $M(\Lambda K \pi^+ \pi^-)$ in the backward-forward hemisphere.

For the case of $M(\Lambda K 2(\pi^+ \pi^-))$ variable, we divided the entire sample into 5 $M(\Lambda K 2(\pi^+ \pi^-))$ bins, see Table 19. In each of these bins we determined $\Lambda^0$ polarization. The results are in Table 20. Figure 22 shows these results. From Figure 22, we can see that $\Lambda^0$ polarization is consistent with zero and independent of $M(\Lambda K 2(\pi^+ \pi^-))$.

As we did for the $P_T$ variable, we separated the sample into $P_z < 0$ and $P_z > 0$ bins. Each of these bins was divided into 5 $M(\Lambda K 2(\pi^+ \pi^-))$ bins. In each of these bins we determined $\Lambda^0$ polarization. The results are in Table 21. Figure 23 shows that results. From Figure 23, we see that $\Lambda^0$ polarization depends on $M(\Lambda K 2(\pi^+ \pi^-))$. In the forward hemisphere $\Lambda^0$ polarization is negative. At $M(\Lambda K 2(\pi^+ \pi^-)) = 3.9\, GeV$ the polarization is consistent with zero, it decreases roughly linearly to $\sim -0.14$ at $M(\Lambda K 2(\pi^+ \pi^-)) = 5.1\, GeV$. In the backward hemisphere $\Lambda^0$ polarization is positive. At $M(\Lambda K 2(\pi^+ \pi^-)) = 3.9\, GeV$ the polarization is roughly consistent with zero, it increases roughly linearly

to $\sim 0.06$ at $M(\Lambda K 2(\pi^+\pi^-)) = 5.1\,GeV$. Our conclusions are the same as in the dependence on $M(\Lambda K)$, and on $M(\Lambda K\pi^+\pi^-)$.

### 5.2.3 $\Lambda^0$ Not Produced Directly

$\Lambda^0$ polarization may depend on whether the $\Lambda^0$ is produced directly or is the decay product of a particle or resonance produced in the strong interaction of the two protons. This is particularly troublesome to inclusive studies which are unable to distinguish directly produced $\Lambda^0$'s from those made in other ways. In our exclusive final states, we have the ability to study the contributions from non-directly produced $\Lambda^0$'s.

### 5.2.3.1 $\Sigma^0 \rightarrow \Lambda^0\gamma$

In inclusive $\Lambda^0$ production at these energies, as much as 30% of the $\Lambda^0$'s are the result of decays of $\Sigma^0$ [30]. Those $\Lambda^0$'s dilute the polarization observed inclusively, making comparison with theoretical models difficult.

In our exclusive sample, we expect the contribution from $\Sigma^0$'s to be reduced compared to inclusive production. The stringent demands on $P_T^2$ and longitudinal momentum restrict the kinematic regions when the gamma ray from the $\Sigma^0 \rightarrow \Lambda^0\gamma$ decay can be unobserved. If the missing momentum is too large, the event will not pass our cuts.

In order to estimate the fraction of $\Lambda^0$'s from $\Sigma^0$ decay, we conducted a Monte Carlo simulation. We assumed that the production processes for $\Sigma^0$ were identical to those describing $\Lambda^0$ production. (See Chapter 6 for a detailed

45

presentation of the Monte Carlo procedures.) Once produced, the $\Sigma^0$'s were decayed isotropically in their center of mass into $\Lambda\gamma$. Information about the $\gamma$ was then discarded and the event processed as thought it were $\Lambda^0$ production.

From these studies, we found that the average acceptance for $\Lambda^0$ produced from $\Sigma^0$ is 1.32%. Using another Monte Carlo sample of $\Lambda^0$ directly produced (see Chapter 6) we found that the average acceptance for $\Lambda^0$ directly produced is 11.17%. If we suppose that the $\Sigma^0$ production is equal to the $\Lambda^0$ production, the ratio of the $\Lambda^0$ produced through $\Sigma^0 \to \Lambda^0\gamma$ to the $\Lambda^0$ produced directly is roughly 12%. But from inclusive studies, we know that $\Sigma^0$ production is $0.28 \pm 0.011$ [30] of a $\Lambda^0$ production. Thus the ratio of $\Lambda^0$ produced through $\Sigma^0 \to \Lambda^0\gamma$ to $\Lambda^0$ produced directly is roughly $(3.36 \pm 0.132)\%$. From these Monte Carlo studies, we determined cuts which would reduce the possible contamination of $\Lambda^0$ from $\Sigma^0$ decay in the sample. By choosing the total sum of the longitudinal momentum of the event between $(27.3, 28.0)$ $GeV$, and the total squared transverse momentum less than $0.001$ $GeV^2$, we discard 75% of the $\Sigma^0$ ($\Lambda^0$) Monte Carlo output sample. When we put these cuts on the 8 track Monte Carlo sample ($\Lambda^0$ directly produced), the sample was reduced by 14%.

Demanding the above mentioned cuts, the 8 track sample was reduced 37.5%. In this sample, the ratio of $\Lambda^0$'s produced through $\Sigma^0$ decay to direct $\Lambda^0$'s is roughly 1%. In this reduced sample, we studied $\Lambda^0$ polarization as a function of $P_z$ and $P_r$ , as we did in section 5.2.1. The results are in Table 22. In Figure 24 we compare these results with the results that we obtained in section 5.2.1. From this figure, we can see that statistically the results are the

same. We conclude that the 3.36% of the contamination from $\Sigma^0$ does not affect our results on $\Lambda^0$ polarization.

### 5.2.3.2 $\Sigma^{*-} \rightarrow \Lambda^0 \pi^-$

The resonance $\Sigma^{*-}$ (1385) was detected in our $\Lambda^0$ sample.

The following procedure was followed to determine what effect, if any, the existence of this resonance had on our measurements.

In Figure 25 we plot the invariant mass of all possible combinations of $\Lambda^0 \pi^-$. It peaks clearly around 1.385 $GeV$. In the figure we indicate the cuts ((1.33, 1.46) $GeV$) we performed on the sample around the peak of the distribution. The events inside this interval were discarded; they represent roughly 4.2% of the sample. We measure $\Lambda^0$ polarization with the rest of the events. The results of these measurements are in Table 23. In Figure 26 we compare these $\Lambda^0$ polarization measurements with the results obtained in section 5.2.1. From this figure, we can see that both sets of measurements are statistically the same. Our conclusion is that there is not any difference between the $\Lambda^0$ polarization directly produced and the $\Lambda^0$ polarization contaminated with roughly 4.2% of $\Sigma^{*-} \rightarrow \Lambda^0 \pi^-$.

### 5.2.3.3 $\Sigma^{*+} \rightarrow \Lambda^0 \pi^+$

The resonance $\Sigma^{*+}$ (1385) was also detected in our $\Lambda^0$ sample.

To determine what effect, if any, the existence of this resonance had on our measurements, the following procedure was conducted.

47

In Figure 27 we plot the invariant mass of all possible combinations of $\Lambda^0 \pi^+$. It peaks clearly around 1.385 $GeV$. In the figure we indicate the cuts ((1.33, 1.46) $GeV$) we performed on the sample around the peak of the distribution. The events inside this interval were discarded; they represent roughly 4.5% of the sample. We measure $\Lambda^0$ polarization with the rest of the events. The results of these measurements are in Table 24. In Figure 28, we compare these $\Lambda^0$ polarization measurements with the results obtained in section 5.2.1. From this figure, we can see that both sets of measurements are statistically the same. Our conclusion is that there is not any difference between the $\Lambda^0$ polarization directly produced and the $\Lambda^0$ polarization contaminated with roughly 4.5% of $\Sigma^{*+} \to \Lambda^0 \pi^+$.

## 5.3    $\Lambda^0$ Polarization as a Function of the Number of Final State Particles

We investigated if the $\Lambda^0$ polarization depends on the number of final state particles, or the number of pions in each multiplicity. We compared the 8 track final state sample results with the 6, 10, and 12 track final state samples. We separated each of these samples into $P_z < 0$ and $P_z > 0$ bins. We separated each of these bins into 5 $P_T$ bins (the same $P_T$ bins we use in measuring the 8 track sample). We measured $\Lambda^0$ polarization in each of these bins. The results are in Table 25, Table 26, and Table 27 for the 6 track, the 10 track, and the 12 track final state samples respectively. For the 6 track final state sample (see Figure 29), we lack statistics. We note that although the 6 track polarization seems to follow the behavior of $\Lambda^0$ polarization in the 8 track final state sample (see Figure 29 where we compare with those from the 8 track final state sample), the error bars are too large to allow a definitive

comparison. In both hemispheres the polarization is mirror symmetric of each other. To double the statistics, we combine the polarization from both hemispheres. The results are in Table 28 and are shown in Figure 30. From this figure it is evident that 6 track sample polarization and 8 track sample polarization have the same behavior. For 10 track final state sample, $\Lambda^0$ polarization in the forward hemisphere is consistent with the 8 track $\Lambda^0$ polarization. In the backward hemisphere $\Lambda^0$ polarization is consistent with zero. Figure 31 shows these results and the comparison with the 8 track $\Lambda^0$ polarization. For 12 track final state sample, $\Lambda^0$ polarization in the forward hemisphere is consistent with the 8 track $\Lambda^0$ polarization. In the backward hemisphere $\Lambda^0$ polarization is consistent with zero. Figure 32 shows these results and the comparison with the 8 track $\Lambda^0$ polarization.

These facts deserve a little more discussion. In section 5.1 we stated that the 6 track and the 8 track samples seem to share the same production mechanism (SSD). Either the beam proton or the target proton dissociates to give birth to the $\Lambda^0$. In this case, the $P_z$ variable seems to work very well in separating both hemispheres (the $\Lambda^0$'s from the target proton are preferentially in the $P_z < 0$ hemisphere and the $\Lambda^0$'s from the beam proton are preferentially in the $P_z > 0$ hemisphere). The 6 track sample polarization and the 8 track sample polarization (in the backward hemisphere and in the forward hemisphere) have the same behavior as a function of $P_T$, as we stated above.

We have stated also in section 5.1 that the 10 track sample and the 12 track sample share the same production mechanism (DDD), where either the beam proton or the target proton dissociate to produce the $\Lambda^0$. In this case, the

49

$P_z$ variable is not enough of a criterion to separate the $\Lambda^0$'s produced via the dissociation of the target proton, $P_z < 0$, from the $\Lambda^0$'s produced via the dissociation of the beam proton, $P_z > 0$.

We compare, for $P_z > 0$ and $P_z < 0$, the $\Lambda^0$ polarization measurements of the 6 track, the 8 track, the 10 track, and the 12 track samples. In Figure 33, we compare the results, in the forward hemisphere, between the different samples. From this figure, we can see that the $\Lambda^0$ polarization is statistically the same for all final state multiplicity particle samples. In Figure 34, we make the same comparison, but in the backward hemisphere. From this figure, we see that the $\Lambda^0$ polarization for the 10 track and for the 12 track samples is consistent with zero -- clearly different from the 6 track and the 8 track $\Lambda^0$ polarization. This is a surprising result. It is possible that this result could be coupled to the fact that the production mechanisms seem to be different or with the difficulty of separating the two reaction hemispheres. In either case, we conclude that $\Lambda^0$ polarization, in the forward hemisphere, does not depend on the number of final state particles. Using the technique we have described, the polarization changes as a function of multiplicity in the backward hemisphere. In the backward hemisphere, $\Lambda^0$ polarization is different from zero for the 6 track and for the 8 track samples and is consistent with zero for the 10 track and for the 12 track samples. This is most likely because our technique (separation into 2 $P_z$ hemispheres) is not sufficient to identify which interacting proton produced the $\Lambda^0$.

It is important to note that these results agree with the current reported inclusive $\Lambda^0$ polarization measurements. Because as we stated in section

50

1.4.2, in inclusive reactions only $\Lambda^0$ polarization measurements in the $P_z > 0$ hemisphere have been carried out.

## 5.4    Consistency Checks

We performed two consistency checks of the technique used to extract $\Lambda^0$ polarization.

First, in 8 track $\Lambda^0$ polarization measurements, we checked our measurement procedures by determining the polarization (expected to be zero) of a sample of exclusive $K_s^0$'s. The analysis procedures were identical to the $\Lambda^0$ 8 track final state sample. We substituted the $p$ from $\Lambda^0$ for the $\pi^+$ from $K_s^0$. The results along the $n_y$ direction are in Table 29. The measured $K_s^0$ polarization is consistent with zero along this direction, for both hemispheres, see Figure 35. These results were statistically unchanged by acceptance corrections (see section 6.2.3).

As a second consistency check, we analyzed an 8 track Monte Carlo sample that was created with known polarization, see section 6.2.4. We followed exactly the same procedure as with the data. The results are in Table 30, for the $n_y$ direction. The results are the same -- inside the statistical uncertainties -- the polarization we put into the sample. The polarization agrees between generated and measured for both hemispheres. See Figure 36.

## 5.5    Other Components of the Polarization

So far we have not discussed $\Lambda^0$ polarization components that are in the creation plane (according to our convention, the $\Lambda^0$ polarization components along the $n_x$ and along the $n_z$ directions). Any deviation from zero could be from production mechanism processes, from $\Lambda^0$ magnetic moment precession in the magnetic field, or from acceptance problems. $\Lambda^0$'s must be created with their spins normal to the creation plane. Therefore, the components of $\Lambda^0$ polarization along the $n_x$ and along the $n_z$ directions must be zero. If they are not the result of the decay of another particle or resonance. We determined that a few percent of $\Lambda^0$'s are created indirectly. In this way, we discard the first proposition.

To test the second proposition, we have calculated that the maximum precession angle of $\Lambda^0$ magnetic moment, in the magnetic field of E766 spectrometer is roughly 5.4°. With this value, the components $n_x$ and $n_z$ of the $\Lambda^0$ polarization must be less than roughly 0.035.

If the acceptance varies extremely rapidly in the variables used to measure the polarization, small uncertainties in the determination of acceptance could result in incorrect or unreliable polarization measurements. As we show in Chapter 6, Monte Carlo studies of the acceptance for the $n_x$ and $n_z$ components show that such variations do in fact exist. Thus, we are unable to measure the $n_x$ and $n_z$ components reliably.

# CHAPTER 6

## IS THE ASSUMPTION OF NO ACCEPTANCE CORRECTION JUSTIFIED?

### 6.1    Acceptance Calculation

We have assumed that the polarization measurement is not affected by either the apparatus or the analysis procedures.  To determine if this assumption is justified, we use Monte Carlo techniques to calculate the acceptance as follows.

We define the acceptance of the detector in a Monte Carlo simulation of the experiment as:

$$A_c = Acceptance = \frac{\#\ of\ accepted\ events}{\#\ of\ generated\ events} = \frac{N_A}{N_g},$$

The acceptance is a function of the reaction type, the model of the production process, and the momenta of the particles in the final state.

### 6.2    Monte Carlo Simulation

Due to the complexity of the detector, its acceptance must be studied using a Monte Carlo simulation technique.  The complete process of this technique has two steps: First, the Monte Carlo data is generated with certain characteristics, definite number of final state particles, polarization for certain

particles, and certain momentum distributions, etc. Second, the generated data is passed through the simulated detector.

### 6.2.1 Detector Simulation

We generated the particular mechanism of production; i.e., the way the particles are created, the number of particles in each event, the number of vertices, the momenta for each particle, and the decay time for unstable particles.

In a Monte Carlo simulation of the detector we use the actual characteristics of the detector. These are: the real distances between static detector components (JGG magnet, drift chambers, etc.), and the shape and the size of its components (chambers, scintillators, target, etc.). In addition we used a map of the magnetic field and the world average values [28] of particle masses.

The Monte Carlo program generated hits in the drift chambers and counts in the scintillators. Effects such as particle re-interactions, energy losses, and multiple scattering were included. The program simulated decays in flight of pions, kaons, and hyperons. It included drift chamber wire inefficiencies, drift time measurement errors, and multiple wire responses. The simulated events were written as a data set of the same form as the real data.

The Monte Carlo data was then treated as if it were real data. It was passed through the same sequence of analysis programs as the real data -- PASS1, PASS2, PASS3, and PASS4.

### 6.2.2 Monte Carlo Production of Unpolarized $\Lambda^0$

The Monte Carlo simulations of $\Lambda^0$'s have the following main features. The total available energy in the center of mass of the interaction is $7.31\,GeV$. The coordinate system is identical to the laboratory coordinate system described in section 2.4.

The first step in generating the reaction is a single diffraction dissociation $pp \rightarrow pX$. This has one proton and an $X$ system, which contains all the other particles. The transverse momentum distribution in this intermediate state is given by:

$$\frac{dN}{dP_T^2} \sim e^{-DP_T^2}.$$

This $P_T^2$ distribution is consistent with the distributions seen in the real data [25], and is termed diffraction dissociation [31].

In this intermediate state, $M_X^2$ can be expressed as:

$$M_X^2 = \varepsilon^2 + m_p^2 - \sqrt{4\varepsilon^2 \left( m_p^2 + P_Z^2 + P_T^2 \right)}$$

where $\varepsilon$ is the total center-of-mass energy, $m_p$ is the proton mass, and $P_Z$ and $P_T$ are the longitudinal and the transverse momenta of the proton in the center-of-mass frame respectively.

For each final state, different $M_X^2$ distribution functions were used. The function is given by $\frac{dN}{dM_X^2} \sim \frac{1}{M_X^r}$ , where $r$ is an integer.

In each different final state sample, the following values for $D$ and $r$ were used:

For 6 track events:    $D = 4$ and $r = 6$.

For 8 track events:    $D = 4$ and $\frac{dN}{dM_x^2} \sim C$ up to $M_x^2 = 16\,GeV^2$ and $r = 6$ for

$M_x^2 > 16\,GeV^2$.

For 10 track events:    $D = 4$ and $\frac{dN}{dM_x^2} \sim C$ up to $M_x^2 = 25\,GeV^2$ and $r = 6$ for

$M_x^2 > 25\,GeV^2$.

For 12 track events:    $D = 2$ and $r = -12$ up to $M_x^2 = 36.6\,GeV^2$ and $\frac{dN}{dM_x^2} \sim C$ for

$M_x^2 > 36.6\,GeV^2$.

For all final states the $X$ system decayed into $\Lambda^0$, $K^+$, and $N(\pi^+\pi^-)$ pairs, where $N = 1$ for six track events, $N = 2$ for eight track events, $N = 3$ for ten track events, and $N = 4$ for twelve track events. For further details of the $X$ decay algorithms, see Reference 25.

The momentum distributions for individual particles, the total momentum distributions for all particles, the position distributions for the primary vertex, and the mass and the lifetime distributions for $\Lambda^0$ are reproduced by the Monte Carlo generator. The main features of the data are reproduced by the Monte Carlo in each final state. However, the Monte Carlo simulation does not include resonances. The data contains resonances such as $\Delta^{++}(1232)$, $K^*(892)$, $\rho(770)$, $\Sigma^{*+}(1385)$, $\Sigma^{*-}(1385)$, $\Delta^0(1232)$.

Due to the finite acceptance of the spectrometer, many of the generated events do not survive the full analysis procedure. Table 31 summarizes the

number of $\Lambda^0$ events generated for each final state and the number of events accepted after the analysis and Table 32 summarizes the average acceptance in each final state multiplicity. Table 33 shows the average time spent to generate each Monte Carlo sample in a Digital Equipment Corporation VAX Station 3200.

### 6.2.3  Monte Carlo Production of $K_s^0$

For consistency checks, we produced a Monte Carlo $K_s^0$ sample in an 8 track final state. The Monte Carlo production of $K_s^0$ has the following characteristics. The system $pp$ decayed isotropically; i.e., following a phase space production (*PHSP*) model, into $2p$, $K_s^0$ and $\pi^+\pi^-\pi^+\pi^-$. The *PHSP* model is a statistical one. It considers only kinematic relations between the final state particles and supposes that it is equally probable for all the spatial directions (or all the momenta) that the final state particles can obtain. For a complete discussion of the *PHSP* model see Reference 32. The $K_s^0$ decayed following the *PHSP* model into a $\pi^+\pi^-$. Table 34 summarizes the number of $K_s^0$ events generated and the number of events accepted after the analysis.

### 6.2.4  Monte Carlo Production of Polarized $\Lambda^0$

In order to check the analysis procedures further, a Monte Carlo sample of polarized $\Lambda^0$'s was generated in the 8 track final state.

The main features were the following. The first intermediate state of the $pp$ system was the $pX$ system as described in section 6.2.2. The $X$ system

57

decayed isotropically into $\Lambda^0 K^+ \pi^+ \pi^- \pi^+ \pi^-$. The $\Lambda^0$ was assigned a polarization as described in Table 35. The polarization is a function of $P_T$.

We polarized $\Lambda^0$ in the following way:

In the coordinate system in which $\Lambda^0$ is at rest (the coordinate system defined in section 3.2), the decay proton is distributed (along the $n_y$ direction) according to the following expression:

$$\frac{dN}{d(\cos\theta_y)} = \frac{1}{2}(1 + \alpha \wp_y \cos\theta_y)$$ (2).

In order to generate the decays with this distribution, we use the technique shown below. If $R$ is a random number between 0 and 1, the following expression produces values of $\cos\theta_y$ which satisfy the distributions in equation (2).

$$R = \frac{\int_{-1}^{\cos\theta_y}\left(1 + \alpha\wp_y \cos\theta_y\right)d(\cos\theta_y)}{\int_{-1}^{+1}\left(1 + \alpha\wp_y \cos\theta_y\right)d(\cos\theta_y)}$$ (3)

The Monte Carlo assumes there is no polarization in either the $n_x$ or $n_z$ directions.

The distributions generated along $\hat{n}_x$ and along $\hat{n}_z$ axes were isotropic; i.e., with no polarization along those directions. From equation (3), if $\wp_i = 0$, $\cos\theta_i = -1 + 2*R$ $i = x, z$. If $\wp_i \neq 0$ $i = y$,

$$\cos\theta_y = \frac{-1 + \sqrt{1 + 2\alpha\wp_y(2R-1) + \left(2\alpha\wp_y\right)^2}}{\alpha\wp_y}.$$

## 6.3 Acceptance

In this section, we show that the detector acceptance does not affect our $\Lambda^0$ polarization measurements, within the statistical uncertainties, in the $n_y$ direction. The acceptance does affect polarization in the $n_x$ and in the $n_z$ directions, making it difficult to determine the $\Lambda^0$ polarization in these directions.

We discuss and compare the acceptance determined by two different Monte Carlo samples. The first sample, which we call the big statistics Monte Carlo sample (BS), was created as we explained in section 6.2.2. The second sample, which we call the small statistics Monte Carlo sample (SS), was created combining together, in different percentages, data created as we will indicate below.

These samples were created following the procedures in section 6.2.2, with the characteristics for each of the models, in each final state multiplicity, as follows:

For 6 track events:    1):    $D = 4$ and $r = 6$.

                                2):    $D = 2$ and $\dfrac{dN}{dM_x^2} \sim C$.

For 8 track events:    1):    $D = 4$, $\dfrac{dN}{dM_x^2} \sim C$ up to $M_x^2 = 16\, GeV^2$ and $r = 6$ for

                                       $M_x^2 > 16\, GeV^2$.

                                2):    $D = 2$ and $r = -12$ up to $M_x^2 = 20.6\, GeV^2$ and $\dfrac{dN}{dM_x^2} \sim C$ for          $M_x^2 > 20.6\, GeV^2$.

For 10 track events: 1): $D = 4$ and $\frac{dN}{dM_x^2} \sim C$ up to $M_x^2 = 25\,GeV^2$ and $r = 6$ for

$M_x^2 > 25\,GeV^2$.

2): $D = 2$ and $r = -12$ up to $M_x^2 = 30.6\,GeV^2$ and $\frac{dN}{dM_x^2} \sim C$ for $M_x^2 > 30.6\,GeV^2$.

For 12 track events: 1): Not created.

2): $D = 2$ and $r = -12$ up to $M_x^2 = 36.6\,GeV^2$ and $\frac{dN}{dM_x^2} \sim C$

for $M_x^2 > 36.6\,GeV^2$.

The SS sample, in each final state (except the 12 track sample), was created combining the two samples in the following percentages:

6 track events:      sample 1) 85% + sample 2) 15%

8 track events:      sample 1) 60% + sample 2) 40%

10 track events:      sample 1) 40% + sample 2) 60%

12 track events:      sample 2) 100%

In what follows, we are concerned solely with the 6 track, the 8 track, and the 10 track Monte Carlo samples, since the 12 track Monte Carlo sample does not change.

Table 36 lists the number of events generated and accepted, in each final state multiplicity, for the SS sample.

Table 37 lists the average acceptance in each final state for the SS sample. The average acceptance agrees with the BS sample average acceptance, see Table 32.

To calculate the $\cos\theta_i$ $i = x, y, z$ acceptance distributions, we divided the $\cos\theta_i$ $i = x, y, z$ range (-1, +1) in 20 equal bins, for both the accepted Monte Carlo data and the generated Monte Carlo data. The $\cos\theta_i$ $i = x, y, z$ distributions, from the accepted Monte Carlo data, divided by the corresponding $\cos\theta_i$ $i = x, y, z$ distributions, from the generated Monte Carlo data, represent the $\cos\theta_i$ $i = x, y, z$ acceptance distributions. The data $\cos\theta_i$ $i = x, y, z$ distributions divided by the corresponding acceptance distributions give us the $\cos\theta_i$ $i = x, y, z$ distributions corrected by acceptance.

For acceptance correction purposes, we use only the BS sample (~2.5 times the data), because the SS sample is not large enough (approximately 1/5 the data in each final state). In the first case, the measurement error bars are dominated by the data errors; in the second case, the measurement error bars would be dominated by the Monte Carlo errors.

### 6.3.1 Acceptance Along the $n_y$ Direction

The acceptance curves for the BS and for the SS samples, in all track samples, along the $n_y$ direction (the normal to the creation plane) are smooth, and symmetric around zero. The acceptance distributions are statistically consistent with a straight line of very small slope or with a straight line of slope consistent with zero (a constant).

In Figure 37, we show an example (from the Monte Carlo 8 track samples) of the acceptance curves along the $n_y$ direction. These distributions exhibit the same characteristics. In this figure, we compare the acceptance from the BS sample and from the SS sample. We can see that the $\cos\theta_y$ acceptance curve distributions are statistically equivalent, in each $P_T$ bin. However, we use only the BS sample distributions to correct by acceptance, because we want the error bars to be dominated by the data, not by the Monte Carlo.

Our studies indicate that in all final states, in both $P_z$ regions, and in all $P_T$ bins, the BS sample and the SS sample are equivalent. In the 6, the 8, the 10, and the 12 final state samples, we fit to a straight line (and to a constant also) the $\cos\theta_y$ acceptance distributions using the least-squares technique. The constant and the straight line fit the data very well. The $\chi^2/DOF$ is close to one, in all cases and in both hypothesis. Both fits are consistent. In 85% of the $P_T$ bins, the slope of the straight line fit is consistent with zero. In the other 15%, the slopes are very small. The results are in Tables 38, 39, 40, and 41, for the 6, the 8, the 10, and the 12 track final states respectively. In these tables we compare the slopes of the straight line fits from both Monte Carlo samples. As an example, we show in Figure 38, the comparison of the *slopes* / $\alpha$ for the straight line fits, for the 8 track BS and the 8 track SS samples. In 85% of the $P_T$ bins, the *slopes* / $\alpha$ are consistent with zero.

The slope and the intercept of the straight line fit are the parameters that really matter when we correct the data by acceptance. In the cases where the slope is consistent with zero, the acceptance does not change the data distributions; the polarization measurements remain unaltered. But in the

62

cases where the slope is not consistent with zero, the data distribution changes, and so do the polarization measurements. However, the fits in these cases were consistent with a constant also, and no matter in what complicated way the slope of the data distribution changes, the final effect on the polarization measurements is unobserved statistically. We show in section 6.4, that this is the case.

### 6.3.2  Acceptance Along the $n_x$ and $n_z$ Directions

The $\cos\theta_x$ acceptance distributions vary rapidly, are not smooth, and are not symmetric around zero. In the $P_z < 0$ region, these acceptance curves have a big positive slope. An example from the 8 track sample is in Figure 39. We compare the $\cos\theta_x$ acceptance distributions from both samples, the BS sample and the SS sample. Inside the statistical errors, they agree in both hemispheres.

The $\cos\theta_z$ acceptance distributions vary rapidly also, are not smooth, and are not symmetric around zero. In the $P_z < 0$ region, the acceptance curves have a big negative slope. An example, from the 8 track sample, is in Figure 40. We compare the $\cos\theta_z$ acceptance distributions from both samples, the BS sample and the SS sample. Inside the statistical errors, they agree in both hemispheres.

The behavior of these acceptance curve distributions, makes it impossible to determine the $\Lambda^0$ polarization along the $n_x$ and $n_z$ directions.

63

### 6.4 Comparison Between Uncorrected $\Lambda^0$ Polarization Measurements and Corrected Ones, Along the $n_y$ Direction

To show that the acceptance does not affect the $\Lambda^0$ polarization measurements along the $n_y$ direction, we corrected the data using the acceptance obtained from the BS sample. Figure 41 shows an example of $\cos\theta_y$ distributions; Figure 41a shows the $\cos\theta_y$ distribution uncorrected by acceptance, Figure 41b shows the $\cos\theta_y$ acceptance distribution, and Figure 41c shows the $\cos\theta_y$ acceptance distribution corrected by acceptance. Statistically the acceptance correction does not change the $\cos\theta_y$ distribution.

We found that the polarization results in all final states are unchanged within statistics when the acceptance corrections are applied. An example from the 8 track sample is in Table 42. Table 42 shows both sets of measurements.

In Figure 42 we compare these two sets of $\Lambda^0$ polarization measurements. We can see that, statistically, the two sets of measurements agree. Therefore, our $\Lambda^0$ polarization measurements are independent of the acceptance corrections.

Table 43 shows the same comparison in the Monte Carlo 8 track sample.

In Figure 43 we compare Monte Carlo $\Lambda^0$ polarization measurements uncorrected by acceptance with those corrected by BS sample acceptance. From this figure, we can see that both sets of measurements agree. This fact supports our previous conclusion, that our $\Lambda^0$ polarization measurements are independent of the acceptance corrections.

## 6.5    CONCLUSIONS

We have studied the polarization of $\Lambda^0$'s produced in the exclusive reactions:

$$pp \rightarrow p\Lambda^0 K^+ \pi^+ \pi^- \qquad (1)$$

$$pp \rightarrow p\Lambda^0 K^+ \pi^+ \pi^- \pi^+ \pi^- \qquad (2)$$

$$pp \rightarrow p\Lambda^0 K^+ \pi^+ \pi^- \pi^+ \pi^- \pi^+ \pi^- \qquad (3)$$

$$pp \rightarrow p\Lambda^0 K^+ \pi^+ \pi^- \pi^+ \pi^- \pi^+ \pi^- \pi^+ \pi^- \qquad (4)$$

$\Lambda^0$ polarization, in reaction (2), depends both on the Z-momentum component in the center of mass of event ($P_z$) and the transversal momentum with respect to the Z-direction ($P_T$) of the $\Lambda^0$. In the kinematic region with $P_z > 0$, the $\Lambda^0$ polarization is consistent with zero at $P_T = 0$ and decreases linearly with $P_T$ to $-0.23 \pm 0.08$ at $P_T = 1.2\,GeV$. These results agree with the current reported inclusive $\Lambda^0$ polarization measurements [1, . . . ,14]. In the kinematic region with $P_z < 0$, the $\Lambda^0$ polarization is mirror symmetric to that in the $P_z > 0$ region (the polarization is consistent with zero at $P_T = 0$ and increases linearly in $P_T$ to $+0.18 \pm 0.08$ at $P_T = 1.2\,GeV$). The dependence of $\Lambda^0$ polarization on the $P_z$ results in a net zero polarization when the entire data sample for this reaction is analyzed independently of $P_z$. We find that the observation of polarization requires the ability to distinguish in which kinematic region (forward where $P_z > 0$, backward where $P_z < 0$) the $\Lambda^0$ is produced.

$\Lambda^0$ polarization, for reaction (1), agrees with that from reaction (2). $\Lambda^0$ polarization, from reaction (3) and (4) agree with each other; and with that

from reaction (2) in the $P_z > 0$ region. In the $P_z < 0$ region the $\Lambda^0$ polarization seems to be consistent with zero. These results could be an indication of the production mechanisms. For reactions (1) and (2), the $\Lambda^0$'s are most probably created by SDD (Single Diffraction Dissociation, $P_z$ distributions have forward-backward peaks). For reactions (3) and (4), the $\Lambda^0$ are more likely created by DDD (Double Diffraction Dissociation, $P_z$ distributions peak around zero). For SDD, $P_z$ is correlated to the Z-momentum component in the center of mass of the event of the proton $(P_{zp})$; for DDD the correlation is weaker. The additional complication of the detector acceptance makes this more apparent in the $P_z < 0$ region. The absence of polarization in the DDD type reactions (3) and (4) (in the $P_z < 0$ region) could be due to our inability to distinguish uniquely the kinematic region in which the $\Lambda^0$'s are produced.

We have also studied the $\Lambda^0$ polarization dependence on the relative directions of $\Lambda^0$ and $K^+$ and $\Lambda^0$ and $p$ in the reaction (2). When the $p$ and the $\Lambda^0$ are in the same hemisphere (both $P_z < 0$ and $P_{zp} < 0$), the $P_z$ distribution peaks around zero. The $\Lambda^0$ polarization is consistent with zero (as in reaction (3) and (4) with $P_z < 0$). When $\Lambda^0$ and $K^+$ are in the same hemisphere (both $P_z > 0$ or $P_z < 0$) or in opposite hemispheres (one $P_z > 0$ and the other $P_z < 0$) and when the $\Lambda^0$ and the $p$ are in opposite hemispheres, $P_z$ distributions have backward and forward peaks. The $\Lambda^0$ polarization is consistent with the polarization measured independently of the kinematic distributions of $p$ and $K^+$. We interpret this as indicating that the determination of the $\Lambda^0$ polarization depends on the ability of the experiment to tell which proton dissociated into the $\Lambda^0$.

# APPENDICES

## I    Proton Angular Distribution

The spin of $\Lambda^0$ is different from zero [28]. In high energy collisions, a $\Lambda^0$ is created with its spin normal to the creation plane [21]. Through the weak force, a $\Lambda^0$ breaks up into a $p$ and a $\pi^-$, with 0.64 of probability [28]. The angular distribution of its decay products is not isotropic and depends on the $\Lambda^0$'s spin orientation. We now analyze with great detail the angular distribution of $\Lambda^0$ decay products and relate it to the $\Lambda^0$ polarization.

$\Lambda^0$, $p$, and $\pi$'s quantum numbers are [28]:

$$\Lambda^0\colon J^P = \left(\frac{1}{2}\right)^+ \qquad p\colon J^P = \left(\frac{1}{2}\right)^+ \qquad \pi\colon J^P = (0)^-$$

By conservation of total angular momentum:

$$\vec{J}_\Lambda = \vec{L} + \vec{S}, \quad \pm\frac{1}{2} = L \pm \frac{1}{2}$$

If

$$\frac{1}{2} = L \pm \frac{1}{2} \quad \Rightarrow \quad L = 0 \quad \text{or} \quad L = 1$$

If

$$-\frac{1}{2} = L \pm \frac{1}{2} \quad \Rightarrow \quad L = 0$$

Consider the $\Lambda^0$ rest frame coordinate system. Let the $Y$-direction be parallel to the normal of the creation plane. Let $u$ be the probability that the

$\Lambda^0$ spin points parallel to the normal of the creation plane, and let $d$ be the probability that the $\Lambda^0$ spin points anti-parallel to the normal of the creation plane.

Consider a sample of $N_0$ $\Lambda^0$'s. Let $N_\uparrow$ be the number of $\Lambda^0$'s with spin up and $N_\downarrow$ the number of $\Lambda^0$'s with spin down.

We have $N_\uparrow = N_0 u$ and $N_\downarrow = N_0 d = N_0(1-u)$. By the definition of polarization we have:

$$\wp_\Lambda = \frac{N_\uparrow - N_\downarrow}{N_\uparrow + N_\downarrow}, \text{ or } \wp_\Lambda = \frac{N_0 u - N_0(1-u)}{N_0} = 2u - 1$$

Let $\theta$ be the angle between the normal of the creation plane and the proton momentum vector. Let $W_\uparrow(\theta)$ be the angular distribution of the proton when the $\Lambda^0$ spin is parallel to the creation plane normal and $W_\downarrow(\theta)$ be the angular distribution of the proton when $\Lambda^0$ spin is anti-parallel to the creation plane normal.

If the $\Lambda^0$ spin and the $p$ spin are parallel when the $\Lambda^0$ decays, we have $L = 0$. -- *S waves*. If the $\Lambda^0$ spin and the $p$ spin are anti-parallel when $\Lambda^0$ decays, we have $L = 1$. -- *P waves*.

By parity conservation:

*Parity of $\Lambda^0$(even) = Parity of p(even) $\times$ Parity of $\pi^-$ (odd) $\times (-1)^L$*

If parity is conserved, $L = 1$. If parity is not conserved, $L = 0$.

Let $m_1$ be the Y-component of $L$ and $m_2$ be the Y-component of $p$ spin. Also, let $j_1$ and $j_2$ be the value of $L$ and the value of $p$ spin respectively.

With  $L = 0$

$$L = 0, \Rightarrow m_1 = 0$$

$$S = \frac{1}{2}, \Rightarrow m_2 = +\frac{1}{2}, -\frac{1}{2}$$

With  $L = 1$

$$L = 1, \Rightarrow m_1 = 1, 0$$

$$S = \frac{1}{2} \Rightarrow m_2 = \frac{1}{2}, -\frac{1}{2}$$

Let  $J_y$  be the $\Lambda^0$'s spin projection on the $Y$-axis.

$$J_y = m = m_1 + m_2$$

$$\frac{1}{2} = 0 + \frac{1}{2} \qquad\qquad S\ waves$$

$$\frac{1}{2} = 1 - \frac{1}{2}$$

$$P\ waves$$

$$\frac{1}{2} = 0 + \frac{1}{2}$$

*S waves*:

$$\left|J_1 J_2 J\, m\right\rangle = \underset{m_1 m_2}{\Sigma}\left|J_1 J_2 m_1 m_2\right\rangle \left\langle J_1 J_2 m_1 m_2\left|J_1 J_2 J m\right\rangle\right.$$

$$\left|0+\frac{1}{2}+\frac{1}{2}\pm\frac{1}{2}\right\rangle = \underset{m_1 m_2}{\Sigma}\left|0+\frac{1}{2}m_1 m_2\right\rangle\left\langle 0+\frac{1}{2}m_1 m_2\left|0+\frac{1}{2}\frac{1}{2}\pm\frac{1}{2}\right\rangle\right.$$

$$\left|0+\frac{1}{2}+\frac{1}{2}\pm\frac{1}{2}\right\rangle = \left|0+\frac{1}{2}0\pm\frac{1}{2}\right\rangle\left\langle 0+\frac{1}{2}0\pm\frac{1}{2}\left|0+\frac{1}{2}\frac{1}{2}\pm\frac{1}{2}\right\rangle\right.$$

$$J_\mp\left|0+\frac{1}{2}+\frac{1}{2}\pm\frac{1}{2}\right\rangle = \left|0+\frac{1}{2}+\frac{1}{2}\mp\frac{1}{2}\right\rangle$$

$$= \left|0+\frac{1}{2}0\mp\frac{1}{2}\right\rangle\left\langle 0+\frac{1}{2}0\pm\frac{1}{2}\left|0+\frac{1}{2}\frac{1}{2}\pm\frac{1}{2}\right\rangle\right.$$

$$\left|\left\langle 0+\frac{1}{2}0\pm\frac{1}{2}\left|0+\frac{1}{2}\frac{1}{2}\pm\frac{1}{2}\right\rangle\right.\right|^2 = 1$$

$$\left\langle 0+\frac{1}{2}0\pm\frac{1}{2}\left|0+\frac{1}{2}\frac{1}{2}\pm\frac{1}{2}\right\rangle\right.\left\langle 0+\frac{1}{2}0\mp\frac{1}{2}\left|0+\frac{1}{2}\frac{1}{2}\mp\frac{1}{2}\right\rangle\right. = 1$$

$$\left|0+\frac{1}{2}+\frac{1}{2}+\frac{1}{2}\right\rangle = \left|0\ 0\right\rangle\left|\frac{1}{2}\ \frac{1}{2}\right\rangle,$$

$$\left|0+\frac{1}{2}+\frac{1}{2}-\frac{1}{2}\right\rangle = \left|0\ 0\right\rangle\left|+\frac{1}{2}\ -\frac{1}{2}\right\rangle$$

*P waves*

$$\left|J_1 J_2 J m\right\rangle = \underset{m_1\ m_2}{\Sigma}\left|J_1 J_2 m_1 m_2\right\rangle\left\langle J_1 J_2 m_1 m_2\left|J_1 J_2 J m\right\rangle\right.$$

$$L = +1$$

$$m_1 = +1, 0; \quad J = L+S; \quad J = J_1 + J_2$$

$$\frac{1}{2} = 1-\frac{1}{2}$$

$$m = m_1 + m_2,$$

$$\frac{1}{2}=1-\frac{1}{2}, \quad \frac{1}{2}=0+\frac{1}{2}$$

$$\left|1+\frac{1}{2}\frac{1}{2}\frac{1}{2}\right\rangle = \sum_{m_1 m_2}\left|1+\frac{1}{2}\,m_1\,m_2\right\rangle\left\langle 1+\frac{1}{2}\,m_1\,m_2\Big|1+\frac{1}{2}\frac{1}{2}\frac{1}{2}\right\rangle$$

$$=\left|1+\frac{1}{2}+1-\frac{1}{2}\right\rangle\left\langle 1+\frac{1}{2}+1-\frac{1}{2}\Big|1+\frac{1}{2}\frac{1}{2}\frac{1}{2}\right\rangle +$$

$$\left|1+\frac{1}{2}\,0\,\frac{1}{2}\right\rangle\left\langle 1+\frac{1}{2}\,0\,\frac{1}{2}\Big|1+\frac{1}{2}\frac{1}{2}\frac{1}{2}\right\rangle$$

$$=\left|1\,1\right\rangle\left|+\frac{1}{2}-\frac{1}{2}\right\rangle\left\langle 1+\frac{1}{2}+1-\frac{1}{2}\Big|1+\frac{1}{2}\frac{1}{2}\frac{1}{2}\right\rangle +$$

$$\left|1\,0\right\rangle\left|+\frac{1}{2}\frac{1}{2}\right\rangle\left\langle 1+\frac{1}{2}\,0\,\frac{1}{2}\Big|1+\frac{1}{2}\frac{1}{2}\frac{1}{2}\right\rangle$$

$$J_+\left|1+\frac{1}{2}\frac{1}{2}\frac{1}{2}\right\rangle=\left(J_{1+}+J_{2+}\right)\left\{\begin{array}{l}\left|1\,1\right\rangle\left|+\frac{1}{2}-\frac{1}{2}\right\rangle\left\langle 1+\frac{1}{2}+1-\frac{1}{2}\Big|1+\frac{1}{2}\frac{1}{2}\frac{1}{2}\right\rangle \\[2mm] +\left|1\,0\right\rangle\left|+\frac{1}{2}\frac{1}{2}\right\rangle\left\langle 1+\frac{1}{2}\,0\,\frac{1}{2}\Big|1+\frac{1}{2}\frac{1}{2}\frac{1}{2}\right\rangle\end{array}\right\}$$

Using

$$J_\pm\left|\alpha\,j\,m\right\rangle=\left((j\mp m)(j\pm m+1)\right)^{\frac{1}{2}}\left|\alpha\,j\,m\pm 1\right\rangle$$

$$J_+\left|1+\frac{1}{2}\frac{1}{2}\frac{1}{2}\right\rangle=\left|1\,1\right\rangle\left|+\frac{1}{2}+\frac{1}{2}\right\rangle\left\langle 1+\frac{1}{2}+1-\frac{1}{2}\Big|1+\frac{1}{2}\frac{1}{2}\frac{1}{2}\right\rangle +$$

$$[2]^{\frac{1}{2}}\left|1\,1\right\rangle\left|+\frac{1}{2}\frac{1}{2}\right\rangle\left\langle 1+\frac{1}{2}\,0\,\frac{1}{2}\Big|1+\frac{1}{2}\frac{1}{2}\frac{1}{2}\right\rangle=0$$

$$\left\langle 1+\frac{1}{2}+1-\frac{1}{2}\Big|1+\frac{1}{2}\frac{1}{2}\frac{1}{2}\right\rangle=-[2]^{\frac{1}{2}}\left\langle 1+\frac{1}{2}\,0\,\frac{1}{2}\Big|1+\frac{1}{2}\frac{1}{2}\frac{1}{2}\right\rangle$$

With normalization

$$\left|\left\langle 1+\frac{1}{2}+1-\frac{1}{2}\Big|1+\frac{1}{2}\frac{1}{2}\frac{1}{2}\right\rangle\right|^{\frac{1}{2}} + \left|\left\langle 1+\frac{1}{2}\,0\,\frac{1}{2}\Big|1+\frac{1}{2}\frac{1}{2}\frac{1}{2}\right\rangle\right|^{\frac{1}{2}}=1$$

We have

$$\left\langle 1+\frac{1}{2}\ 0\ \frac{1}{2}\Bigg| 1+\frac{1}{2}\ \frac{1}{2}\ \frac{1}{2}\right\rangle = \pm\sqrt{\frac{1}{3}}$$

$$\left\langle 1+\frac{1}{2}\ +1\ -\frac{1}{2}\Bigg| 1+\frac{1}{2}\ \frac{1}{2}\ \frac{1}{2}\right\rangle = \mp\sqrt{\frac{2}{3}}$$

$$\left| 1+\frac{1}{2}\ \frac{1}{2}\ \frac{1}{2}\right\rangle = \sqrt{\frac{2}{3}}\,|1\ 1\rangle\left|\frac{1}{2}\ -\frac{1}{2}\right\rangle - \sqrt{\frac{1}{3}}\,|1\ 0\rangle\left|\frac{1}{2}\ \frac{1}{2}\right\rangle$$

*P waves*

$$\left| J_1\ J_2\ J\ m\right\rangle = \sum_{m_1\ m_2}\left| J_1\ J_2\ m_1\ m_2\right\rangle\left\langle J_1\ J_2\ m_1\ m_2\Big| J_1\ J_2\ J\ m\right\rangle$$

$$L = +1$$

$$m_1 = -1,\quad 0,\quad J = L+S,\quad J = J_1 + J_2$$

$$+\frac{1}{2} = +1 - \frac{1}{2},\qquad J = J_1 + J_2 - 1$$

$$m = m_1 + m_2$$

$$-\frac{1}{2} = -1 + \frac{1}{2}$$

$$-\frac{1}{2} = 0 - \frac{1}{2}$$

$$\left| 1+\frac{1}{2}\ \frac{1}{2}\ -\frac{1}{2}\right\rangle = \sum_{m_1\ m_2}\left| 1+\frac{1}{2}\ m_1\ m_2\right\rangle\left\langle 1+\frac{1}{2}\ m_1\ m_2\Big| 1+\frac{1}{2}\ \frac{1}{2}\ -\frac{1}{2}\right\rangle$$

$$= \left| 1+\frac{1}{2}\ -1\ \frac{1}{2}\right\rangle\left\langle 1+\frac{1}{2}\ -1\ \frac{1}{2}\Big| 1+\frac{1}{2}\ \frac{1}{2}\ -\frac{1}{2}\right\rangle +$$

$$\left| 1+\frac{1}{2}\ 0\ -\frac{1}{2}\right\rangle\left\langle 1+\frac{1}{2}\ 0\ -\frac{1}{2}\Big| 1+\frac{1}{2}\ \frac{1}{2}\ -\frac{1}{2}\right\rangle$$

$$= \left| 1\ -1\right\rangle\left| +\frac{1}{2}\ \frac{1}{2}\right\rangle\left\langle 1+\frac{1}{2}\ -1\ \frac{1}{2}\Big| 1+\frac{1}{2}\ \frac{1}{2}\ -\frac{1}{2}\right\rangle +$$

$$\left| 1\ 0\right\rangle\left| \frac{1}{2}\ -\frac{1}{2}\right\rangle\left\langle 1+\frac{1}{2}\ 0\ -\frac{1}{2}\Big| 1+\frac{1}{2}\ \frac{1}{2}\ -\frac{1}{2}\right\rangle$$

$$J_-\left| 1+\frac{1}{2}\ \frac{1}{2}\ -\frac{1}{2}\right\rangle = 0 = (J_{1-} + J_{2-})\left[\begin{array}{l}\left| 1\ -1\right\rangle\left| +\frac{1}{2}\ \frac{1}{2}\right\rangle\left\langle 1+\frac{1}{2}\ -1\ \frac{1}{2}\Big| 1\ \frac{1}{2}\ \frac{1}{2}\ -1\right\rangle + \\[2mm] \left| 1\ 0\right\rangle\left| \frac{1}{2}\ -\frac{1}{2}\right\rangle\left\langle 1\ \frac{1}{2}\ 0\ -\frac{1}{2}\Big| 1+\frac{1}{2}\ \frac{1}{2}\ -\frac{1}{2}\right\rangle\end{array}\right]$$

72

If we consider:

$$J_-|\alpha\,j\,m\rangle=[(j+m)(j-m+1)]^{\frac{1}{2}}|\alpha\,j\,m-1\rangle$$

we have

$$J_-\left|1+\frac{1}{2}\frac{1}{2}-\frac{1}{2}\right\rangle=0=|1-1\rangle\left|\frac{1}{2}-\frac{1}{2}\right\rangle\left\langle1+\frac{1}{2}-1\frac{1}{2}\right|1\frac{1}{2}\frac{1}{2}-1\right\rangle+$$

$$(2)^{\frac{1}{2}}|1-1\rangle\left|\frac{1}{2}-\frac{1}{2}\right\rangle\left\langle1\frac{1}{2}0-\frac{1}{2}\right|1+\frac{1}{2}\frac{1}{2}-\frac{1}{2}\right\rangle$$

$$=0$$

$$\left\langle1+\frac{1}{2}-1\frac{1}{2}\right|1\frac{1}{2}\frac{1}{2}-1\right\rangle+(2)^{\frac{1}{2}}\left\langle1\frac{1}{2}0-\frac{1}{2}\right|1+\frac{1}{2}\frac{1}{2}-\frac{1}{2}\right\rangle=0$$

$$\left|\left\langle1+\frac{1}{2}-1\frac{1}{2}\right|1\frac{1}{2}\frac{1}{2}-1\right\rangle\right|^2+\left|\left\langle1\frac{1}{2}0-\frac{1}{2}\right|1+\frac{1}{2}\frac{1}{2}-\frac{1}{2}\right\rangle\right|^2=1$$

$$\left\langle1+\frac{1}{2}-1\frac{1}{2}\right|1\frac{1}{2}\frac{1}{2}-\frac{1}{2}\right\rangle=-\sqrt{\frac{2}{3}}$$

$$\left\langle1\frac{1}{2}0-\frac{1}{2}\right|1+\frac{1}{2}\frac{1}{2}-\frac{1}{2}\right\rangle=\sqrt{\frac{1}{3}}$$

$$\left|1+\frac{1}{2}\frac{1}{2}-\frac{1}{2}\right\rangle=-\sqrt{\frac{2}{3}}|1-1\rangle\left|+\frac{1}{2}\frac{1}{2}\right\rangle+\sqrt{\frac{1}{3}}|1\,0\rangle\left|\frac{1}{2}-\frac{1}{2}\right\rangle$$

Let $a_{p\uparrow}$ be the probability amplitude for $P$ *waves* and $a_{s\uparrow}$ be the probability amplitude for $S$ *waves* when the $\Lambda^0$ spin is parallel to the normal of the creation plane.

The probability amplitude can be written as:

$$\psi_\uparrow=\left[\sqrt{\frac{2}{3}}|1\,1\rangle\left|\frac{1}{2}-\frac{1}{2}\right\rangle-\sqrt{\frac{1}{3}}|1\,0\rangle\left|\frac{1}{2}\frac{1}{2}\right\rangle\right]a_{p\uparrow}+|0\,0\rangle\left|\frac{1}{2}\frac{1}{2}\right\rangle a_{s\uparrow}$$

And the probability density as:

$$\psi_\uparrow^* \, \psi_\uparrow = \left[\left(\sqrt{\frac{2}{3}}|1\,1\rangle^* \left|\frac{1}{2}-\frac{1}{2}\right\rangle^* - \sqrt{\frac{1}{3}}|1\,0\rangle^* \left|\frac{1}{2}\,\frac{1}{2}\right\rangle^*\right) a_{P\uparrow}^* + \left(|0\,0\rangle^* \left|\frac{1}{2}\,\frac{1}{2}\right\rangle^* a_{S\uparrow}^*\right)\right]$$

$$\left[\left(\sqrt{\frac{2}{3}}|1\,1\rangle \left|\frac{1}{2}-\frac{1}{2}\right\rangle - \sqrt{\frac{1}{3}}|1\,0\rangle \left|\frac{1}{2}\,\frac{1}{2}\right\rangle\right) a_{P\uparrow} + \left(|0\,0\rangle \left|\frac{1}{2}\,\frac{1}{2}\right\rangle\right) a_{S\uparrow}\right]$$

$$= \left(\frac{2}{3}|1\,1\rangle|^2 + \frac{1}{3}|1\,0\rangle|^2\right)|a_{P\uparrow}|^2 - \sqrt{\frac{1}{3}}|1\,0\rangle|0\,0\rangle^* \, a_{S\uparrow}^* \, a_{P\uparrow} -$$

$$\sqrt{\frac{1}{3}}|1\,0\rangle^* |0\,0\rangle a_{S\uparrow} \, a_{P\uparrow}^* + |0\,0\rangle|^2 \, |a_{S\uparrow}|^2$$

As :

$$|0\,0\rangle = Y_0^0 = 1$$

$$|1\,1\rangle = Y_1^1 = -\left(\frac{3}{2}\right)^{\frac{1}{2}} \sin\theta$$

$$|1\,0\rangle = Y_1^0 = (3)^{\frac{1}{2}} \cos\theta$$

$$\psi_\uparrow^* \, \psi_\uparrow = |a_{P\uparrow}|^2 + |a_{S\uparrow}|^2 - \left(a_{S\uparrow}^* \, a_{P\uparrow} + a_{S\uparrow} a_{P\uparrow}^*\right) \cos\theta$$

$$\psi_\uparrow^* \, \psi_\uparrow = \left(|a_{P\uparrow}|^2 + |a_{S\uparrow}|^2\right)\left(1 - \frac{2\,\mathrm{Re}\left(a_{S\uparrow} a_{P\uparrow}^*\right)}{|a_{P\uparrow}|^2 + |a_{S\uparrow}|^2}\right) \cos\theta$$

When the $\Lambda^0$ spin is parallel to the normal of the creation plane, the angular distribution is given by:

$$W_\uparrow(\theta) = \frac{\psi_\uparrow^* \, \psi_\uparrow}{|a_{P\uparrow}|^2 + |a_{S\uparrow}|^2} = (1 + \alpha\cos\theta)$$

where

$$\alpha = -\frac{2\,\mathrm{Re}(a_{S\uparrow} a_{P\uparrow}^*)}{|a_{P\uparrow}|^2 + |a_{S\uparrow}|^2}$$

74

Let $a_{P\downarrow}$ be the probability amplitude for $P$ waves and $a_{s\downarrow}$ the probability amplitude for $S$ waves for the decay of a $\Lambda^{0}$ when its spin points down in the creation plane. The probability amplitude can be written as:

$$\psi_{\downarrow} = \left[\left(-\sqrt{\frac{2}{3}}\left|1\ -1\right\rangle\left|\frac{1}{2}\ \frac{1}{2}\right\rangle + \sqrt{\frac{1}{3}}\left|1\ 0\right\rangle\left|\frac{1}{2}\ -\frac{1}{2}\right\rangle\right)a_{P\downarrow} + \left(\left|0\ 0\right\rangle\left|\frac{1}{2}\ -\frac{1}{2}\right\rangle\right)a_{s\downarrow}\right]$$

And the probability density:

$$\psi_{\downarrow}^{*}\psi_{\downarrow} = \left(\frac{2}{3}\left||1-1\rangle\right|^{2} + \frac{1}{3}\left||10\rangle\right|^{2}\right)\left|a_{P\downarrow}\right|^{2} + \sqrt{\frac{1}{3}}\langle00|^{*}|10\rangle a_{s\downarrow}^{*}a_{P\downarrow} +$$
$$\sqrt{\frac{1}{3}}\langle10|^{*}|00\rangle a_{P\downarrow}^{*}a_{s\downarrow} + \left||00\rangle\right|^{2}\left|a_{s\downarrow}\right|^{2}$$

If we use:

$$\left|0\ 0\right\rangle = Y_{0}^{0} = 1$$

$$\left|1\ 0\right\rangle = Y_{1}^{0} = (3)^{\frac{1}{2}}\cos\theta$$

$$\left|1-1\right\rangle = Y_{1}^{-1} = +\left(\frac{3}{2}\right)^{\frac{1}{2}}\sin\theta$$

we obtain for the probability density:

$$\psi_{\downarrow}^{*}\psi_{\downarrow} = \left|a_{P\downarrow}\right|^{2} + \left|a_{s\downarrow}\right|^{2} + \left(a_{s\downarrow}^{*}a_{P\downarrow} + a_{P\downarrow}^{*}a_{s\downarrow}\right)\cos\theta$$

and for the angular distribution:

$$W_{\downarrow}(\theta) = \frac{\psi_{\downarrow}^{*}\psi_{\downarrow}}{\left|a_{P\downarrow}\right|^{2} + \left|a_{s\downarrow}\right|^{2}} = 1 + \frac{2\,\mathrm{Re}(a_{s\downarrow}a_{P\downarrow}^{*})}{\left|a_{P\downarrow}\right|^{2} + \left|a_{s\downarrow}\right|^{2}}\cos\theta$$

with

$$\alpha = -\frac{2\,\mathrm{Re}(a_{s\downarrow}a_{P\downarrow}^{*})}{\left|a_{P\downarrow}\right|^{2} + \left|a_{s\downarrow}\right|^{2}}$$

75

The angular distribution, when the $\Lambda^0$ spin is anti-parallel to the normal of the creation plane is given by:

$$W_\downarrow(\theta) = 1 - \alpha \cos\theta$$

The total angular distribution is:

$$\frac{dN}{d\Omega} = uW_\uparrow(\theta)N_0 + (1-u)W_\downarrow(\theta)N_0$$
$$= (u + \alpha u \cos\theta + 1 - \alpha \cos\theta - u + \alpha u \cos\theta)N_0$$
$$= (1 - (1-2u)\alpha \cos\theta)N_0 = (1 + \alpha \wp_\Lambda \cos\theta)N_0$$
$$\frac{dN}{d\Omega} = (1 + \alpha \wp_\Lambda \cos\theta)N_0$$

If we normalize to $N_0$, we can write the last equation as:

$$\frac{dN}{d\Omega} = \frac{N_0}{4\pi}(1 + \alpha \wp_\Lambda \cos\theta)$$

76

## II    Errors

### 1.    Fitting N Points to a Straight Line $y_i = b + mx_i$

The minimum $\chi^2$ or least-squares technique to fit $n$ points, with values $P(x_j)$ and with variance $\sigma_j$, to a given distribution $f(x_j)$ is accomplished by minimizing the valued of $\chi^2$ given by Equation 1.

$$\chi^2 \equiv \sum_{j=1}^{n} \frac{[f(x_j) - P(x_j)]^2}{\sigma_j^2} \tag{1}$$

The $\chi^2$ characterizes the dispersion of the observed frequencies, $P(x_j)$, from the expected frequencies, $f(x_j)$.

If the observed frequencies agree exactly with the predicted ones $f(x_j) = P(x_j)$, then $\chi^2 = 0$. The larger the $\chi^2$ values, the larger the deviations from the assumed distribution. So, the smaller the $\chi^2$, the better the assumed distribution.

Sometimes the reduced $\chi^2$ is used:

$$\chi^2_{DOF} \equiv \chi^2 / DOF,$$

where DOF means the degrees of freedom (number of points to fit minus the number of constraints). If $\chi^2 / DOF$ is close to 1 or less than 1, it means that the assumed distribution fits the observed data well.

For the particular case of to a straight line, $f(x_j) = b + mx_j$. It is well known [33] that

$$m = \frac{\sum_i \frac{x_i y_i}{\sigma_i^2} \sum_i \frac{1}{\sigma_i^2} - \sum_i \frac{y_i}{\sigma_i^2} \sum_i \frac{x_i}{\sigma_i^2}}{Det}$$

and

$$b = -\frac{\sum_i \frac{x_i y_i}{\sigma_i^2} \sum_i \frac{x_i}{\sigma_i^2} - \sum_i \frac{y_i}{\sigma_i^2} \sum_i \frac{x_i^2}{\sigma_i^2}}{Det}$$

with

$$Det = \left( \sum_i \frac{x_i^2}{\sigma_i^2} \right) \left( \sum_i \frac{1}{\sigma_i^2} \right) - \left( \sum_i \frac{x_i}{\sigma_i^2} \right)^2.$$

As *Det* is not a function of $y_i$ and because for the normal distribution $\sigma_{y_i}^2 = y_i$, the standard deviations for *m* and *b* are given by:

$$\sigma_m^2 = \frac{\sum_i \frac{1}{\sigma_i^2}}{Det}$$

and

$$\sigma_b^2 = \frac{\sum_i \frac{x_i^2}{\sigma_i^2}}{Det}$$

respectively.

## 1.2 Determination of Uncertainties in $\Lambda^0$ Polarization

### 1.2.1 Correlated Variables

Consider the acceptance $A_{Ci}$.

$$A_{Ci} = \frac{N_{Ai}}{N_{Gi}},$$

where $A_{Ci}$ is the probability of accepting $N_{Ai}$ $\Lambda^0$'s of the total number generated $N_{Gi}$ $\Lambda^0$'s in the bin $i$. Of course, $N_{Gi} \geq N_{Ai}$. Thus:

$$A_{Ci} = \frac{N_{Ai}}{N_{Gi}}$$

follows a binomial distribution because an event is accepted $(N_{Ai})$ or not accepted $(\overline{N}_{Ai})$ and always $N_{Gi} \geq N_{Ai}$. This distribution is given by:

$$P(N_A, N_G) = \frac{N_G!}{N_A!(N_G - N_A)!} \, p^{N_A}(1-p)^{N_G - N_A}$$

where $p$ is the probability of accepting an event. The probability density function is given by:

$$\ell(p) = P(N_A, N_G).$$

To find the uncertainty in a variable where the variables are related or correlated, we use the maximum likelihood method. By this method:

$$\omega = \ln \ell(p),$$

$$\omega = N_A \ln p + (N_G - N_A)\ln(1 - p) + \ln N_G! - \ln N_A! - \ln(N_G - N_A)!.$$

And we have:

$$\left.\frac{\partial \omega}{\partial p}\right|_{p=p^*} = \frac{N_A}{p} - \left.\frac{N_G - N_A}{(1-p)}\right|_{p=p^*} \quad \text{with } p^* = \frac{N_A}{N_G}.$$

And as:

$$\frac{\partial^2 \omega}{\partial p^2} = -\frac{N_A}{p^2} - \frac{N_G - N_A}{(1-p)^2};$$

we have that:

$$\sigma_{p^*}^2 \equiv \left[ -\left.\frac{\partial^2 \omega}{\partial p^2}\right|_{p=p^*} \right]^{-1}$$

and

$$\sigma_{p^*}^2 = \frac{N_A^2}{N_G^2}\left( \frac{1}{N_A} - \frac{1}{N_G} \right)$$

The uncertainty is given by:

$$\sigma_A = \frac{N_A}{N_G}\left( \frac{1}{N_A} - \frac{1}{N_G} \right)^{\frac{1}{2}}.$$

## 1.2.2 Uncorrelated Variables

Consider the polarization $\wp_y$:

$$\wp_y = \frac{m}{b\alpha},$$

where $m \pm \sigma_m$ and $b \pm \sigma_b$ are the parameters from the fitting of the $\cos\theta_y$ distributions to a straight line. $\alpha \pm \sigma_\alpha$ is the asymmetry parameter, and $\wp_y$ is the polarization. This is an example of uncorrelated variables.

If $f = f(x_1, x_2, \ldots x_n)$ where $x_i, i = 1, 2, \ldots, n$ are uncorrelated. The uncertainty $\sigma_f^2$ is given by:

$$\sigma_f^2 = \sum_i^n \left( \frac{\partial f}{\partial x_i} \right)^2 \sigma_{x_i}^2.$$

## 1.3   Error Propagation

In the $\Lambda^0$ polarization measurements, the errors were propagated through the following steps:

1)   We plotted $\cos\theta_y$, for each of the $P_T$ bins, as we described in section 4.3. We fitted this distribution to a straight line using the least-squares technique. If we had not corrected by acceptance, then $\sigma_{Ai}^2 \equiv N_i$. This last statement is following a Gaussian distribution.

2)   We determined the acceptance for each of the $P_T$ bins, as we explained in section 6.3. The acceptance for each $\cos\theta_y$ distribution bins is given by:

$$A_{Ci} = \frac{N_{Ai}}{N_{Gi}},$$

with $N_{Gi} = N_{Ai} + \overline{N}_{Ai}$ and $N_{Gi} \geq N_{Ai}$.

3)   We corrected the real data $\cos\theta_y$ distributions, bin to bin, by the acceptance. We obtained the uncertainties by the following way: from the number of entries in the bin $i$,

$$N_{Ci} = \frac{N_{ri}}{A_{Ci}},$$

we took $N_{ri}$ and $A_{ci}$ as uncorrelated variables. $N_{ri}$ is the number of real events inside the bin $i$ and $A_{ci}$ is the acceptance for the bin $i$. Following the procedure of this Appendix section 1.2.2, the uncertainty in $N_{ci}$ is given by:

$$\sigma_{Ci} = \frac{N_{ri}N_{Gi}}{N_{Ai}}\left(\frac{1}{N_{ri}} + \frac{1}{N_{Ai}} - \frac{1}{N_{Gi}}\right)^{\frac{1}{2}} \tag{2}$$

We fitted the $\cos\theta_y$ distribution that was corrected by acceptance to a straight line $y_{ci} = b + m\cos\theta_{yi}$ using the least-squares method. Then we obtained:

$$\frac{N_0}{4\pi}\left(1 + \alpha\,\wp_y\cos\theta_{yi}\right) = b + m\cos\theta_{yi}$$

and

$$m = \frac{N_0}{4\pi}\alpha\wp_y, \quad b = \frac{N_0}{4\pi}, \quad \wp_y = \frac{m}{\alpha b}.$$

We took the variables $m, \alpha$, and $b$ as uncorrelated. Following the procedure of this Appendix section 1.2.2, the uncertainty in the polarization $\sigma_{\wp_y}$ is given by:

$$\sigma_{\wp_y} = \frac{m}{b\alpha}\left[\left(\frac{\sigma_m}{m}\right)^2 + \left(\frac{\sigma_b}{b}\right)^2 + \left(\frac{\sigma_\alpha}{\alpha}\right)^2\right]^{\frac{1}{2}} \tag{3}$$

# REFERENCES

1.  A. Lesnik, et al., Phys. Rev. Lett. 35, 770 (1975).

2.  G. Bunce, et al., Phys. Rev. Lett. 19, 1113 (1976).

3.  K. Heller, et al., Phys. Lett. 5, 480 (1977).

4.  F. Lomanno, et al., Phys. Rev. Lett. 26, 1905 (1979).

5.  F. Abe, et al., Phys. Rev. Lett. 15, 1102 (1983).

6.  S. Erhan, et al., Phys. Lett. 2, 301 (1979).

7.  K. Raychaudhuri, et al., Phys. Lett. 3, 319 (1980).

8.  K. Heller, et al., Phys. Rev. Lett. 9, 607 (1978).

9.  F. Abe, et al., Journal of the Physical Society of Japan Vol.52, No. 12, December, 1983, pp. 4107-4117.

10. P. Aahlin, et al., Lettere al Nuovo Cimento. 21, N. 7 236 (1978).

11. A.M. Smith, et al., Phys. Lett. B 1, and 2, 209 (1987).

12. BIS-2 Collaboration, Sov. J. Phys. 37(6), June 1983.

13. V. Blobel, et al., Nuclear Physics B122 (1977) 429-434.

14. Yu. D. Aleshin, et al., Sov. J. Nucl. Phys., 20(6), May 1975.

15. S.M. Troshin, et al., Sov. J. Nucl. Phys., 38(4), October 1983.

16. Thomas A. DeGrand, et al., Phys. Rev. D 24, 2419 (1981).

17. K.J.M. Moriarty, et al., Lettere al Nuovo Cimento. 17, N. 11 366 (1976).

18. B. Andersson, et al., Phys. Lett. 4, 85B (1979).

19. J. Szwed, et al., Phys. Lett. 5, 105B (1981).

20. T. Henkes, et al., Phys. Lett. B 283 (1992).

21. Donald K. Perkins, "Introduction to High Energy Physics", (Addison Wesley, 1987).

22. K. Keller, in Proceedings of the Seventh International Conference on Polarization Phenomena in Nuclear Physics, Paris, 1990, edited by A. Boudard and Y. Terrien [J. Phys. (Paris), Colloq. 51, C6-163 (1990)].

23. M.D. Church, Columbia University Ph.D. dissertation, "$\Xi^-$ Production in 15-28 GeV Neutron-Proton Interactions", Nevis R# 260, (1986).

24. B.J. Stern, Columbia University Ph.D. dissertation, "A Search for Charmed Particles in 15-28 GeV Neutron-Proton Interactions", Nevis R# 266, (1988).

25. E.E. Gottschalk, Columbia University Ph.D. dissertation, "Strange Baryon Production in 27.5 GeV/c Proton-Proton Interactions", Nevis R# 278 (1992).

26. M.J. Forbush, Texas A & M University Ph.D. dissertation, "High Mass Diffractive Dissociation at 27.5 GeV Proton-Proton Interactions in Exclusive Final States", (1990).

27. L.R. Wiencke, Columbia University Ph.D. dissertation, "Observation of Final State Coulomb Interactions in Proton-Proton Collisions at 27.5 GeV/c", Nevis R# 280 (1992).

28. Particle Data Group, Phys. Rev., D45, VII.37 (1992).

29. J. Uribe, University of Massachusetts Ph.D. Dissertation, "Pion-Pion Correlations at Low Relative Momentum Produced in the Reactions $pp \rightarrow pp(\pi^+\pi^-)^n$ with $n = 2, 3, 4, 5, 6$", UMAHEP 385 (1993).

30. M.W. Sullivan, et al., Phys. Rev. D 36 674 (1987).

31. K. Goulianos, Phys. Rep. 101, No. 3 (1983).

32. R. Hagedorn, "Relativistic Kinematics", (W.A. Benjamin, Inc. 1963).

33. Philip R. Bevington. "Data Reduction and Error Analysis for the Physical Sciences", McGraw-Hill Book Company, New York, 1969.

# TABLES

**TABLE 1.**

Main features of the used $\Lambda^0$ sample.

| Final state multiplicity particles | Average number of solutions per event | Number of events from all triggers |
|---|---|---|
| 6 | 1.2 | 4521 |
| 8 | 1.5 | 57455 |
| 10 | 2.0 | 54266 |
| 12 | 2.5 | 16381 |

**TABLE 2.**

Estimated percentage of the background in each final state.

| Final state multiplicity particles | Background (%) |
|---|---|
| 6 | 12.0 |
| 8 | 10.8 |
| 10 | 11.2 |
| 12 | 11.0 |

**TABLE 3.**

Characteristics of the $\Lambda^0$ sample used to study polarization.

| Final state multiplicity particles | Average number of solutions per event | Number of events from all triggers after PASS4 |
|---|---|---|
| 6 | 1.1 | 3978 |
| 8 | 1.2 | 51195 |
| 10 | 1.4 | 48195 |
| 12 | 1.6 | 14582 |

**TABLE 4.**

Bins for $P_T$.

| Bin | Range $(GeV)$ | $\overline{P}_T\ (GeV)$ |
|-----|---------------|-------------------------|
| 1 | 0.000 -- 0.264 | 0.132 |
| 2 | 0.264 -- 0.528 | 0.396 |
| 3 | 0.528 -- 0.792 | 0.660 |
| 4 | 0.792 -- 1.056 | 0.924 |
| 5 | 1.056 -- 1.320 | 1.188 |

**TABLE 5.**

$\Lambda^0$ polarization for the entire 8 track final state sample.

$|P_z| \leq 3.2\ GeV$

| $\overline{P}_T(GeV)$ | $\wp_y \pm \Delta\wp_y$ | $\chi^2/(DOF = 18)$ |
|-----------------------|-------------------------|---------------------|
| 0.132 | $-0.004 \pm 0.049$ | 0.98 |
| 0.396 | $-0.017 \pm 0.032$ | 2.24 |
| 0.66 | $0.020 \pm 0.024$ | 3.85 |
| 0.924 | $0.017 \pm 0.022$ | 1.08 |
| 1.188 | $0.008 \pm 0.031$ | 1.49 |

**TABLE 6.**

$\Lambda^0$ polarization for the 8 track final state sample.

(a)  $P_z \leq 0$

| $\overline{P}_T (GeV)$ | $\wp_y \pm \Delta \wp_y$ | $\chi^2/(DOF = 18)$ |
|---|---|---|
| 0.132 | $0.028 \pm 0.035$ | 1.34 |
| 0.396 | $0.025 \pm 0.027$ | 2.02 |
| 0.660 | $0.128 \pm 0.032$ | 2.42 |
| 0.924 | $0.097 \pm 0.046$ | 1.93 |
| 1.188 | $0.183 \pm 0.072$ | 1.18 |

(b)  $P_z > 0$

| $\overline{P}_T (GeV)$ | $\wp_y \pm \Delta \wp_y$ | $\chi^2/(DOF = 18)$ |
|---|---|---|
| 0.132 | $-0.020 \pm 0.046$ | 0.70 |
| 0.396 | $0.003 \pm 0.032$ | 1.69 |
| 0.660 | $-0.114 \pm 0.037$ | 1.47 |
| 0.924 | $-0.196 \pm 0.052$ | 1.89 |
| 1.188 | $-0.232 \pm 0.084$ | 1.09 |

**TABLE 7.**

Bins for $P_z$.

| Bin | Range $(GeV)$ | $\overline{P}_z (GeV)$ |
|---|---|---|
| 1 | -3.2 -- -2.0 | -2.6 |
| 2 | -2.0 -- -1.0 | -1.5 |
| 3 | -1.0 -- 0.0 | -0.5 |
| 4 | 0.0 -- 1.0 | 0.5 |
| 5 | 1.0 -- 2.0 | 1.5 |
| 6 | 2.0 -- 3.2 | 2.6 |

## TABLE 8.

### $\Lambda^0$ polarization as a function of $P_z$

| $\overline{P}_z\,(GeV)$ | $\wp_y \pm \Delta\wp_y$ |
|:---:|:---:|
| -2.6 | +0.142 ± 0.073 |
| -1.5 | +0.142 ± 0.064 |
| -0.5 | +0.010 ± 0.019 |
| 0.5 | -0.074 ± 0.048 |
| 1.5 | -0.172 ± 0.065 |
| 2.6 | -0.230 ± 0.206 |

## TABLE 9.

### $\Lambda^0$ polarization for the 8 track final state sample.
$\Lambda^0$'s and $K^+$'s Z-momentum component, in the center of mass of event, have the same sign.

(a) $P_z \leq 0$

| $\overline{P}_T\,(GeV)$ | $\wp_y \pm \Delta\wp_y$ | $\chi^2/(DOF = 18)$ |
|:---:|:---:|:---:|
| 0.132 | +0.035 ± 0.046 | 1.00 |
| 0.396 | -0.020 ± 0.034 | 1.85 |
| 0.660 | +0.114 ± 0.041 | 1.63 |
| 0.924 | +0.094 ± 0.060 | 1.56 |
| 1.188 | +0.192 ± 0.099 | 0.73 |

(b) $P_z > 0$

| $\overline{P}_T\,(GeV)$ | $\wp_y \pm \Delta\wp_y$ | $\chi^2/(DOF = 18)$ |
|:---:|:---:|:---:|
| 0.132 | -0.052 ± 0.060 | 0.51 |
| 0.396 | +0.052 ± 0.042 | 1.25 |
| 0.66 | -0.095 ± 0.048 | 1.60 |
| 0.924 | -0.183 ± 0.067 | 1.47 |
| 1.188 | -0.110 ± 0.113 | 0.91 |

90

## TABLE 10.

$\Lambda^0$ polarization for the 8 track final state sample.
$\Lambda^0$'s and $K^+$'s Z-momentum component, in the center of mass of event, have opposite sign.

(a) $P_z \leq 0$

| $\overline{P}_T(GeV)$ | $\wp_y \pm \Delta \wp_y$ | $\chi^2/(DOF=18)$ |
|---|---|---|
| 0.132 | +0.031 ± 0.055 | 1.73 |
| 0.396 | +0.102 ± 0.042 | 0.96 |
| 0.660 | +0.146 ± 0.053 | 1.57 |
| 0.924 | +0.097 ± 0.073 | 1.61 |
| 1.188 | +0.185 ± 0.110 | 0.97 |

(b) $P_z > 0$

| $\overline{P}_T(GeV)$ | $\wp_y \pm \Delta \wp_y$ | $\chi^2/(DOF=18)$ |
|---|---|---|
| 0.132 | +0.017 ± 0.071 | 0.80 |
| 0.396 | -0.064 ± 0.049 | 1.37 |
| 0.660 | -0.141 ± 0.056 | 0.73 |
| 0.924 | -0.221 ± 0.082 | 1.54 |
| 1.188 | -0.405 ± 0.130 | 1.09 |

## TABLE 11.

$\Lambda^0$ polarization for the 8 track final state sample.
$\Lambda^0$'s and $p$'s Z-momentum component, in the center of mass of event, have opposite sign.

(a) $P_z \leq 0$

| $\overline{P}_T(GeV)$ | $\wp_y \pm \Delta \wp_y$ | $\chi^2/(DOF=18)$ |
|---|---|---|
| 0.132 | +0.034 ± 0.041 | 2.12 |
| 0.396 | +0.032 ± 0.032 | 2.16 |
| 0.660 | +0.151 ± 0.041 | 1.59 |
| 0.924 | +0.088 ± 0.061 | 1.49 |
| 1.188 | +0.292 ± 0.099 | 0.61 |

(b) $P_z > 0$

| $\overline{P}_T(GeV)$ | $\wp_y \pm \Delta \wp_y$ | $\chi^2/(DOF=18)$ |
|---|---|---|
| 0.132 | -0.008 ± 0.046 | 0.71 |
| 0.396 | +0.008 ± 0.032 | 1.63 |
| 0.660 | -0.120 ± 0.037 | 1.48 |
| 0.924 | -0.200 ± 0.053 | 1.98 |
| 1.188 | -0.280 ± 0.087 | 1.04 |

## TABLE 12.

$\Lambda^0$ polarization for the 8 track final state sample.

$\Lambda^0$'s and $p$'s Z-momentum component in the center of mass of event
have the same sign.

(a) $P_z \leq 0$

| $\overline{P}_T (GeV)$ | $\wp_y \pm \Delta\wp_y$ | $\chi^2/(DOF = 18)$ |
|---|---|---|
| 0.132 | $+0.046 \pm 0.071$ | 1.11 |
| 0.396 | $+0.004 \pm 0.049$ | 1.44 |
| 0.660 | $+0.074 \pm 0.054$ | 1.30 |
| 0.924 | $+0.082 \pm 0.073$ | 1.22 |
| 1.188 | $+0.011 \pm 0.110$ | 1.44 |

(b) $P_z > 0$

| $\overline{P}_T (GeV)$ | $\wp_y \pm \Delta\wp_y$ | $\chi^2/(DOF = 18)$ |
|---|---|---|
| 0.132 | $-0.330 \pm 0.366$ | 1.55 |
| 0.396 | $-0.320 \pm 0.172$ | 0.59 |
| 0.660 | $-0.111 \pm 0.197$ | 1.05 |
| 0.924 | $-0.133 \pm 0.220$ | 0.35 |
| 1.188 | $+0.300 \pm 0.340$ | 1.05 |

## TABLE 13.

Bins for $M(\Lambda K)$.

| Bin | Range $(GeV)$ | $\overline{M}(\Lambda K) (GeV)$ |
|---|---|---|
| 1 | 1.00 -- 1.42 | 1.21 |
| 2 | 1.42 -- 1.84 | 1.63 |
| 3 | 1.84 -- 2.26 | 2.05 |
| 4 | 2.26 -- 2.68 | 2.47 |
| 5 | 2.68 -- 3.10 | 2.89 |

## TABLE 14.

$\Lambda^0$ polarization, for the entire 8 track final state sample,
as a function of $M(\Lambda K)$.

$|P_z| \leq 3.2\ GeV$

| $\overline{M}(\Lambda K)(GeV)$ | $\wp, \pm \Delta \wp,$ | $\chi^2/(DOF = 18)$ |
|---|---|---|
| 1.21 | * | * |
| 1.63 | -0.013 ± 0.023 | 2.59 |
| 2.05 | 0.024 ± 0.020 | 3.19 |
| 2.47 | -0.019 ± 0.029 | 1.04 |
| 2.89 | * | * |

\* not enough statistics.

## TABLE 15.

$\Lambda^0$ polarization, for the 8 track final state sample,
as a function of $M(\Lambda K)$.

(a) $P_z \leq 0$

| $\overline{M}(\Lambda K)(GeV)$ | $\wp, \pm \Delta \wp,$ | $\chi^2/(DOF = 18)$ |
|---|---|---|
| 1.21 | * | * |
| 1.63 | -0.020 ± 0.030 | 1.99 |
| 2.05 | +0.116 ± 0.028 | 2.87 |
| 2.47 | +0.108 ± 0.040 | 1.36 |
| 2.89 | * | * |

(b) $P_z > 0$

| $\overline{M}(\Lambda K)(GeV)$ | $\wp, \pm \Delta \wp,$ | $\chi^2/(DOF = 18)$ |
|---|---|---|
| 1.21 | * | * |
| 1.63 | -0.004 ± 0.038 | 1.46 |
| 2.05 | -0.080 ± 0.030 | 1.55 |
| 2.47 | -0.160 ± 0.043 | 1.18 |
| 2.89 | * | * |

\* not enough statistics.

**TABLE 16.**

Bins for $M(\Lambda K \pi^+ \pi^-)$.

| Bin | Range $(GeV)$ | $\overline{M}(\Lambda K \pi^+ \pi^-)(GeV)$ |
|-----|---------------|--------------------------------------------|
| 1   | 2.0 -- 2.5    | 2.25                                       |
| 2   | 2.5 -- 3.0    | 2.75                                       |
| 3   | 3.0 -- 3.5    | 3.25                                       |
| 4   | 3.5 -- 4.0    | 3.75                                       |
| 5   | 4.0 -- 4.5    | 4.25                                       |

**TABLE 17.**

$\Lambda^0$ polarization, for the entire 8 track final state sample,
as a function of $M(\Lambda K \pi^+ \pi^-)$.

$|P_z| \leq 3.2\ GeV$

| $\overline{M}(\Lambda K \pi^+ \pi^-)(GeV)$ | $\wp_y \pm \Delta \wp_y$ | $\chi^2/(DOF = 18)$ |
|--------------------------------------------|--------------------------|----------------------|
| 2.25 | * | * |
| 2.75 | +0.012 ± 0.033 | 1.70 |
| 3.25 | -0.020 ± 0.026 | 2.49 |
| 3.75 | -0.023 ± 0.026 | 1.97 |
| 4.25 | * | * |

* not enough statistics.

## TABLE 18.

$\Lambda^0$ polarization, for the 8 track final state sample,
as a function of $M(\Lambda K\pi^+\pi^-)$.

(a) $P_z \leq 0$

| $\overline{M}(\Lambda K\pi^+\pi^-)(GeV)$ | $\wp, \pm\Delta\wp,$ | $\chi^2/(DOF=18)$ |
|---|---|---|
| 2.25 | * | * |
| 2.75 | $0.008 \pm 0.059$ | 1.33 |
| 3.25 | $0.027 \pm 0.040$ | 2.78 |
| 3.75 | $0.060 \pm 0.030$ | 1.51 |
| 4.25 | * | * |

(b) $P_z > 0$

| $\overline{M}(\Lambda K\pi^+\pi^-)(GeV)$ | $\wp, \pm\Delta\wp,$ | $\chi^2/(DOF=18)$ |
|---|---|---|
| 2.25 | * | * |
| 2.75 | $+0.014 \pm 0.040$ | 1.38 |
| 3.25 | $-0.057 \pm 0.034$ | 1.00 |
| 3.75 | $-0.152 \pm 0.041$ | 1.33 |
| 4.25 | * | * |

* not enough statistics.

## TABLE 19.

Bins for $M(\Lambda K 2(\pi^+\pi^-))$.

| Bin | Range (GeV) | $\overline{M}(\Lambda K 2(\pi^+\pi^-))(GeV)$ |
|---|---|---|
| 1 | 3.0 -- 3.6 | 3.3 |
| 2 | 3.6 -- 4.2 | 3.9 |
| 3 | 4.2 -- 4.8 | 4.5 |
| 4 | 4.8 -- 5.4 | 5.1 |
| 5 | 5.4 -- 6.0 | 5.7 |

## TABLE 20.

$\Lambda^0$ polarization, for the entire 8 track final state sample, as a function of $M(\Lambda K2(\pi^+\pi^-))$.

$|P_z| \le 3.2\ GeV$

| $\overline{M}(\Lambda K2(\pi^+\pi^-))\ GeV$ | $\wp_y \pm \Delta\wp_y$ | $\chi^2/(DOF = 18)$ |
|---|---|---|
| 3.3 | * | * |
| 3.9 | $0.049 \pm 0.034$ | 2.26 |
| 4.5 | $-0.020 \pm 0.025$ | 1.61 |
| 5.1 | $-0.026 \pm 0.025$ | 1.79 |
| 5.7 | * | * |

\* not enough statistics

## TABLE 21.

$\Lambda^0$ polarization, for the 8 track final state sample, as a function of $M(\Lambda K2(\pi^+\pi^-))$.

(a) $P_z \le 0$

| $\overline{M}(\Lambda K2(\pi^+\pi^-))\ GeV$ | $\wp_y \pm \Delta\wp_y$ | $\chi^2/(DOF = 18)$ |
|---|---|---|
| 3.3 | * | * |
| 3.9 | $0.068 \pm 0.040$ | 2.11 |
| 4.5 | $0.064 \pm 0.032$ | 1.50 |
| 5.1 | $0.061 \pm 0.030$ | 1.29 |
| 5.7 | * | |

(b) $P_z > 0$

| $\overline{M}(\Lambda K2(\pi^+\pi^-))\ GeV$ | $\wp_y \pm \Delta\wp_y$ | $\chi^2/(DOF = 18)$ |
|---|---|---|
| 3.3 | * | * |
| 3.9 | $+0.047 \pm 0.042$ | 1.65 |
| 4.5 | $-0.079 \pm 0.033$ | 1.25 |
| 5.1 | $-0.140 \pm 0.039$ | 1.71 |
| 5.7 | * | * |

\* not enough statistics

96

## TABLE 22.
$\Lambda^0$ polarization, for the 8 track final state sample,
without $\Lambda^0$ from $\Sigma^0 \rightarrow \Lambda^0 \gamma$.

(a) $P_z \leq 0$

| $\overline{P}_T (GeV)$ | $\wp_y \pm \Delta \wp_y$ | $\chi^2/(DOF = 18)$ |
|---|---|---|
| 0.132 | $0.053 \pm 0.044$ | 1.34 |
| 0.396 | $0.012 \pm 0.033$ | 1.40 |
| 0.660 | $0.123 \pm 0.041$ | 1.49 |
| 0.924 | $0.109 \pm 0.061$ | 1.57 |
| 1.188 | $0.273 \pm 0.094$ | 0.64 |

(b) $P_z > 0$

| $\overline{P}_T (GeV)$ | $\wp_y \pm \Delta \wp_y$ | $\chi^2/(DOF = 18)$ |
|---|---|---|
| 0.132 | $+0.074 \pm 0.057$ | 0.75 |
| 0.396 | $+0.036 \pm 0.039$ | 1.90 |
| 0.660 | $-0.106 \pm 0.046$ | 1.48 |
| 0.924 | $-0.174 \pm 0.066$ | 1.93 |
| 1.188 | $-0.300 \pm 0.108$ | 1.28 |

97

**TABLE 23.**

$\Lambda^0$ polarization, for the 8 track final state sample,

without $\Lambda^0$ from $\Sigma^{*-} \to \Lambda^0 \pi^-$.

(a) $P_z \leq 0$

| $\overline{P}_T (GeV)$ | $\wp_y \pm \Delta \wp_y$ | $\chi^2/(DOF = 18)$ |
|---|---|---|
| 0.132 | $0.037 \pm 0.036$ | 1.32 |
| 0.396 | $0.024 \pm 0.027$ | 1.85 |
| 0.660 | $0.120 \pm 0.033$ | 2.40 |
| 0.924 | $0.100 \pm 0.047$ | 1.91 |
| 1.188 | $0.190 \pm 0.074$ | 1.20 |

(b) $P_z > 0$

| $\overline{P}_T (GeV)$ | $\wp_y \pm \Delta \wp_y$ | $\chi^2/(DOF = 18)$ |
|---|---|---|
| 0.132 | $-0.011 \pm 0.046$ | 0.58 |
| 0.396 | $+0.001 \pm 0.032$ | 1.71 |
| 0.660 | $-0.120 \pm 0.037$ | 1.42 |
| 0.924 | $-0.200 \pm 0.053$ | 1.79 |
| 1.188 | $-0.270 \pm 0.087$ | 1.09 |

98

**TABLE 24.**

$\Lambda^0$ polarization, for the 8 track final state,

without $\Lambda^0$ from $\Sigma^{*+} \to \Lambda^0 \pi^+$.

(a)  $P_z \leq 0$

| $\overline{P}_T(GeV)$ | $\wp_y \pm \Delta\wp_y$ | $\chi^2/(DOF = 18)$ |
|---|---|---|
| 0.132 | $0.037 \pm 0.036$ | 1.32 |
| 0.396 | $0.024 \pm 0.027$ | 1.85 |
| 0.660 | $0.120 \pm 0.033$ | 2.40 |
| 0.924 | $0.100 \pm 0.047$ | 1.91 |
| 1.188 | $0.190 \pm 0.074$ | 1.20 |

(b)  $P_z > 0$

| $\overline{P}_T(GeV)$ | $\wp_y \pm \Delta\wp_y$ | $\chi^2/(DOF = 18)$ |
|---|---|---|
| 0.132 | $-0.011 \pm 0.046$ | 0.58 |
| 0.396 | $+0.001 \pm 0.032$ | 1.71 |
| 0.660 | $-0.120 \pm 0.037$ | 1.42 |
| 0.924 | $-0.200 \pm 0.053$ | 1.79 |
| 1.188 | $-0.270 \pm 0.087$ | 1.09 |

<div align="center">

**TABLE 25.**

$\Lambda^0$ polarization for the 6 track final state sample.

</div>

(a) $P_z \leq 0$

| $\overline{P}_T (GeV)$ | $\wp_y \pm \Delta \wp_y$ | $\chi^2/(DOF = 18)$ |
|---|---|---|
| 0.132 | $-0.000 \pm 0.106$ | 1.84 |
| 0.396 | $+0.140 \pm 0.097$ | 1.75 |
| 0.660 | $+0.055 \pm 0.130$ | 0.94 |
| 0.924 | $+0.278 \pm 0.200$ | 1.42 |
| 1.188 | $+0.260 \pm 0.327$ | 1.14 |

(b) $P_z > 0$

| $\overline{P}_T (GeV)$ | $\wp_y \pm \Delta \wp_y$ | $\chi^2/(DOF = 18)$ |
|---|---|---|
| 0.132 | $-0.052 \pm 0.170$ | 0.86 |
| 0.396 | $+0.140 \pm 0.120$ | 1.61 |
| 0.660 | $-0.110 \pm 0.120$ | 0.97 |
| 0.924 | $-0.376 \pm 0.173$ | 1.33 |
| 1.188 | $-0.041 \pm 0.360$ | 1.13 |

<div align="center">

100

</div>

**TABLE 26.**

$\Lambda^0$ polarization for the 10 track final state sample.

(a) $P_z \leq 0$

| $\overline{P}_T(GeV)$ | $\wp_y \pm \Delta\wp_y$ | $\chi^2/(DOF = 18)$ |
|---|---|---|
| 0.132 | $0.079 \pm 0.039$ | 1.45 |
| 0.396 | $0.025 \pm 0.028$ | 2.81 |
| 0.660 | $0.070 \pm 0.032$ | 3.80 |
| 0.924 | $0.024 \pm 0.045$ | 1.71 |
| 1.188 | $0.023 \pm 0.076$ | 0.88 |

(b) $P_z > 0$

| $\overline{P}_T(GeV)$ | $\wp_y \pm \Delta\wp_y$ | $\chi^2/(DOF = 18)$ |
|---|---|---|
| 0.132 | $-0.073 \pm 0.048$ | 2.77 |
| 0.396 | $-0.116 \pm 0.033$ | 1.14 |
| 0.660 | $-0.100 \pm 0.038$ | 1.91 |
| 0.924 | $-0.104 \pm 0.056$ | 1.14 |
| 1.188 | $-0.189 \pm 0.093$ | 1.30 |

## TABLE 27.

$\Lambda^0$ polarization for the 12 track final state sample.

(a) $P_z \leq 0$

| $\overline{P}_T(GeV)$ | $\wp_y \pm \Delta \wp_y$ | $\chi^2/(DOF = 18)$ |
|---|---|---|
| 0.132 | $0.049 \pm 0.070$ | 1.01 |
| 0.396 | $0.006 \pm 0.048$ | 0.84 |
| 0.660 | $0.085 \pm 0.057$ | 1.47 |
| 0.924 | $-0.015 \pm 0.083$ | 0.98 |
| 1.188 | $0.063 \pm 0.153$ | 1.52 |

(b) $P_z > 0$

| $\overline{P}_T(GeV)$ | $\wp_y \pm \Delta \wp_y$ | $\chi^2/(DOF = 18)$ |
|---|---|---|
| 0.132 | $-0.131 \pm 0.084$ | 1.25 |
| 0.396 | $0.028 \pm 0.060$ | 1.58 |
| 0.66 | $-0.043 \pm 0.070$ | 0.73 |
| 0.924 | $-0.136 \pm 0.105$ | 0.81 |
| 1.188 | $-0.119 \pm 0.183$ | 0.92 |

## TABLE 28.

$\Lambda^0$ polarization, for the 6 track final state sample, combining both hemispheres data.

$P_z > 0$

| $\overline{P}_T(GeV)$ | $\wp_y \pm \Delta \wp_y$ | $\chi^2/(DOF = 18)$ |
|---|---|---|
| 0.132 | $0.002 \pm 0.089$ | 1.38 |
| 0.396 | $0.022 \pm 0.073$ | 1.21 |
| 0.66 | $0.074 \pm 0.090$ | 1.02 |
| 0.924 | $0.260 \pm 0.129$ | 1.59 |
| 1.188 | $0.200 \pm 0.230$ | 1.56 |

102

# TABLE 29.

$K^0_s$ polarization for the 8 track final state sample.

(a) $P_z \leq 0$

| $\overline{P}_T (GeV)$ | $\wp_y \pm \Delta \wp_y$ | $\chi^2/(DOF = 18)$ |
|---|---|---|
| 0.132 | -0.033 ± 0.062 | 3.67 |
| 0.396 | -0.047 ± 0.049 | 7.11 |
| 0.66 | 0.008 ± 0.060 | 2.81 |
| 0.924 | 0.035 ± 0.088 | 1.53 |
| 1.188 | -0.002 ± 0.150 | 1.37 |

(b) $P_z > 0$

| $\overline{P}_T (GeV)$ | $\wp_y \pm \Delta \wp_y$ | $\chi^2/(DOF = 18)$ |
|---|---|---|
| 0.132 | +0.052 ± 0.047 | 1.74 |
| 0.396 | -0.029 ± 0.037 | 1.88 |
| 0.66 | 0.036 ± 0.048 | 1.28 |
| 0.924 | -0.027 ± 0.079 | 1.45 |
| 1.188 | -0.068 ± 0.159 | 0.49 |

# TABLE 30.

$\Lambda^0$ polarization, for the Monte Carlo 8 track final state sample.

(a) $P_z \leq 0$

| $\overline{P}_T (GeV)$ | $\wp_y \pm \Delta \wp_y$ | $\chi^2/(DOF = 18)$ |
|---|---|---|
| 0.132 | -0.044 ± 0.085 | 1.00 |
| 0.396 | 0.049 ± 0.055 | 0.85 |
| 0.660 | -0.200 ± 0.056 | 1.93 |
| 0.924 | -0.090 ± 0.064 | 1.09 |
| 1.188 | -0.348 ± 0.092 | 1.06 |

(b) $P_z > 0$

| $\overline{P}_T (GeV)$ | $\wp_y \pm \Delta \wp_y$ | $\chi^2/(DOF = 18)$ |
|---|---|---|
| 0.132 | 0.002 ± 0.042 | 1.03 |
| 0.396 | 0.031 ± 0.028 | 1.69 |
| 0.660 | -0.186 ± 0.028 | 1.43 |
| 0.924 | -0.204 ± 0.035 | 0.84 |
| 1.188 | -0.313 ± 0.051 | 1.59 |

**TABLE 31.**

Number of Monte Carlo $\Lambda^0$ sample events generated and accepted, in the big statistics sample.

| Final state multiplicity particles | Number of events generated | Number of events after PASS3 |
|---|---|---|
| 6 | 500 000 | 35 055 |
| 8 | 1000 000 | 133 858 |
| 10 | 600 000 | 89 353 |
| 12 | 200 000 | 39 203 |

**TABLE 32.**

Average acceptance in the big statistics sample.

| Final state multiplicity particles | Average acceptance (%) |
|---|---|
| 6 | 5.33 |
| 8 | 11.17 |
| 10 | 13.04 |
| 12 | 16.75 |

**TABLE 33.**

Average time required to generate the Monte Carlo samples.

| Final state multiplicity particles | Number of events generated | Average time (days) |
|---|---|---|
| 6 | 500 000 | 22 |
| 8 | 1000 000 | 45 |
| 10 | 600 000 | 42 |
| 12 | 200 000 | 94 |

**TABLE 34.**

Number of Monte Carlo $K_s^0$ generated and accepted.

| Number of final state multiplicity particles | Number of events generated | Number of events after PASS3 |
|:---:|:---:|:---:|
| 8 | 150000 | 79800 |

**TABLE 35.**

Monte Carlo $\Lambda^0$ polarization distribution.

| Range of $P_T (GeV)$ | Polarization |
|:---:|:---:|
| 0.000, -- 0.264 | -0.015 |
| 0.264, -- 0.528 | 0.025 |
| 0.528, -- 0.792 | -0.123 |
| 0.792, -- 1.056 | -0.176 |
| 1.056, -- 1.32 | -0.370 |
| 1.32, -- $\infty$ | -0.400 |

## TABLE 36.
Number of Monte Carlo $\Lambda^0$ sample events generated and accepted, in the SS sample.

| Final state multiplicity particles | Model | Number of events generated | Number of events after PASS4 |
|---|---|---|---|
| 6 | 1 | 100 000 | 2 635 |
|   | 2 | 28 000 | 474 |
| 8 | 1 | 50 000 | 4 515 |
|   | 2 | 29 000 | 3 084 |
| 10 | 1 | 31 000 | 4 479 |
|    | 2 | 50 000 | 6 611 |
| 12 | 1 | Not generated | --- |
|    | 2 | Not generated | --- |

## TABLE 37.
Average acceptance in the SS sample.

| Final state multiplicity particles | Average acceptance (%) |
|---|---|
| 6 | 2.4 |
| 8 | 9.6 |
| 10 | 13.04 |
| 12 | * |

* Not calculated

**TABLE 38.**

Straight line fits of the BS sample and of the SS sample,
for the 6 track final state sample.

(a) $P_z \leq 0$

| $\bar{P}_T(GeV)$ | | slope, $\pm \Delta(slope)$, <br> * BS <br> ** SS | $\chi^2/(DOF = 18)$ |
|---|---|---|---|
| | * | $0.002 \pm 0.002$ | 10.16 |
| 0.132 | ** | $0.000 \pm 0.006$ | 0.85 |
| | * | $0.000 \pm 0.001$ | 6.06 |
| 0.396 | ** | $0.003 \pm 0.005$ | 1.72 |
| | * | $0.004 \pm 0.002$ | 2.00 |
| 0.660 | ** | $-0.003 \pm 0.007$ | 1.61 |
| | * | $0.003 \pm 0.004$ | 1.43 |
| 0.924 | ** | $0.004 \pm 0.010$ | 1.26 |
| | * | $-0.002 \pm 0.008$ | 1.56 |
| 1.188 | ** | $0.028 \pm 0.096$ | 1.08 |

(b) $P_z > 0$

| $\bar{P}_T(GeV)$ | | slope, $\pm \Delta(slope)$, <br> * BS <br> ** SS | $\chi^2/(DOF = 18)$ |
|---|---|---|---|
| | * | $0.002 \pm 0.002$ | 1.16 |
| 0.132 | ** | $-0.002 \pm 0.006$ | 1.31 |
| | * | $0.000 \pm 0.001$ | 1.35 |
| 0.396 | ** | $-0.001 \pm 0.004$ | 0.41 |
| | * | $0.001 \pm 0.002$ | 1.05 |
| 0.660 | ** | $0.006 \pm 0.006$ | 1.43 |
| | * | $0.003 \pm 0.004$ | 1.10 |
| 0.924 | ** | $0.008 \pm 0.009$ | 1.03 |
| | * | $0.010 \pm 0.008$ | 0.66 |
| 1.188 | ** | $0.019 \pm 0.016$ | 0.82 |

107

## TABLE 39.
Straight line fits of the BS sample and of the SS sample,
for the 8 track final state sample.

(a) $P_z \leq 0$

| $\overline{P}_T(GeV)$ | | slope, $\pm \Delta(slope)$, <br> * BS <br> ** SS | $\chi^2/(DOF = 18)$ |
|---|---|---|---|
| | * | $0.000 \pm 0.001$ | 1.98 |
| 0.132 | ** | $-0.004 \pm 0.005$ | 0.68 |
| | * | $0.000 \pm 0.001$ | 3.14 |
| 0.396 | ** | $0.002 \pm 0.004$ | 1.37 |
| | * | $-0.001 \pm 0.002$ | 3.18 |
| 0.660 | ** | $0.003 \pm 0.006$ | 1.18 |
| | * | $0.000 \pm 0.003$ | 1.94 |
| 0.924 | ** | $0.016 \pm 0.010$ | 0.62 |
| | * | $-0.006 \pm 0.006$ | 1.13 |
| 1.188 | ** | $0.005 \pm 0.019$ | 1.04 |

(b) $P_z > 0$

| $\overline{P}_T(GeV)$ | | slope, $\pm \Delta(slope)$, <br> * BS <br> ** SS | $\chi^2/(DOF = 18)$ |
|---|---|---|---|
| | * | $0.000 \pm 0.001$ | 1.80 |
| 0.132 | ** | $-0.002 \pm 0.004$ | 2.10 |
| | * | $-0.001 \pm 0.001$ | 1.46 |
| 0.396 | ** | $-0.003 \pm 0.004$ | 1.30 |
| | * | $0.000 \pm 0.002$ | 1.64 |
| 0.660 | ** | $-0.007 \pm 0.006$ | 1.38 |
| | * | $-0.003 \pm 0.003$ | 0.65 |
| 0.924 | ** | $0.000 \pm 0.010$ | 1.13 |
| | * | $0.010 \pm 0.006$ | 1.01 |
| 1.188 | ** | $-0.003 \pm 0.018$ | 0.94 |

**TABLE 40.**
Straight line fits of the BS sample and of the SS sample,
for the 10 track final state sample.

(a) $P_z \leq 0$

| $\overline{P}_T (GeV)$ | slope, $\pm \Delta(slope)$, * BS ** SS | | $\chi^2/(DOF = 18)$ |
|---|---|---|---|
| 0.132 | * | $-0.001 \pm 0.001$ | 1.43 |
| | ** | $0.000 \pm 0.006$ | 0.85 |
| 0.396 | * | $0.002 \pm 0.001$ | 1.77 |
| | ** | $0.003 \pm 0.005$ | 1.72 |
| 0.660 | * | $0.002 \pm 0.002$ | 0.77 |
| | ** | $-0.003 \pm 0.007$ | 1.61 |
| 0.924 | * | $-0.003 \pm 0.003$ | 0.80 |
| | ** | $0.004 \pm 0.010$ | 1.26 |
| 1.188 | * | $-0.005 \pm 0.006$ | 0.93 |
| | ** | $0.028 \pm 0.096$ | 1.08 |

(b) $P_z > 0$

| $\overline{P}_T (GeV)$ | slope, $\pm \Delta(slope)$, * BS ** SS | | $\chi^2/(DOF = 18)$ |
|---|---|---|---|
| 0.132 | * | $0.000 \pm 0.002$ | 1.91 |
| | ** | $-0.002 \pm 0.006$ | 1.31 |
| 0.396 | * | $0.002 \pm 0.002$ | 2.43 |
| | ** | $-0.001 \pm 0.004$ | 0.41 |
| 0.660 | * | $0.002 \pm 0.003$ | 3.60 |
| | ** | $0.006 \pm 0.006$ | 1.43 |
| 0.924 | * | $0.005 \pm 0.005$ | 1.31 |
| | ** | $0.008 \pm 0.009$ | 1.03 |
| 1.188 | * | $0.010 \pm 0.009$ | 0.70 |
| | * | $0.019 \pm 0.016$ | 0.82 |

# TABLE 41.

Straight line fits of the BS sample, for the 12 track final state sample.

(a) $P_z \leq 0$

| $\overline{P}_r(GeV)$ | slope, $\pm \Delta(slope)$, * BS | $\chi^2/(DOF = 18)$ |
|---|---|---|
| 0.132 | * $0.001 \pm 0.005$ | 1.25 |
| 0.396 | * $0.002 \pm 0.004$ | 2.70 |
| 0.660 | * $0.010 \pm 0.005$ | 2.97 |
| 0.924 | * $0.002 \pm 0.008$ | 1.92 |
| 1.188 | * $0.007 \pm 0.020$ | 1.39 |

(b) $P_z > 0$

| $\overline{P}_r(GeV)$ | slope, $\pm \Delta(slope)$, * BS | $\chi^2/(DOF = 18)$ |
|---|---|---|
| 0.132 | * $0.002 \pm 0.004$ | 1.43 |
| 0.396 | * $0.000 \pm 0.003$ | 1.16 |
| 0.660 | * $-0.007 \pm 0.004$ | 1.02 |
| 0.924 | * $0.004 \pm 0.007$ | 1.83 |
| 1.188 | * $0.020 \pm 0.010$ | 0.80 |

## TABLE 42.
$\Lambda^0$ polarization for the 8 track final state sample.

(a) $P_z \leq 0$

| $\overline{P}_T (GeV)$ | | $\wp_y \pm \Delta \wp_y$ <br> * Not corrected <br> ** Corrected | $\chi^2/(DOF = 18)$ |
|---|---|---|---|
| | * | $0.028 \pm 0.035$ | 1.34 |
| 0.132 | ** | $0.014 \pm 0.044$ | 1.09 |
| | * | $0.025 \pm 0.027$ | 2.02 |
| 0.396 | ** | $0.010 \pm 0.032$ | 1.14 |
| | * | $0.128 \pm 0.032$ | 2.42 |
| 0.660 | ** | $0.141 \pm 0.038$ | 1.19 |
| | * | $0.097 \pm 0.046$ | 1.93 |
| 0.924 | ** | $0.114 \pm 0.053$ | 0.70 |
| | * | $0.183 \pm 0.072$ | 1.18 |
| 1.188 | ** | $0.231 \pm 0.085$ | 0.74 |

(b) $P_z > 0$

| $\overline{P}_T (GeV)$ | | $\wp_y \pm \Delta \wp_y$ <br> * Not corrected <br> ** Corrected | $\chi^2/(DOF = 18)$ |
|---|---|---|---|
| | * | $-0.020 \pm 0.046$ | 0.70 |
| 0.132 | ** | $-0.027 \pm 0.051$ | 0.98 |
| | * | $0.003 \pm 0.032$ | 1.69 |
| 0.396 | ** | $0.020 \pm 0.036$ | 0.83 |
| | * | $-0.114 \pm 0.037$ | 1.47 |
| 0.660 | ** | $-0.124 \pm 0.041$ | 0.76 |
| | * | $-0.196 \pm 0.052$ | 1.89 |
| 0.924 | ** | $-0.168 \pm 0.058$ | 1.28 |
| | * | $-0.234 \pm 0.084$ | 1.09 |
| 1.188 | ** | $-0.334 \pm 0.095$ | 1.52 |

**TABLE 43.**

Monte Carlo $\Lambda^0$ polarization for the 8 track final state sample.

(a) $P_z \leq 0$

| $\overline{P}_T(GeV)$ | | $\wp_y \pm \Delta \wp_y$ <br> * Not corrected <br> ** Corrected | $\chi^2/(DOF = 18)$ |
|---|---|---|---|
| | * | $-0.044 \pm 0.085$ | 1.00 |
| 0.132 | ** | $-0.064 \pm 0.090$ | 1.29 |
| | * | $0.049 \pm 0.055$ | 0.85 |
| 0.396 | ** | $0.031 \pm 0.057$ | 0.85 |
| | * | $-0.200 \pm 0.056$ | 1.93 |
| 0.660 | ** | $-0.187 \pm 0.058$ | 1.57 |
| | * | $-0.090 \pm 0.064$ | 1.09 |
| 0.924 | ** | $-0.086 \pm 0.068$ | 1.37 |
| | * | $-0.348 \pm 0.092$ | 0.83 |
| 1.188 | ** | $-0.289 \pm 0.101$ | 1.83 |

(b) $P_z > 0$

| $\overline{P}_T(GeV)$ | | $\wp_y \pm \Delta \wp_y$ <br> * Not corrected <br> ** Corrected | $\chi^2/(DOF = 18)$ |
|---|---|---|---|
| | * | $-0.002 \pm 0.042$ | 1.03 |
| 0.132 | ** | $0.007 \pm 0.048$ | 1.29 |
| | * | $0.030 \pm 0.028$ | 1.69 |
| 0.396 | ** | $0.046 \pm 0.032$ | 0.84 |
| | * | $-0.186 \pm 0.028$ | 1.43 |
| 0.660 | ** | $-0.195 \pm 0.034$ | 1.13 |
| | * | $-0.204 \pm 0.035$ | 0.84 |
| 0.924 | ** | $-0.176 \pm 0.044$ | 0.72 |
| | * | $-0.313 \pm 0.051$ | 1.59 |
| 1.188 | ** | $-0.407 \pm 0.068$ | 1.17 |

# FIGURES

**FIGURE 1.** Three different creation processes. a) SSD, b) DDD, and c) DPE.
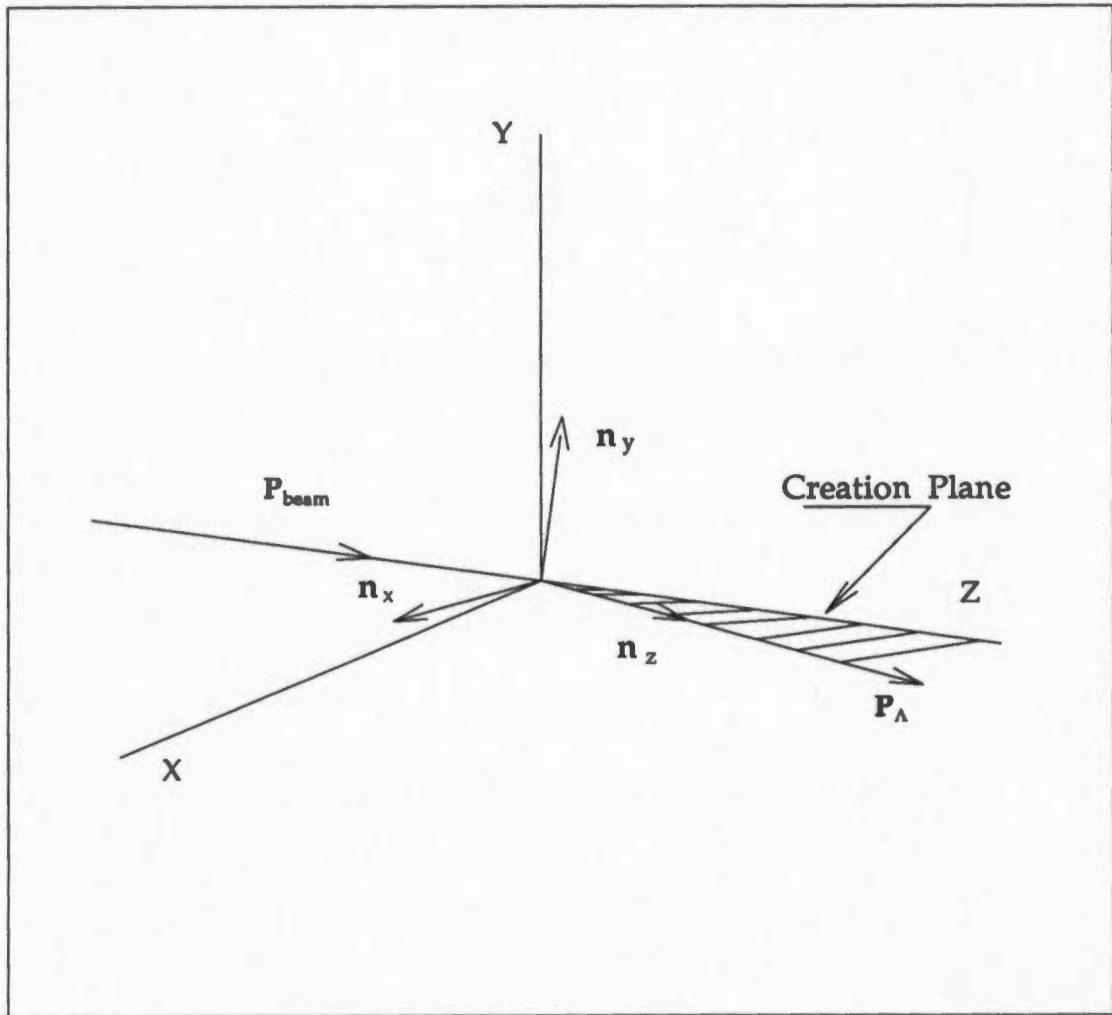
**FIGURE 2.** Relation between the laboratory coordinate system (XYZ) and the creation plane. $n_x$, $n_y$, and $n_z$ represent the coordinate system where $\Lambda^0$ polarization was measured.

115
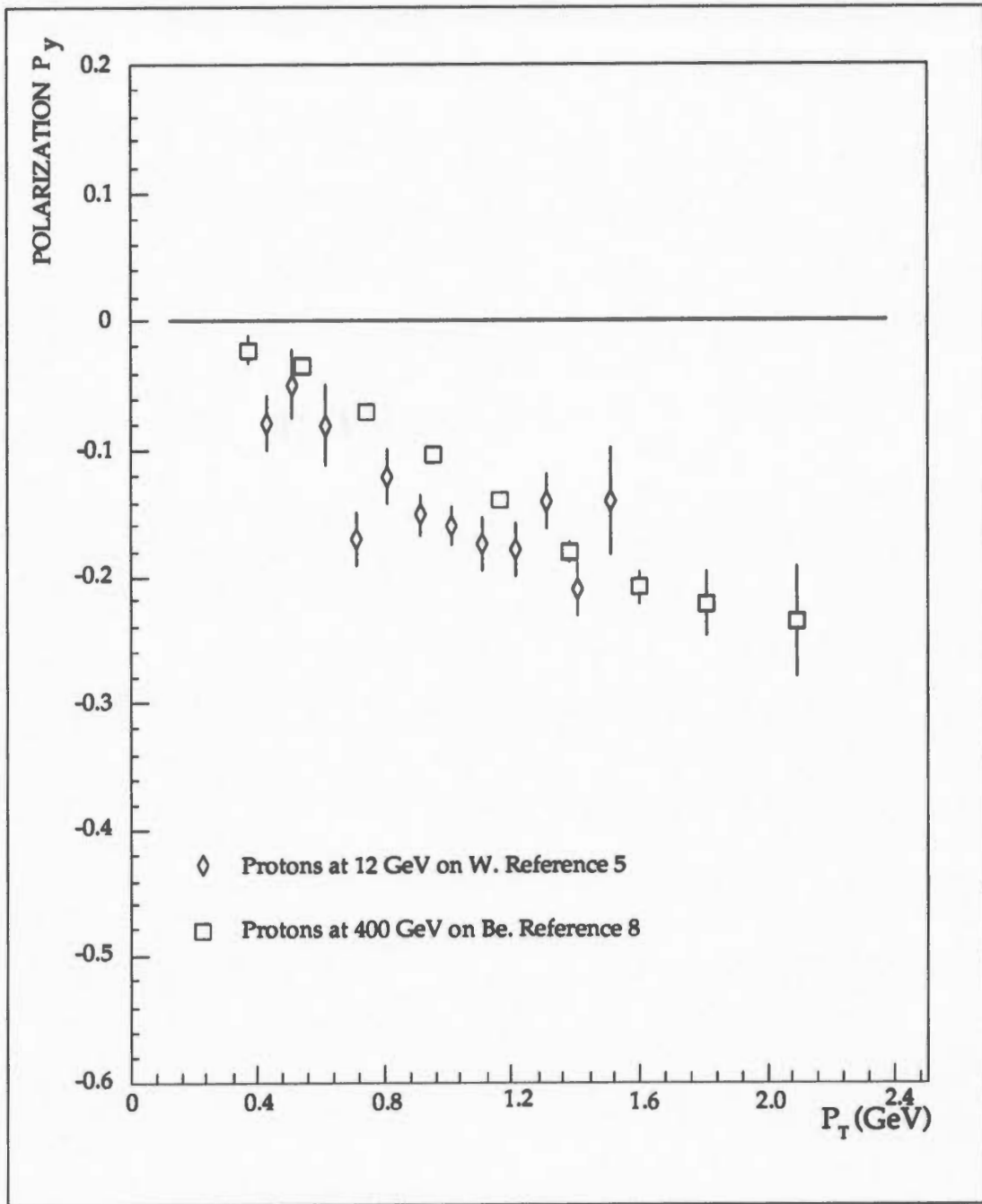
**FIGURE 3.** Experimental $\Lambda^0$ polarization results in inclusive reactions.

116
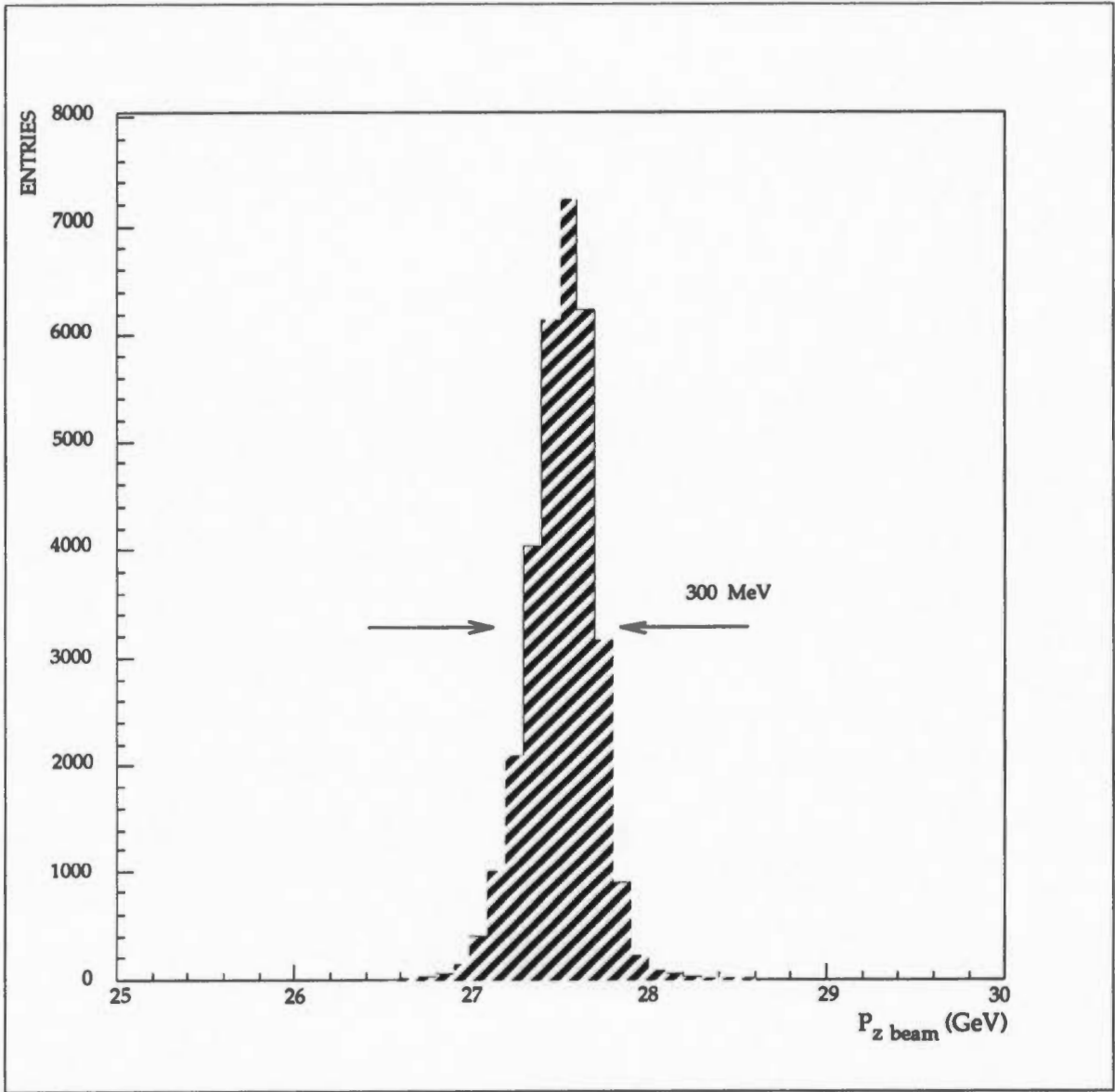
**FIGURE 4.**     Beam proton spectrum determined with the beam proton spectrometer.
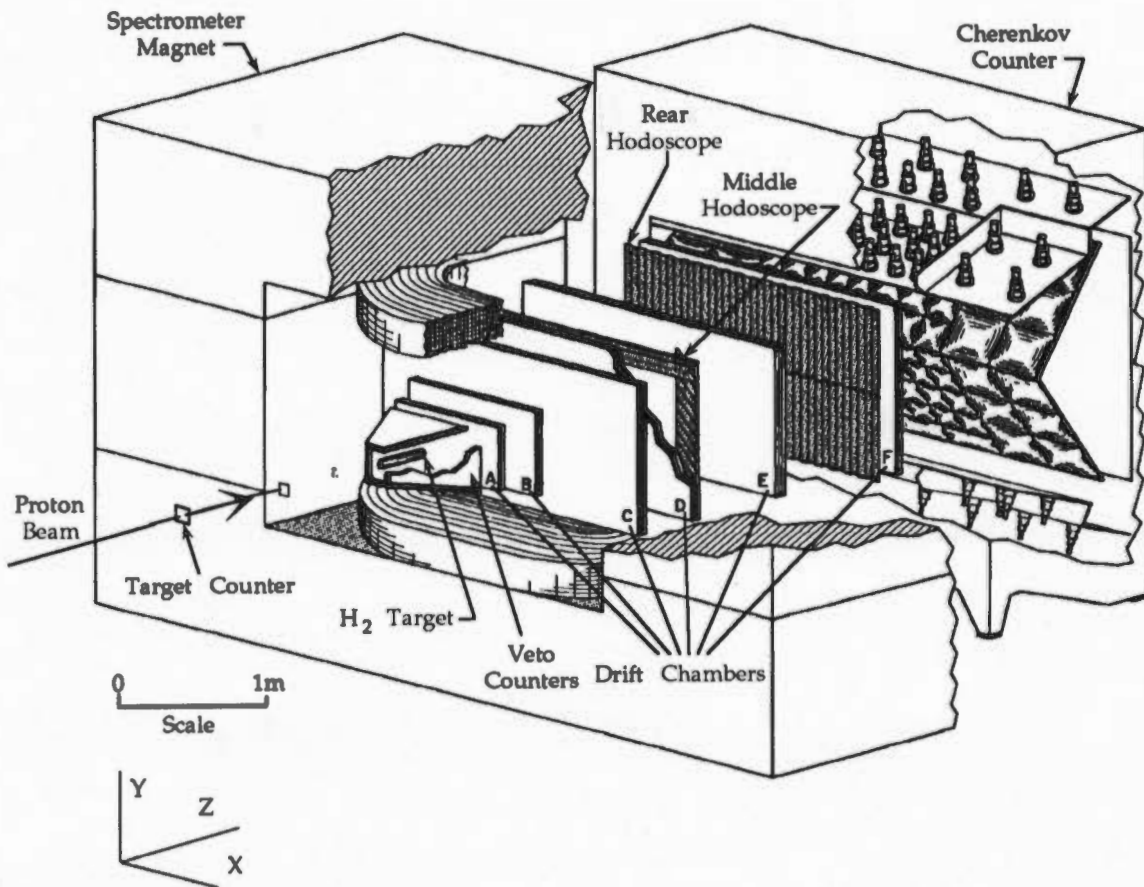
**FIGURE 5.**  The BNL E766 Multiparticle Spectrometer.

118
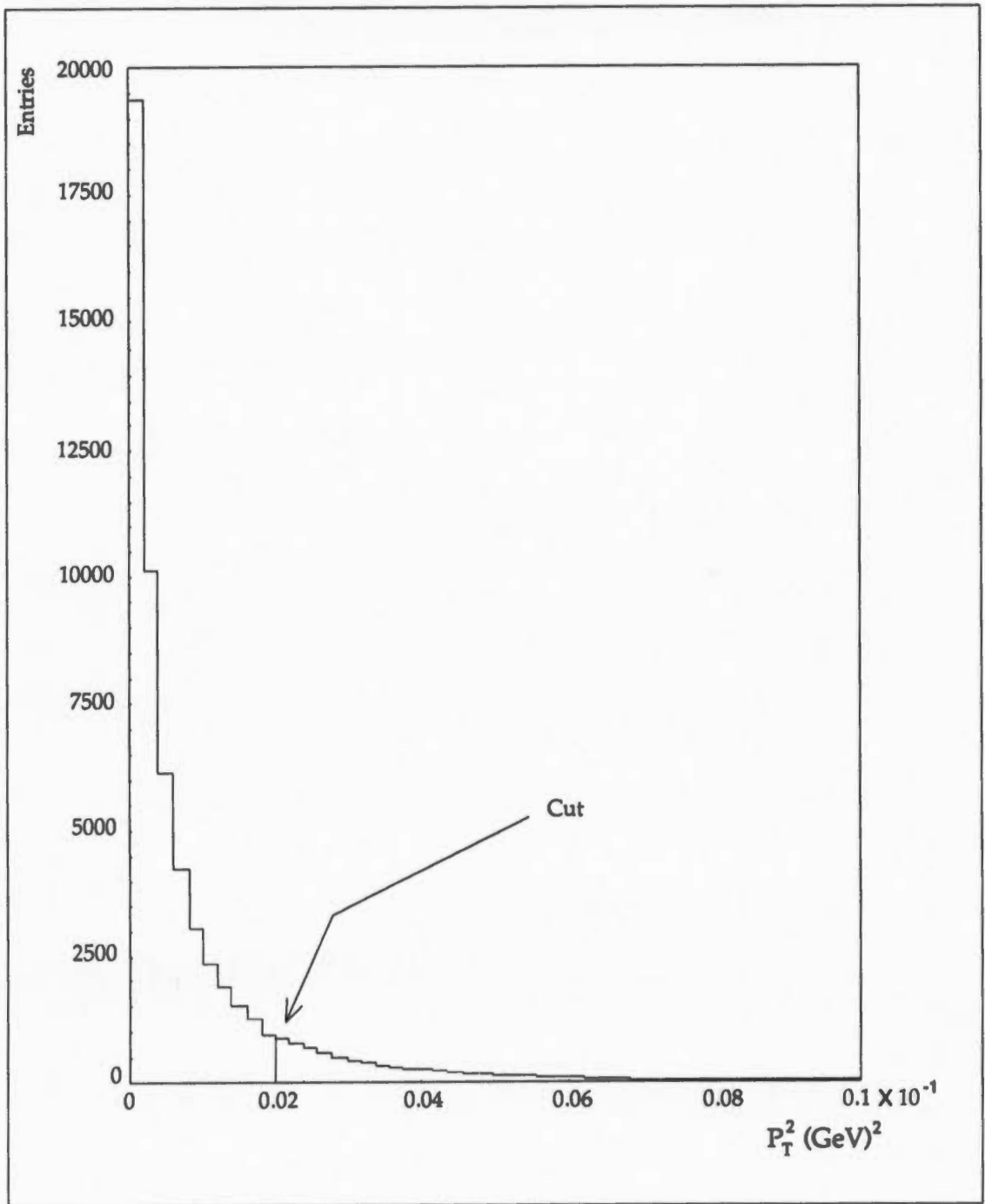
**FIGURE 6.** $P_T^2$ distribution, for the 8 track final state sample.

119
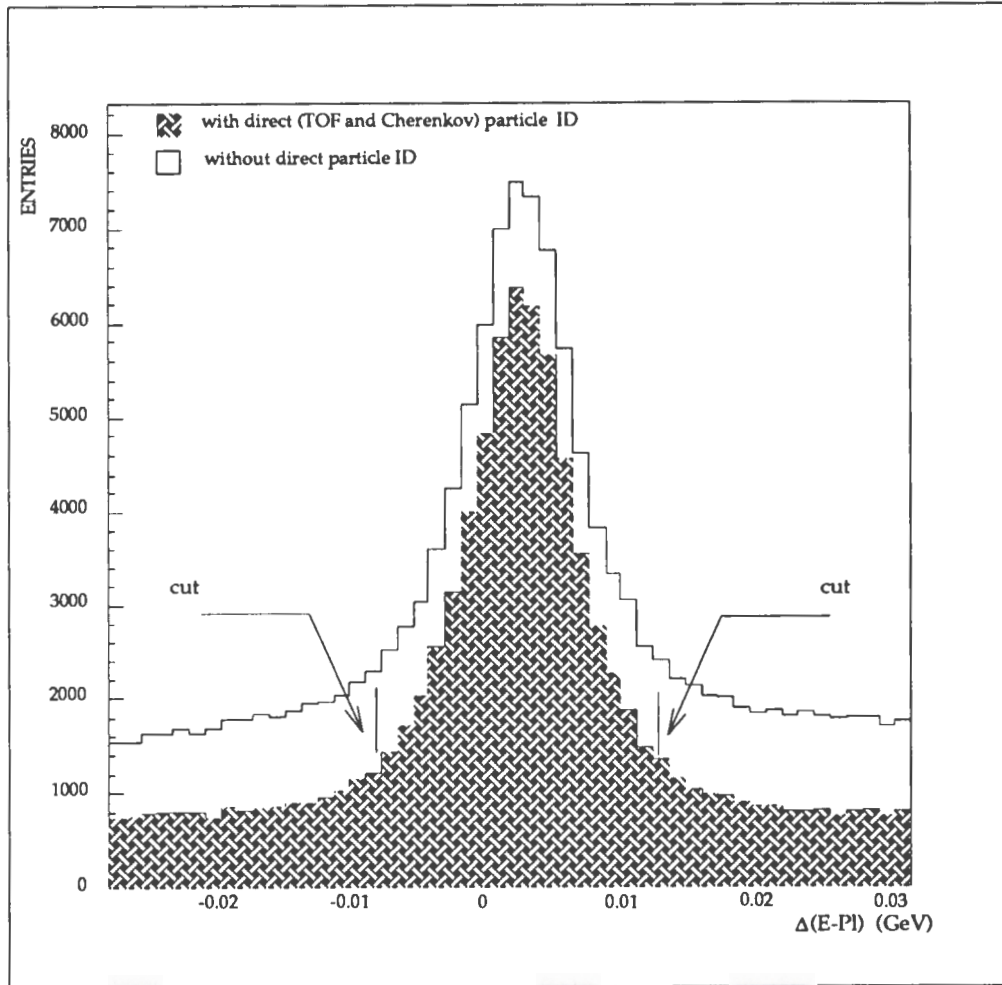
**FIGURE 7.** $\Delta(E - Pl)$ distribution, for the 8 track final state sample, without direct particle identification and with direct particle identification.

120

Event: 7EA3 51
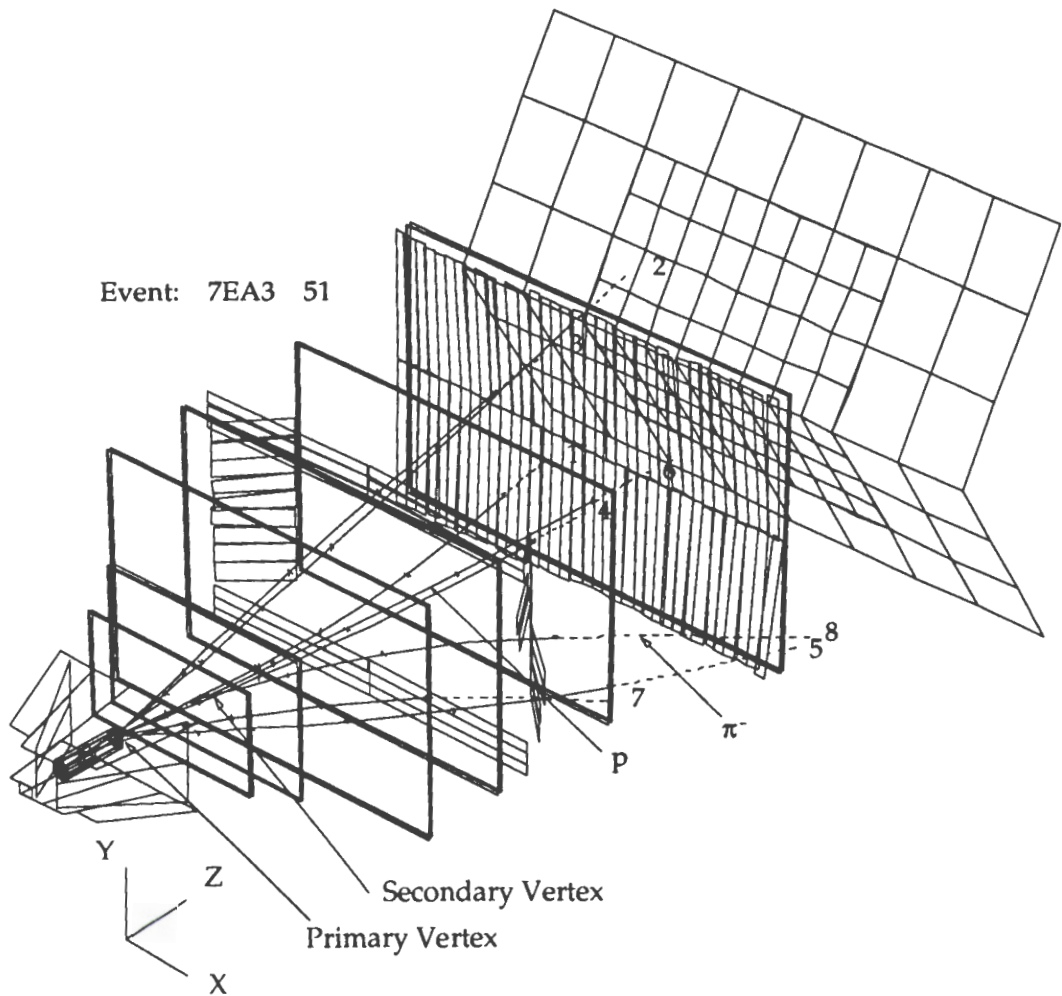
**FIGURE 8.** Spectrometer elements perspective, showing an 8 track reconstructed event.

Event: 7EA3 51
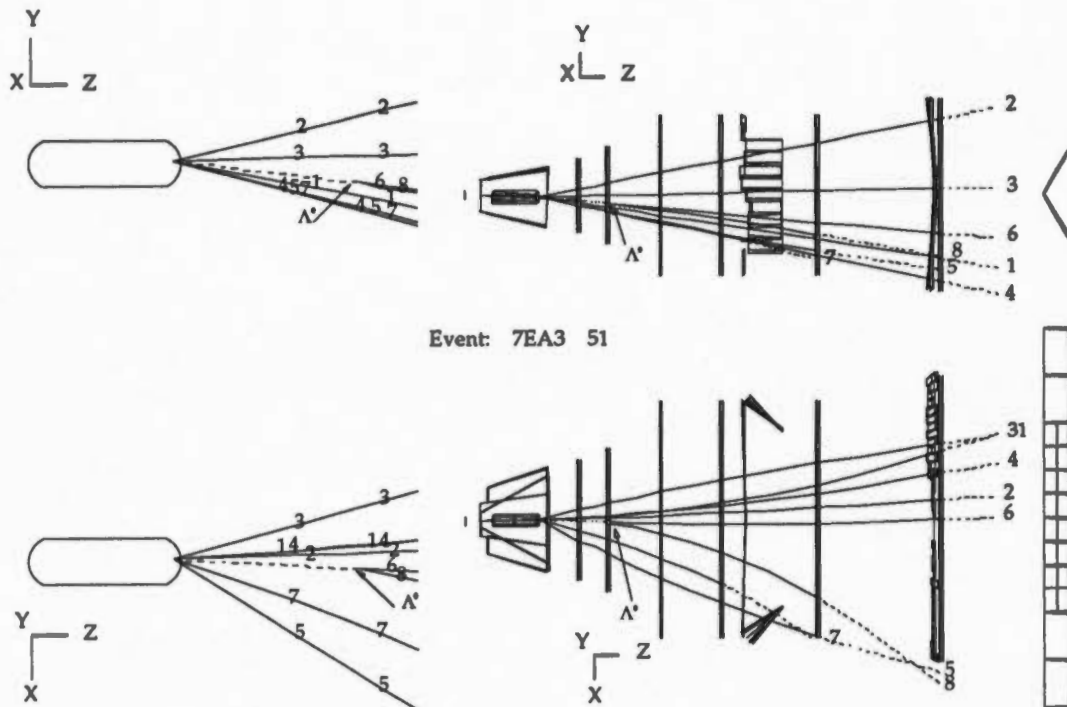
**FIGURE 9.** Two views of a reconstructed event from the 8 track final state sample. The same event that is in Figure 8. The primary vertex and the secondary vertex are shown.
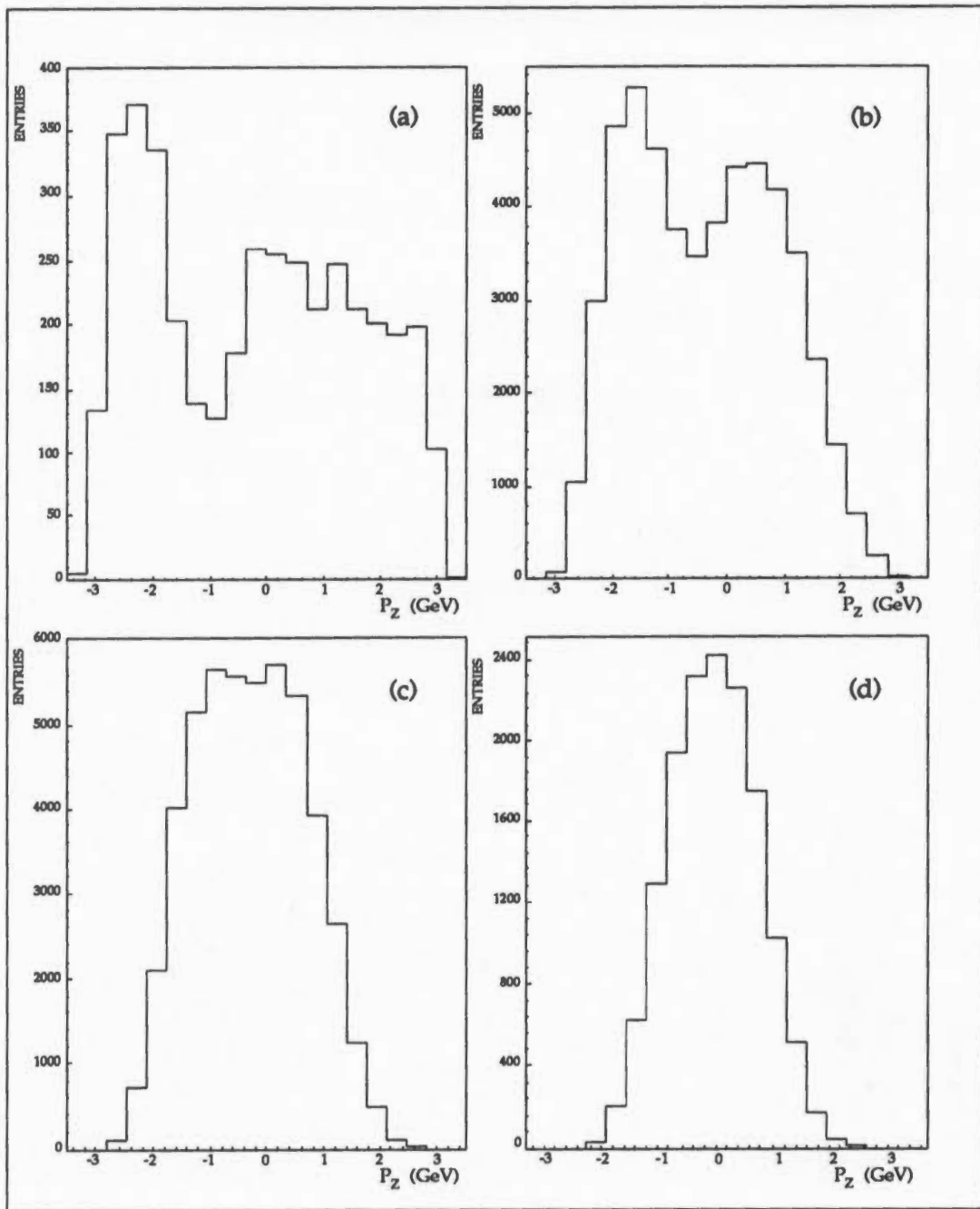
**FIGURE 10.** $P_z$ distributions. a) the 6 track final state, b) the 8 track final state, c) the 10 track final state, and d) the 12 track final state.

123
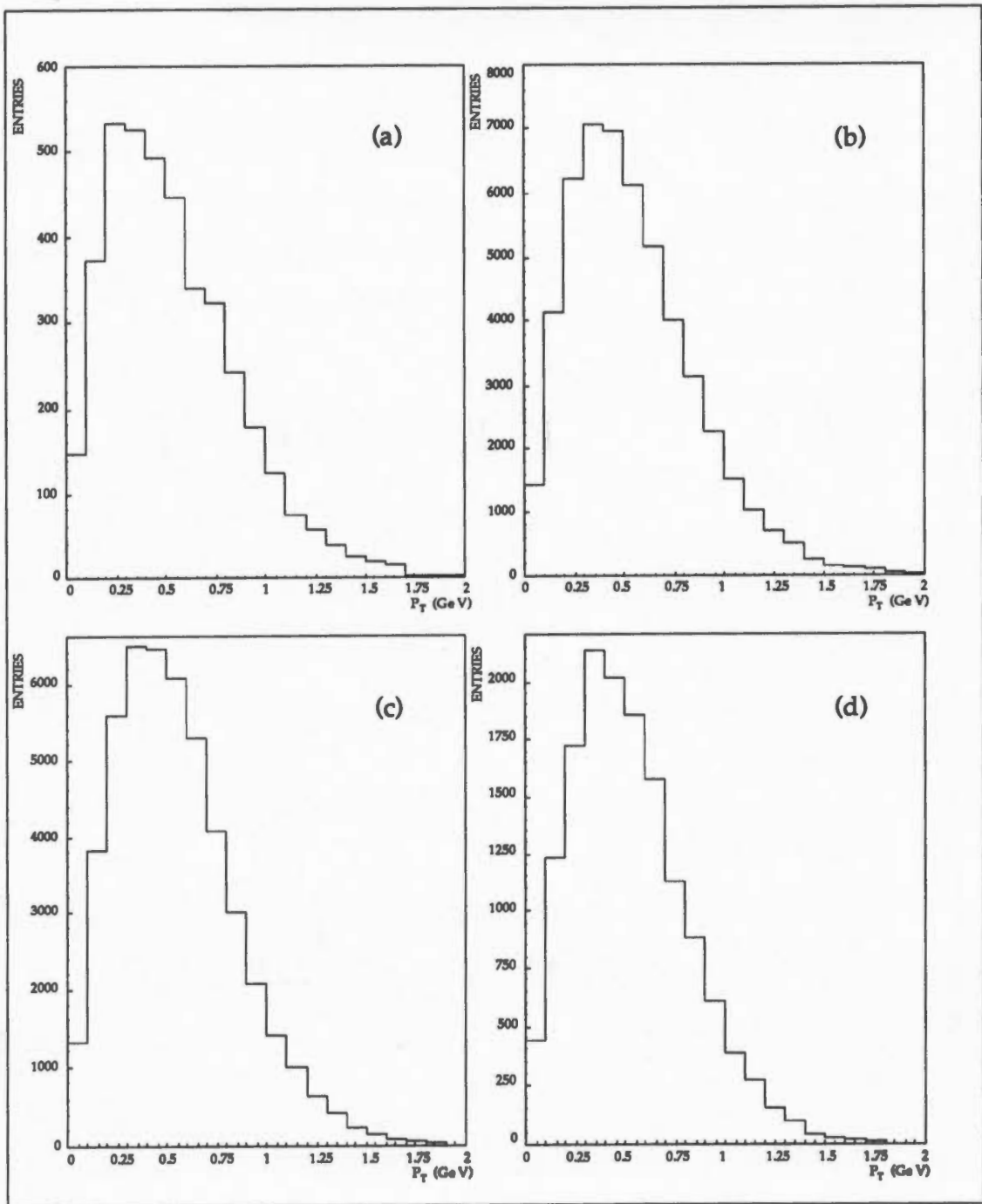
**FIGURE 11.** $P_T$ distributions. a) the 6 track final state, b) the 8 track final state, c) the 10 track final state, and d) the 12 track final state.

124
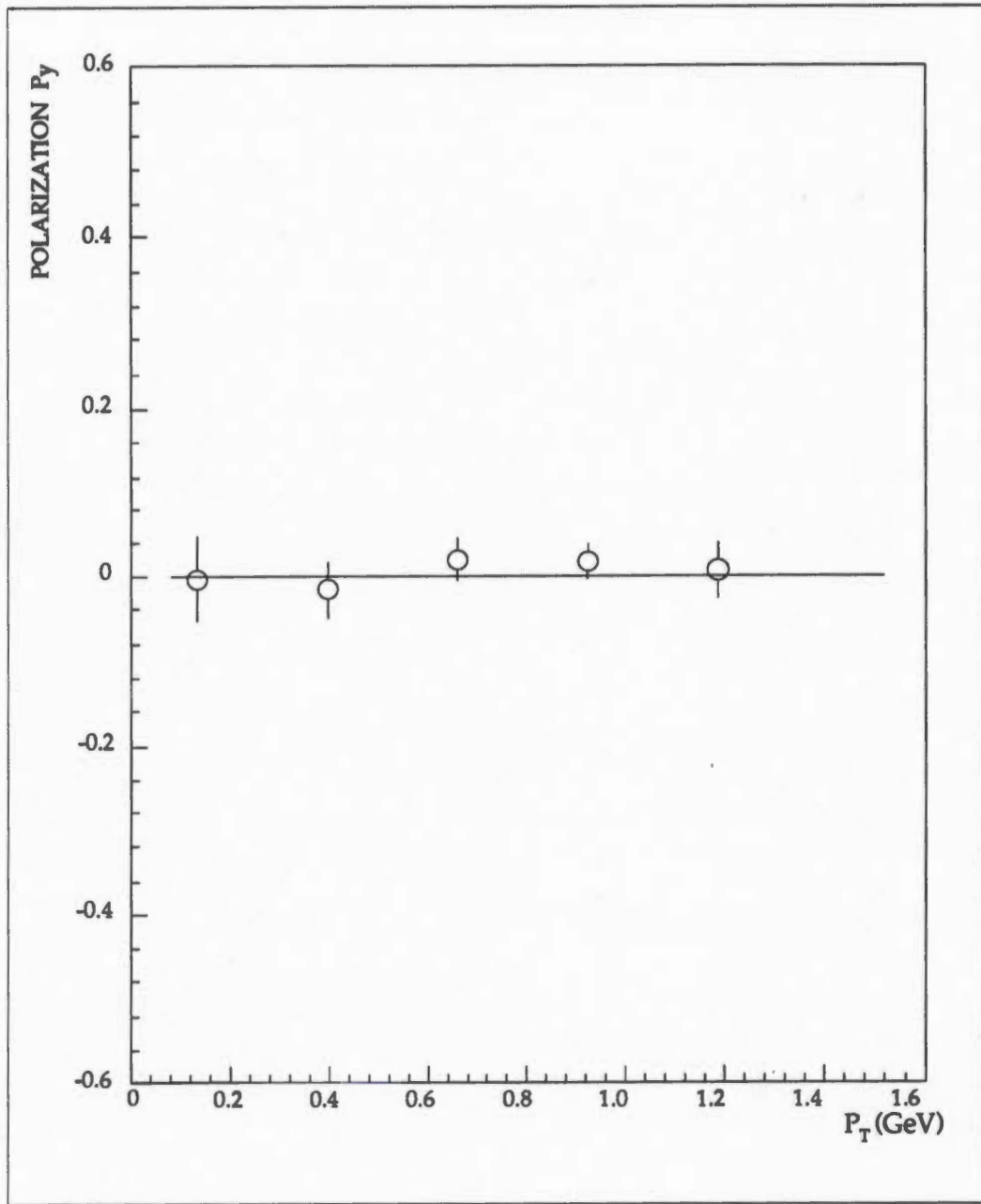
**FIGURE 12.** $\Lambda^0$ polarization for the entire 8 track final state sample.
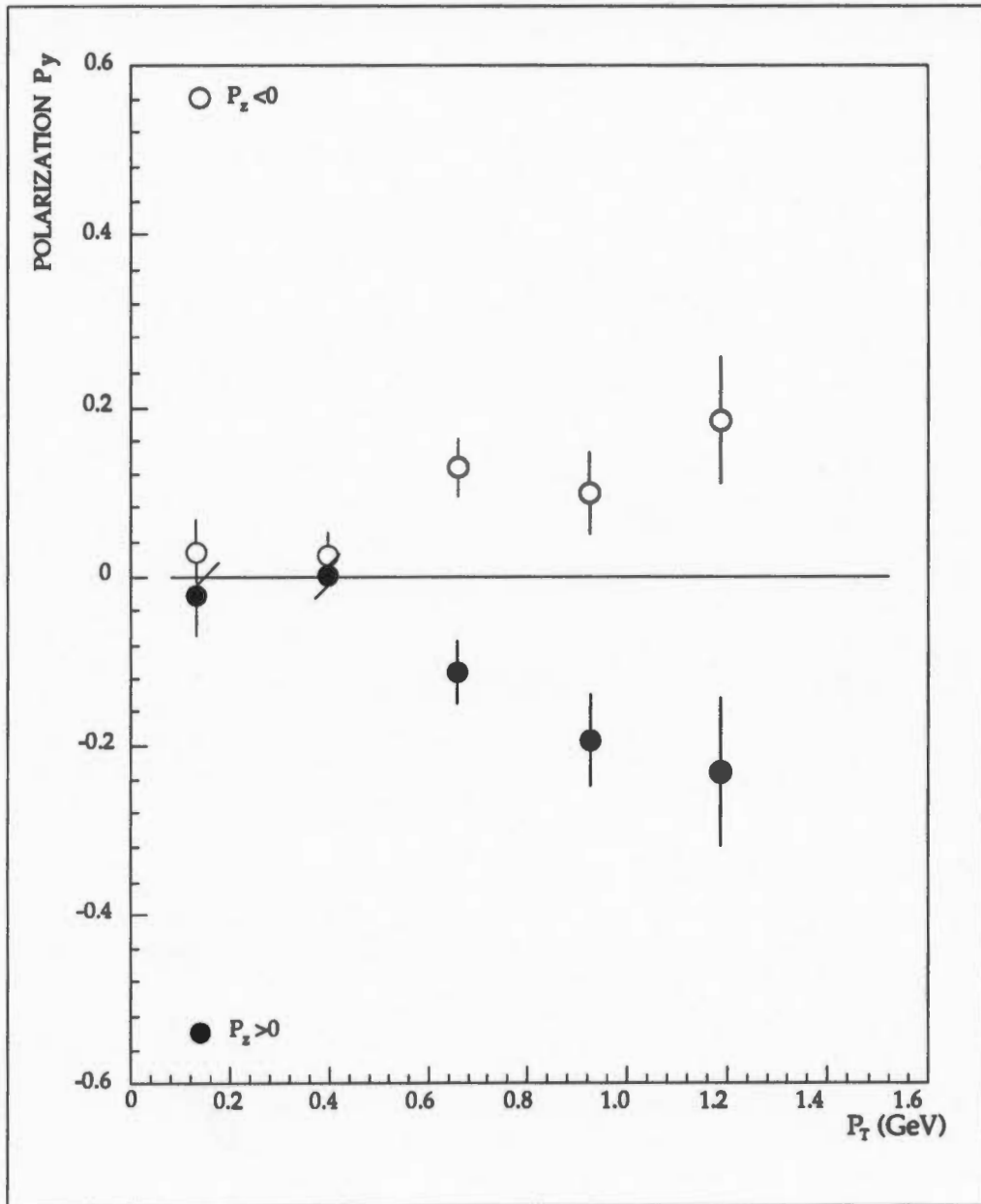
**FIGURE 13.** $\Lambda^0$ polarization, for the 8 track final state sample.

126
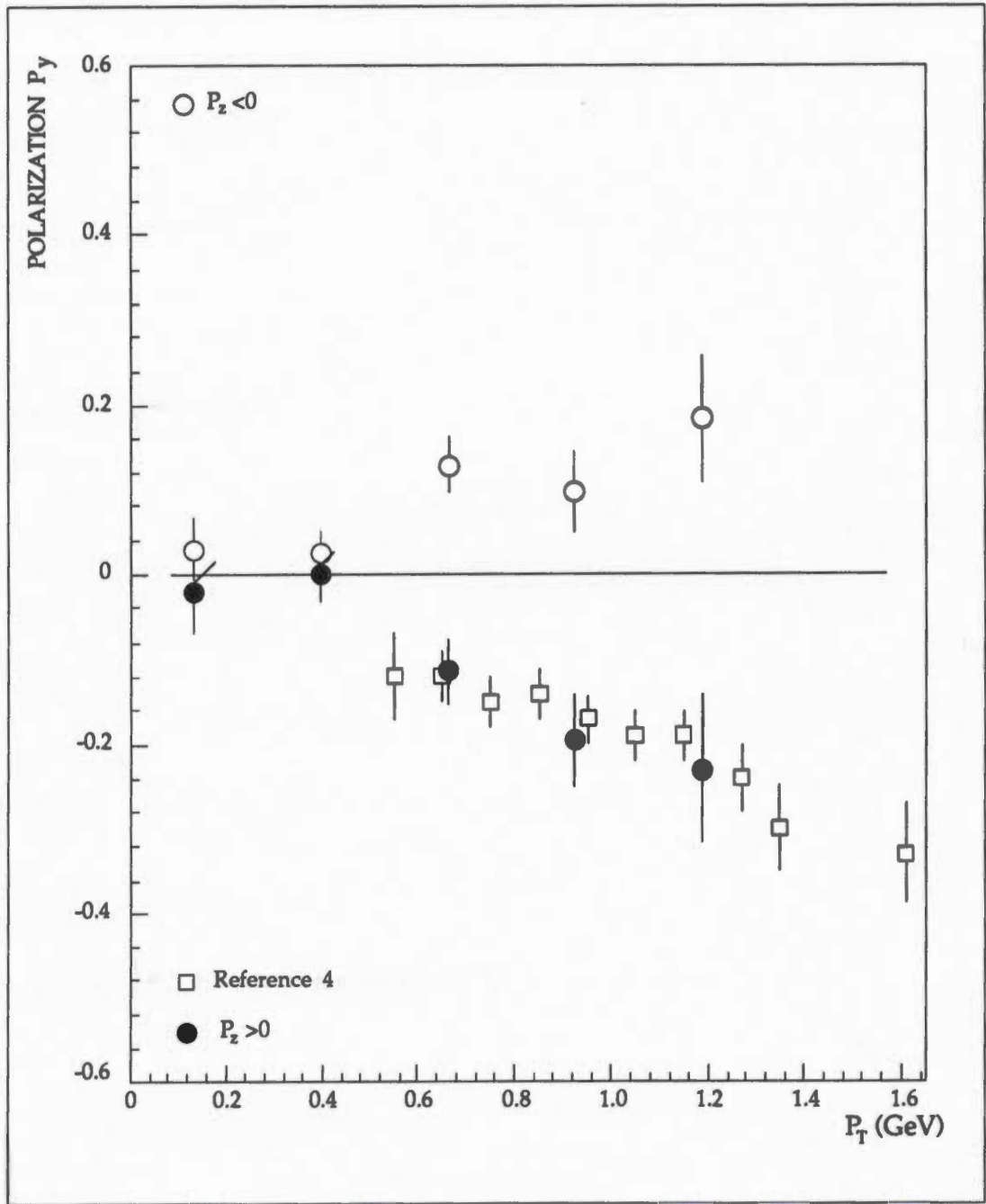
**FIGURE 14.** Comparison between the $\Lambda^0$ polarization, for the 8 track final state sample, and Reference 4 inclusive measurements.
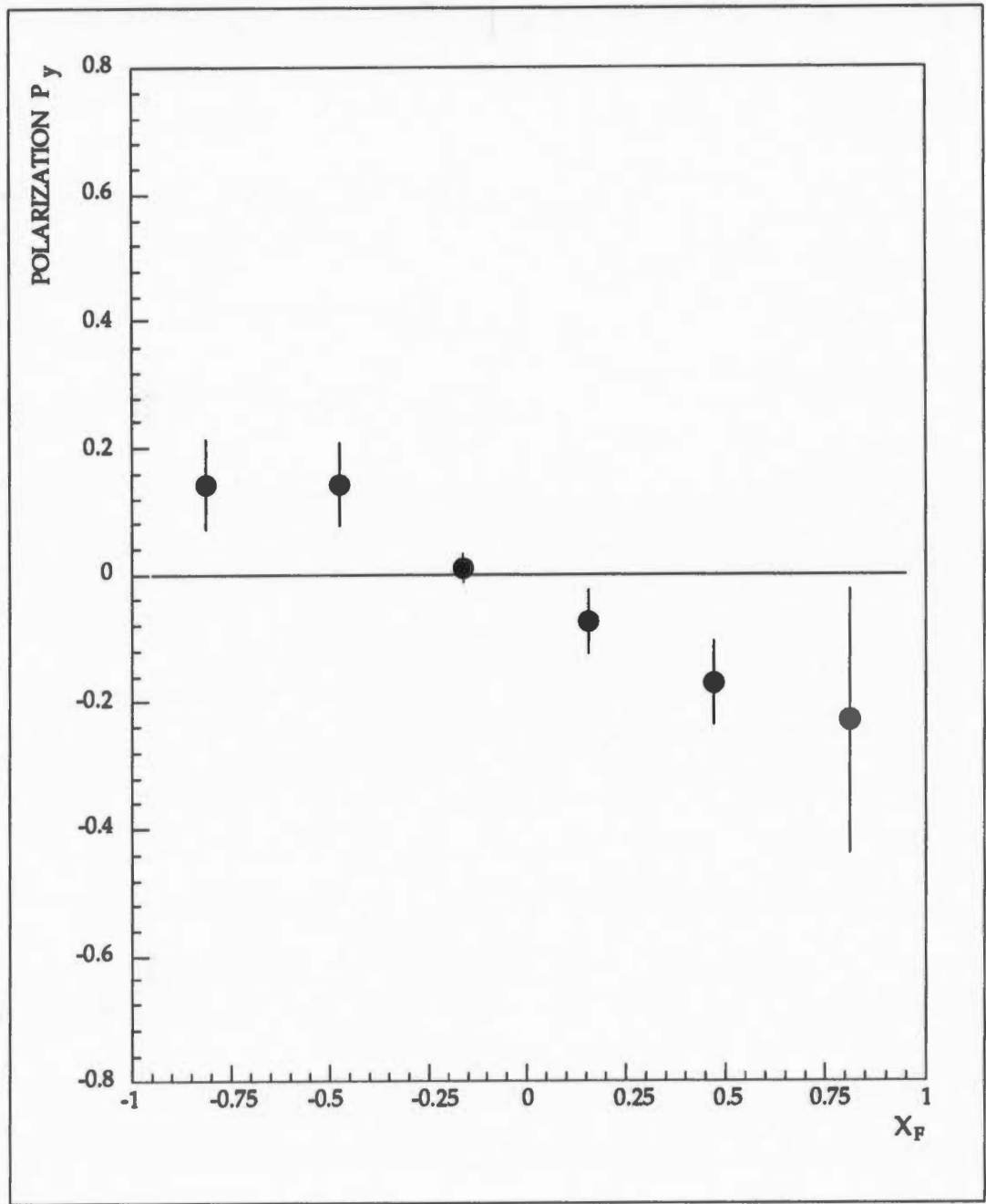
**FIGURE 15.** $\Lambda^0$ polarization, for the 8 track final state sample, as a function of $X_F$.

128
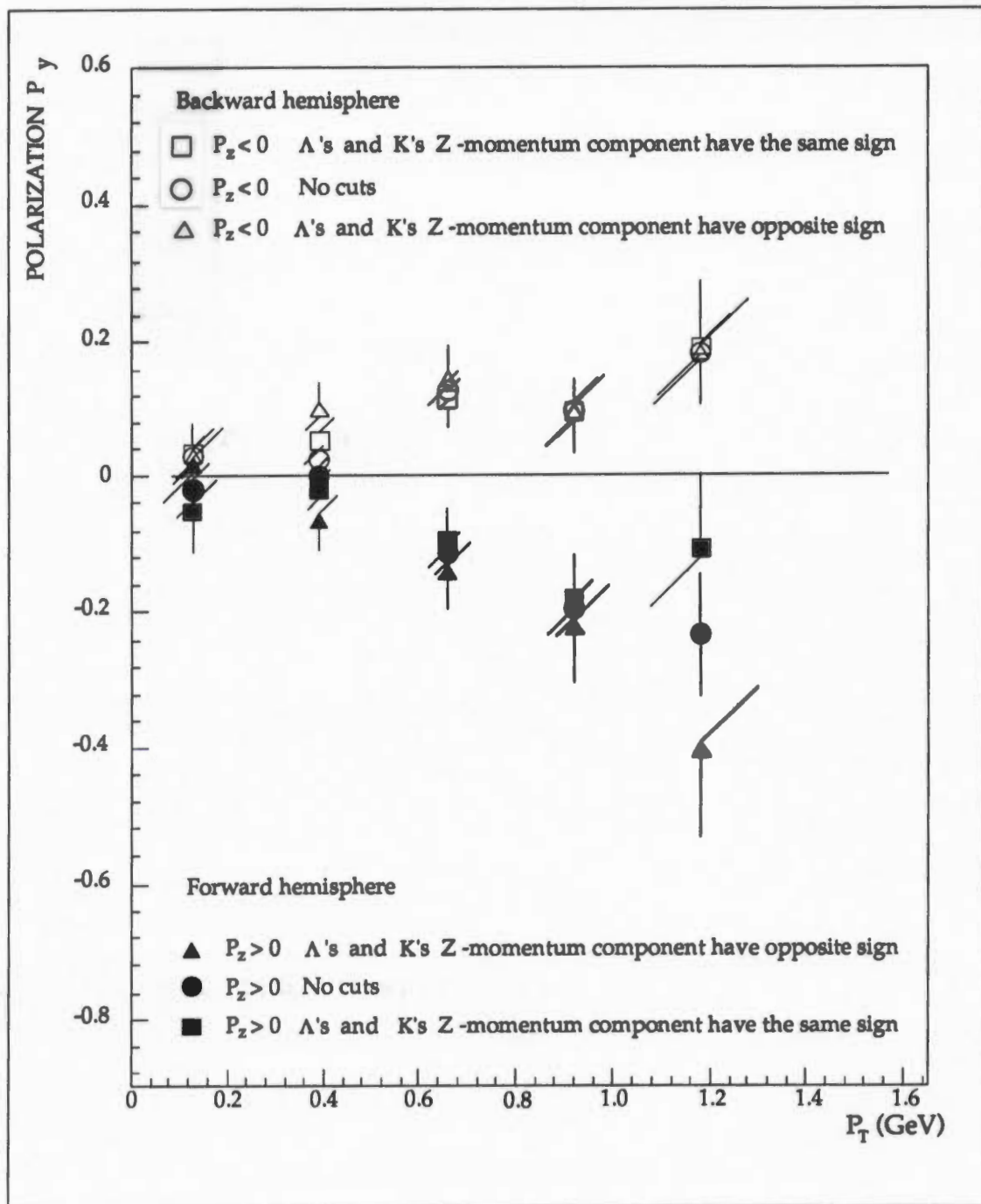
**FIGURE 16.** $\Lambda^0$ polarization, for the 8 track final state sample, in various kinematic regions.
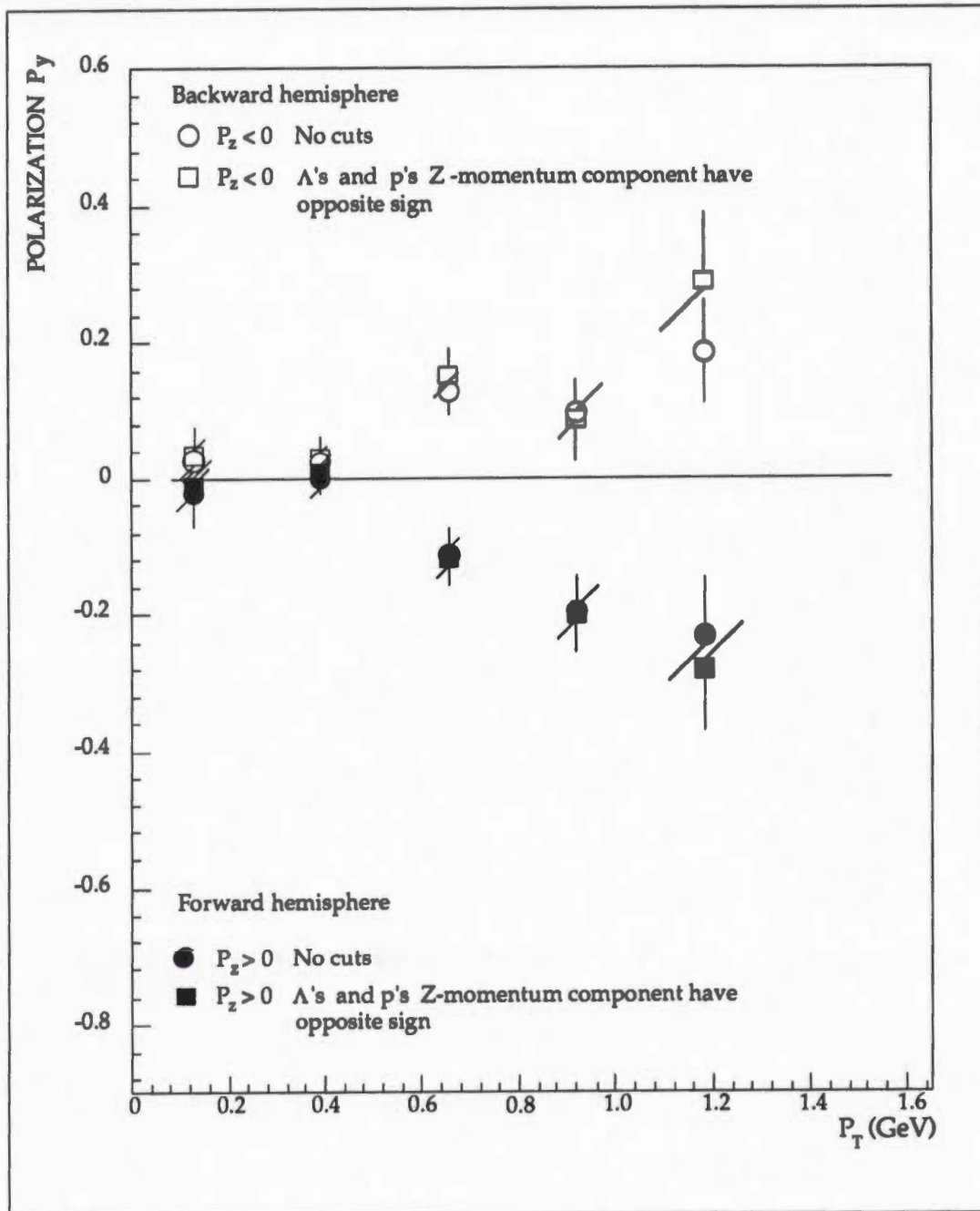
**FIGURE 17a.** $\Lambda^0$ polarization, for the 8 track final state sample, in various kinematic regions.
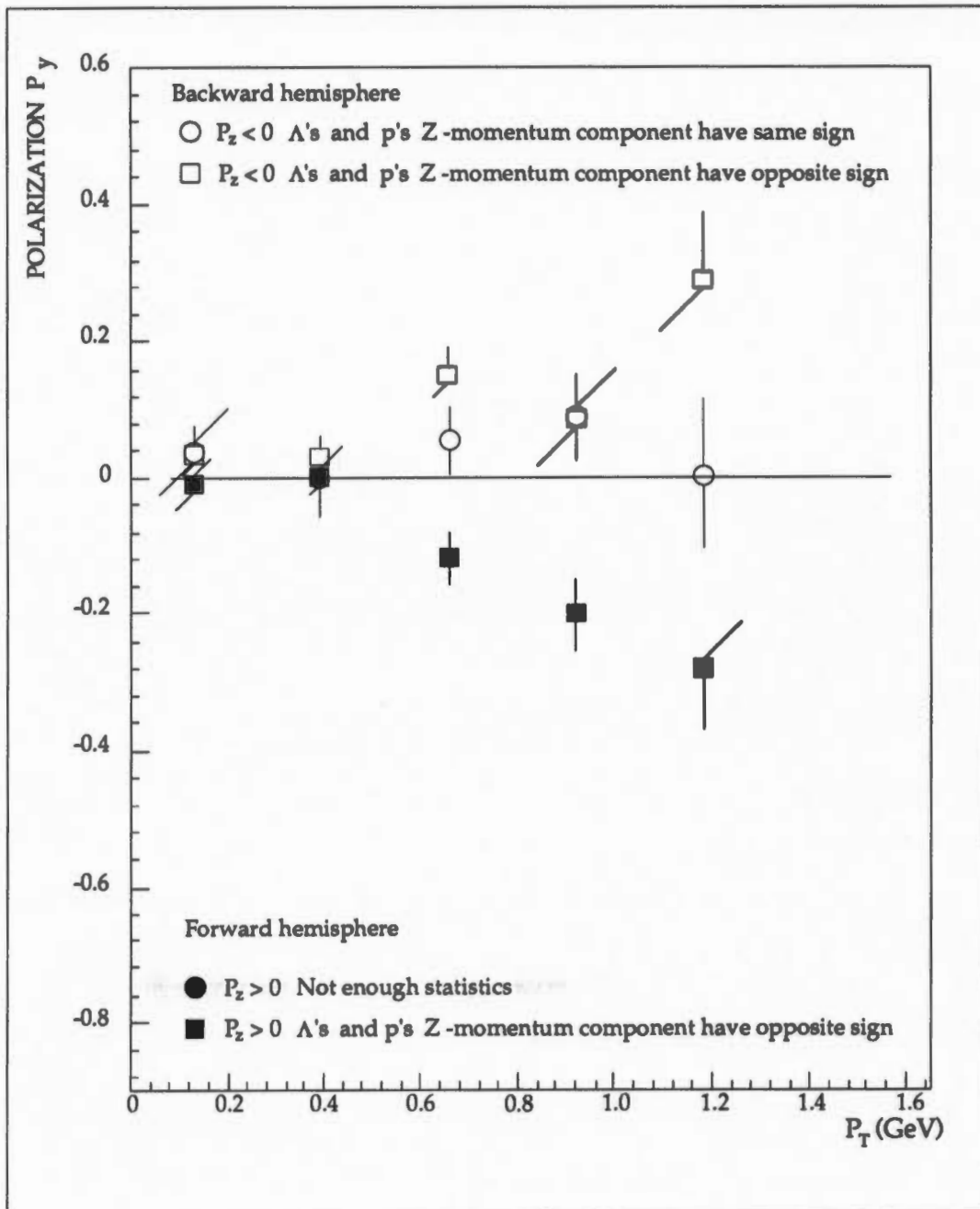
**FIGURE 17b.** $\Lambda^0$ polarization, for the 8 track final state sample, in various kinematic regions.
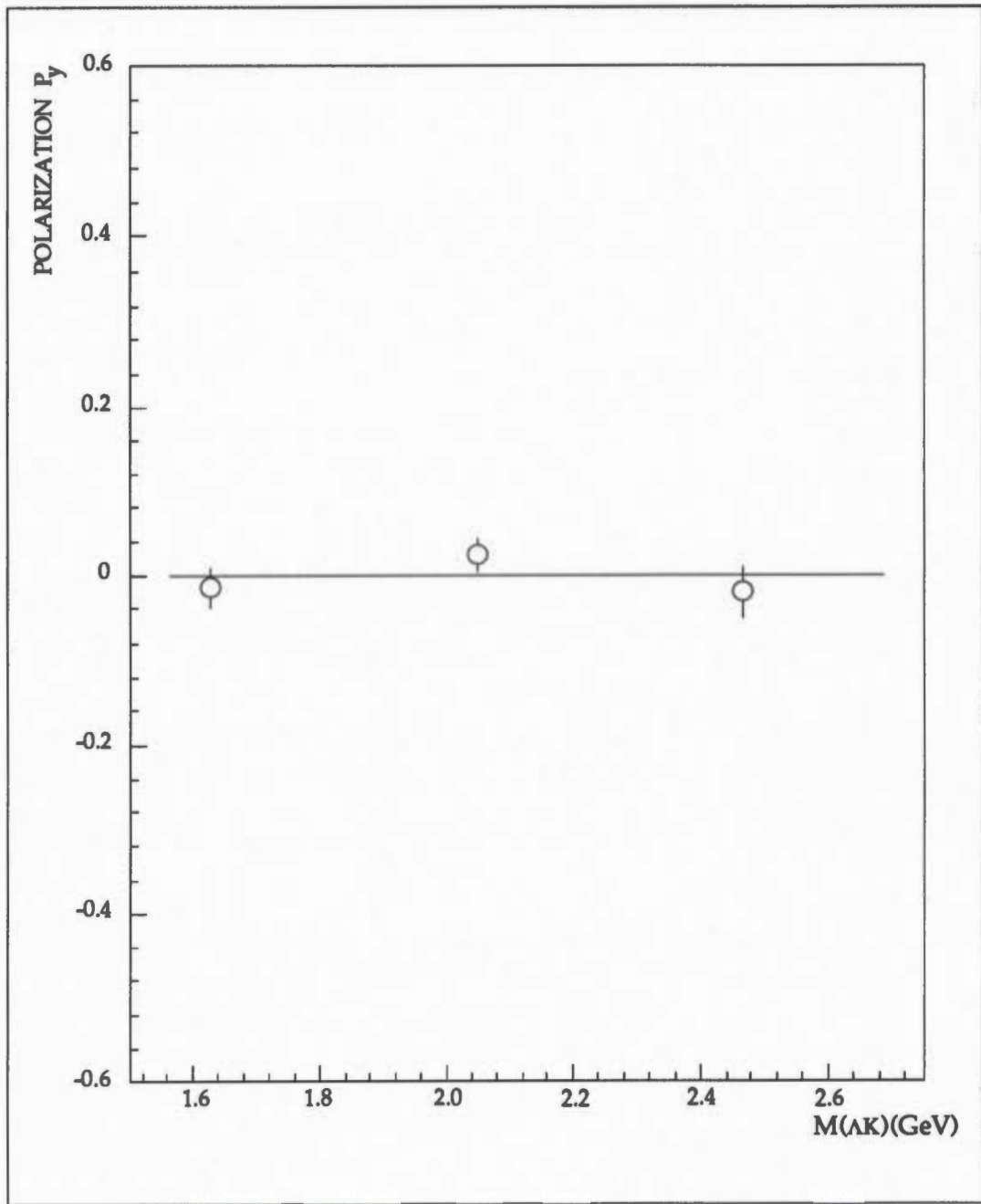
**FIGURE 18.** $\Lambda^0$ polarization, for the entire 8 track final state sample, as a function of $M(\Lambda K)$.
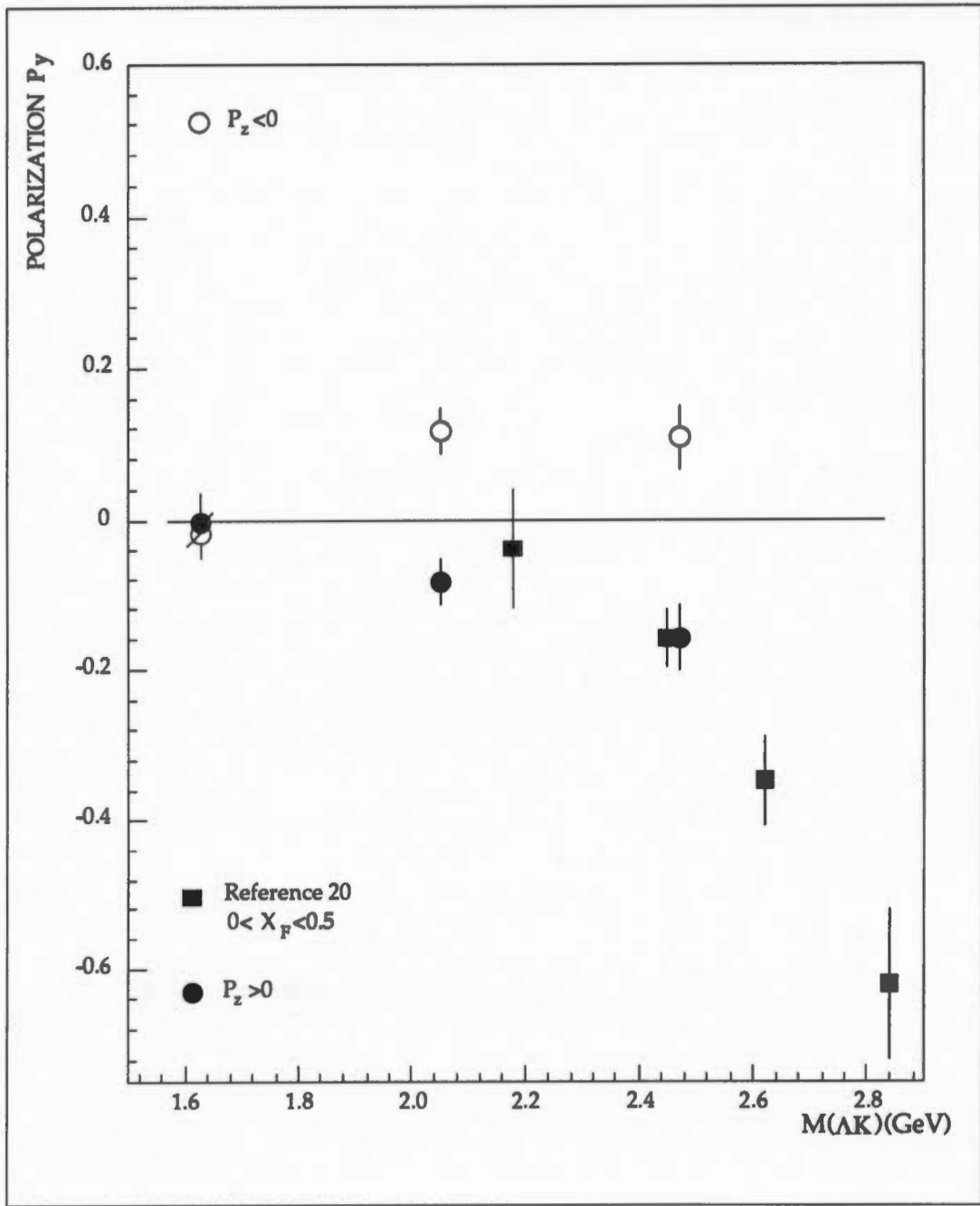
**FIGURE 19.** $\Lambda^0$ polarization, for the 8 track final state sample, as a function of $M(\Lambda K)$. We compare with Reference 20 data.
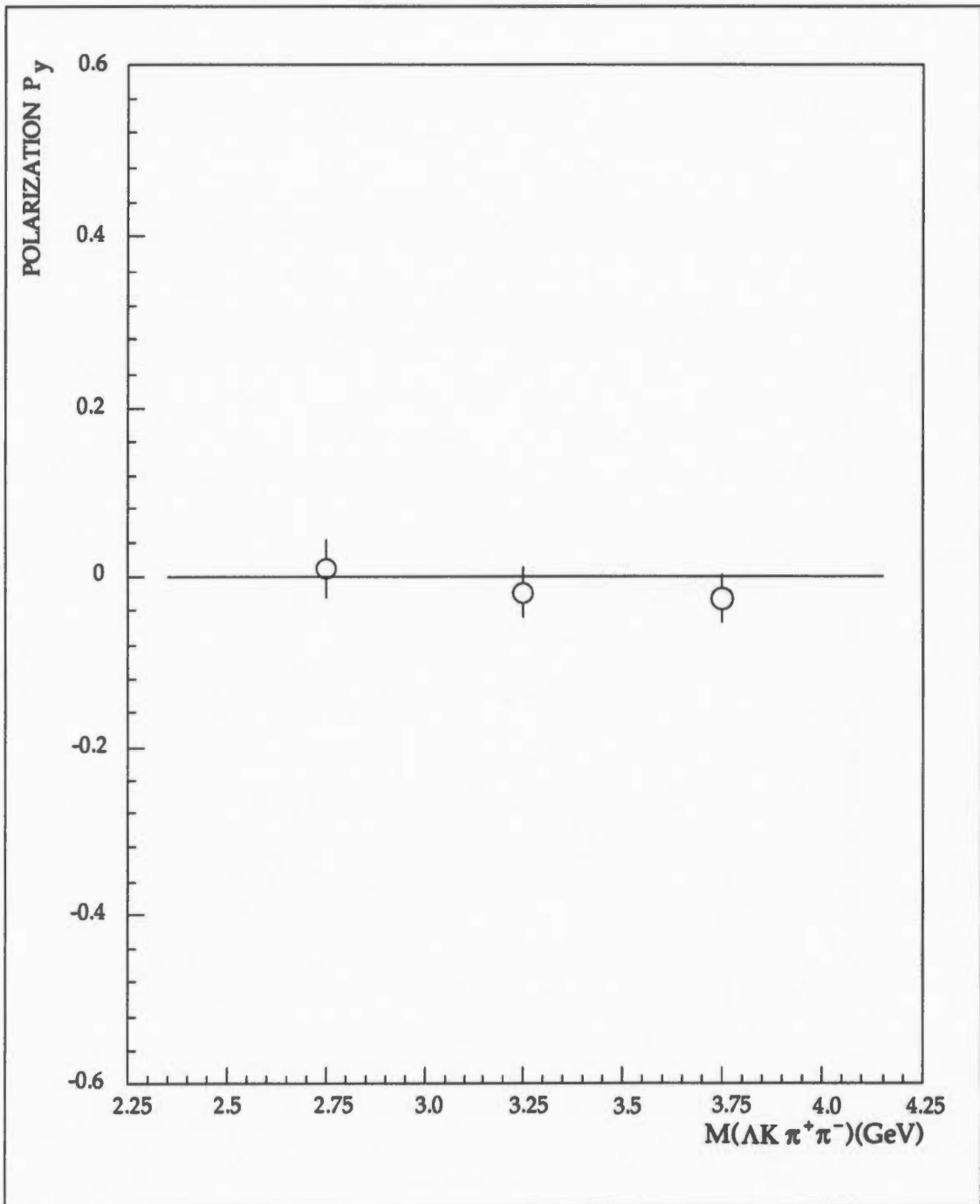
FIGURE 20. $\Lambda^0$ polarization, for the entire 8 track final state sample, as a function of $M(\Lambda K \pi^+ \pi^-)$.
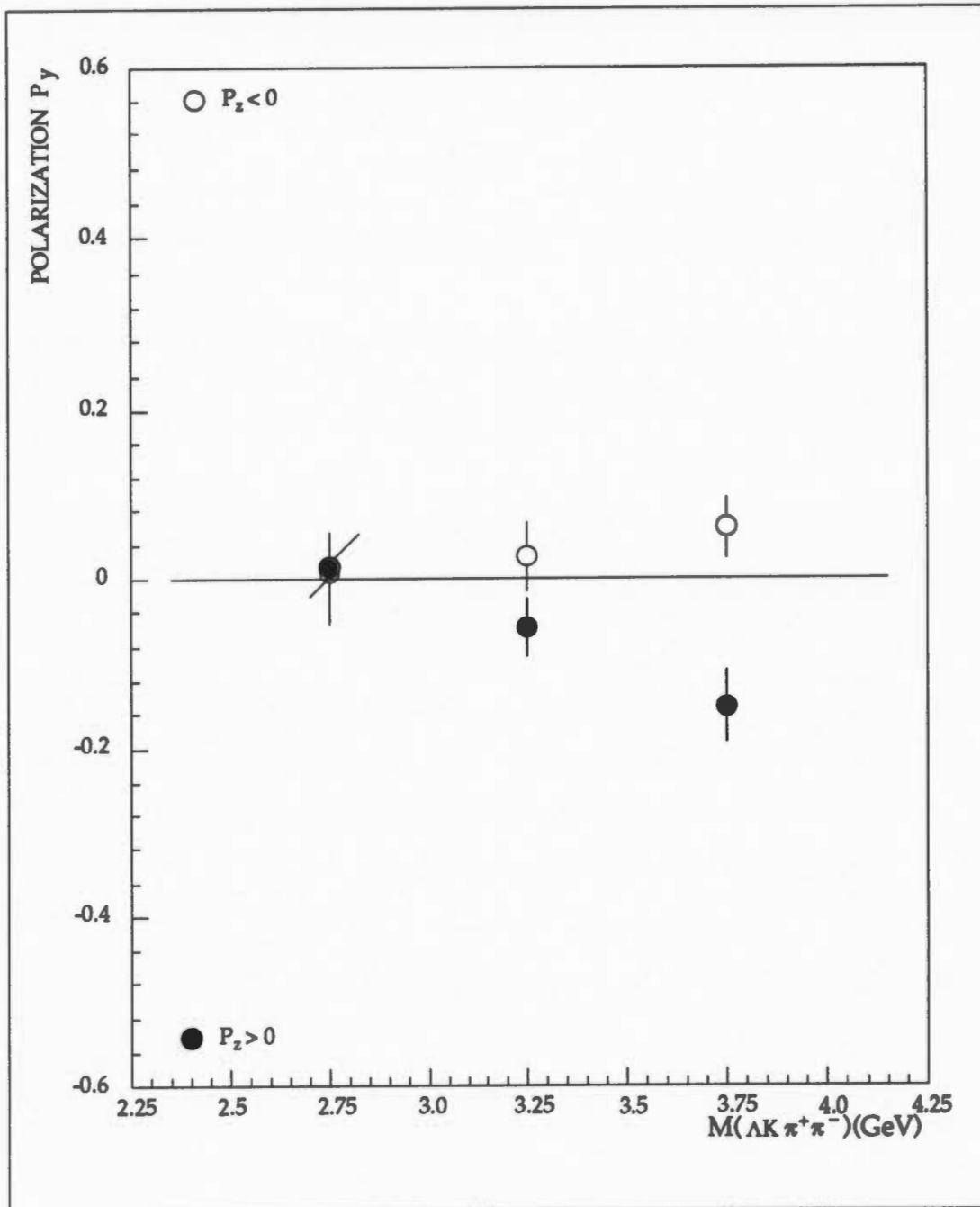
**FIGURE 21.** $\Lambda^0$ polarization, for the 8 track final state sample, as a function of $M(\Lambda K \pi^+ \pi^-)$.
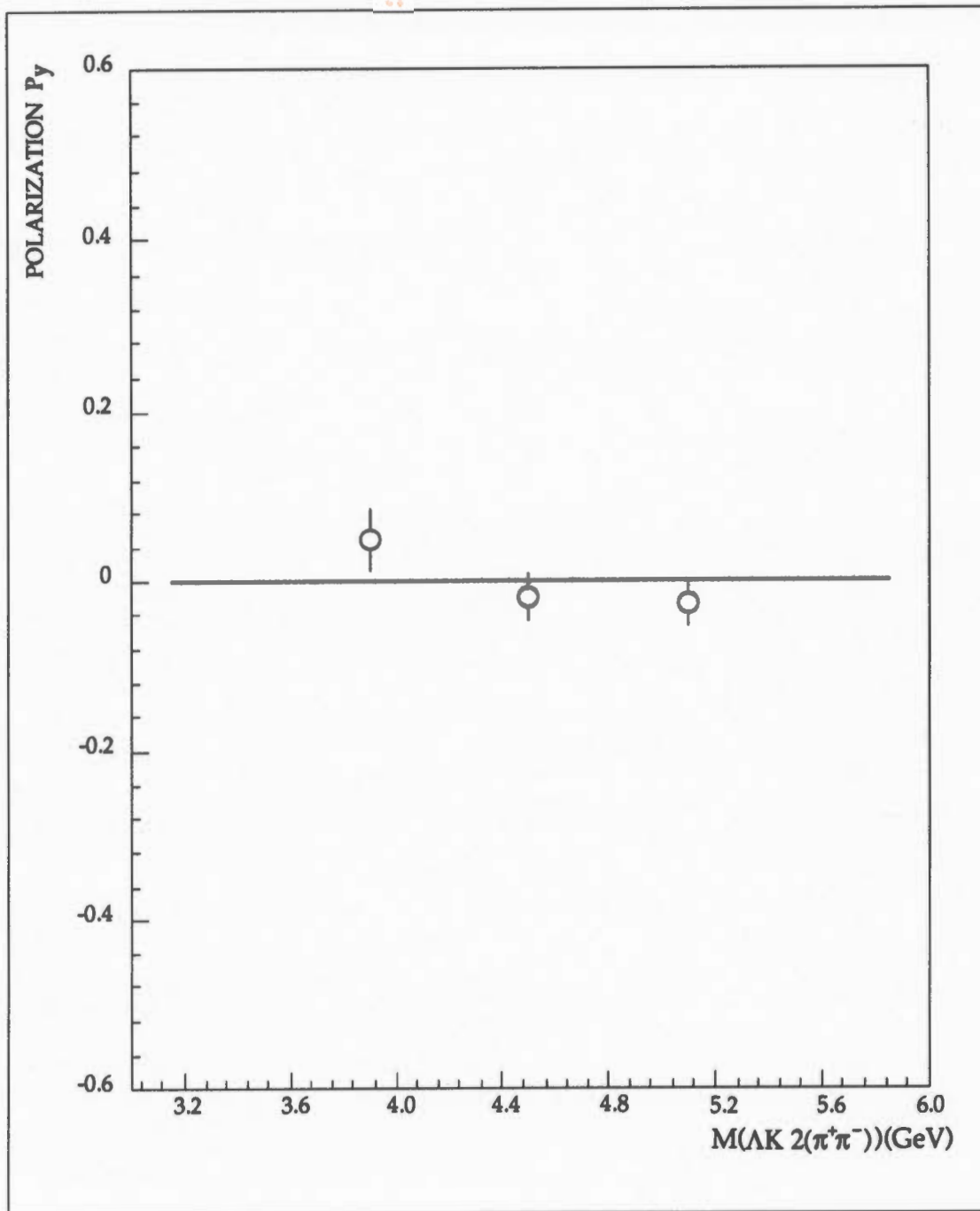
**FIGURE 22.** $\Lambda^0$ polarization, for the entire 8 track final state sample, as a function of $M(\Lambda K 2(\pi^+\pi^-))$.
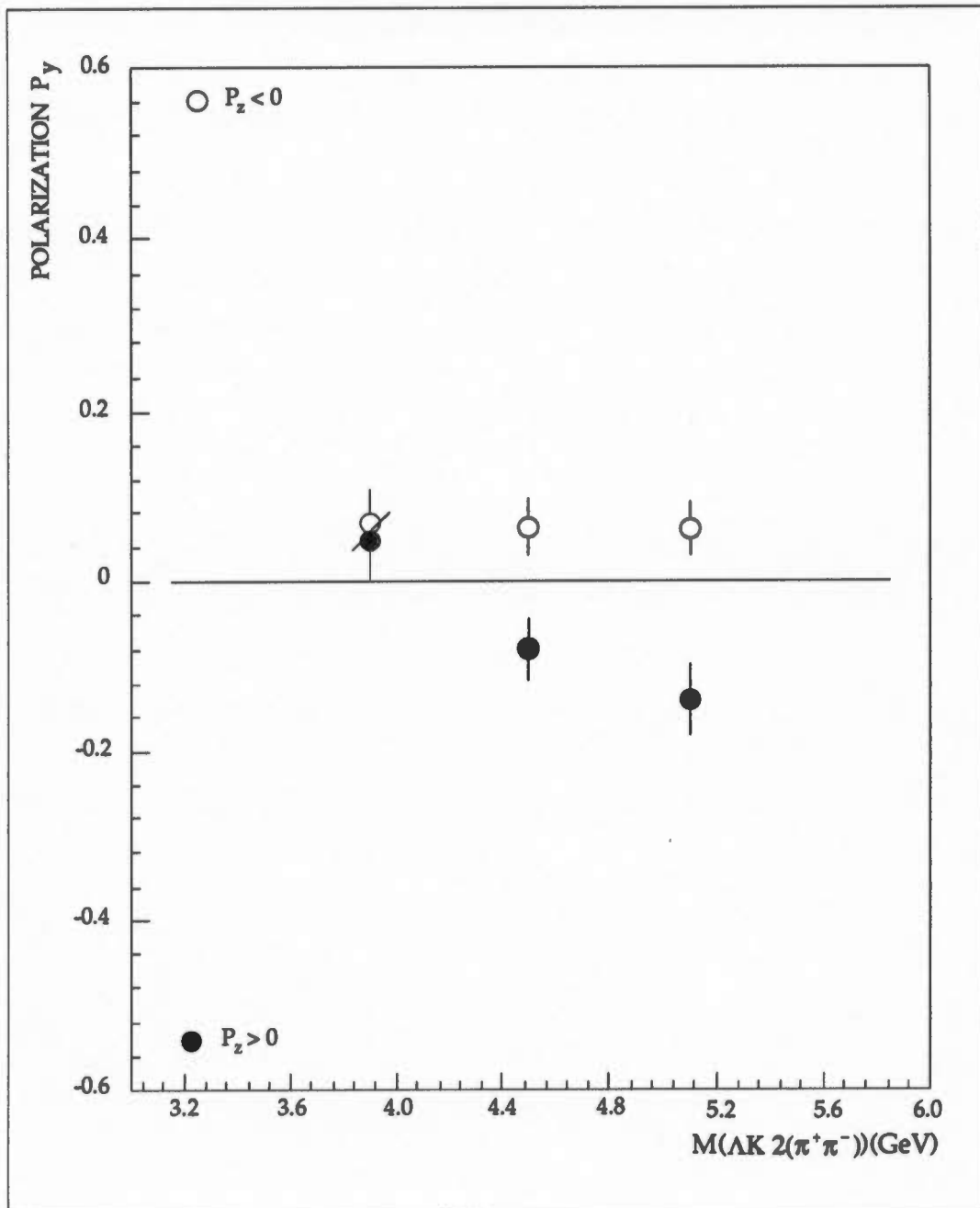
**FIGURE 23.** $\Lambda^0$ polarization, for the 8 track final state sample, as a function of $M(\Lambda K 2(\pi^+\pi^-))$.
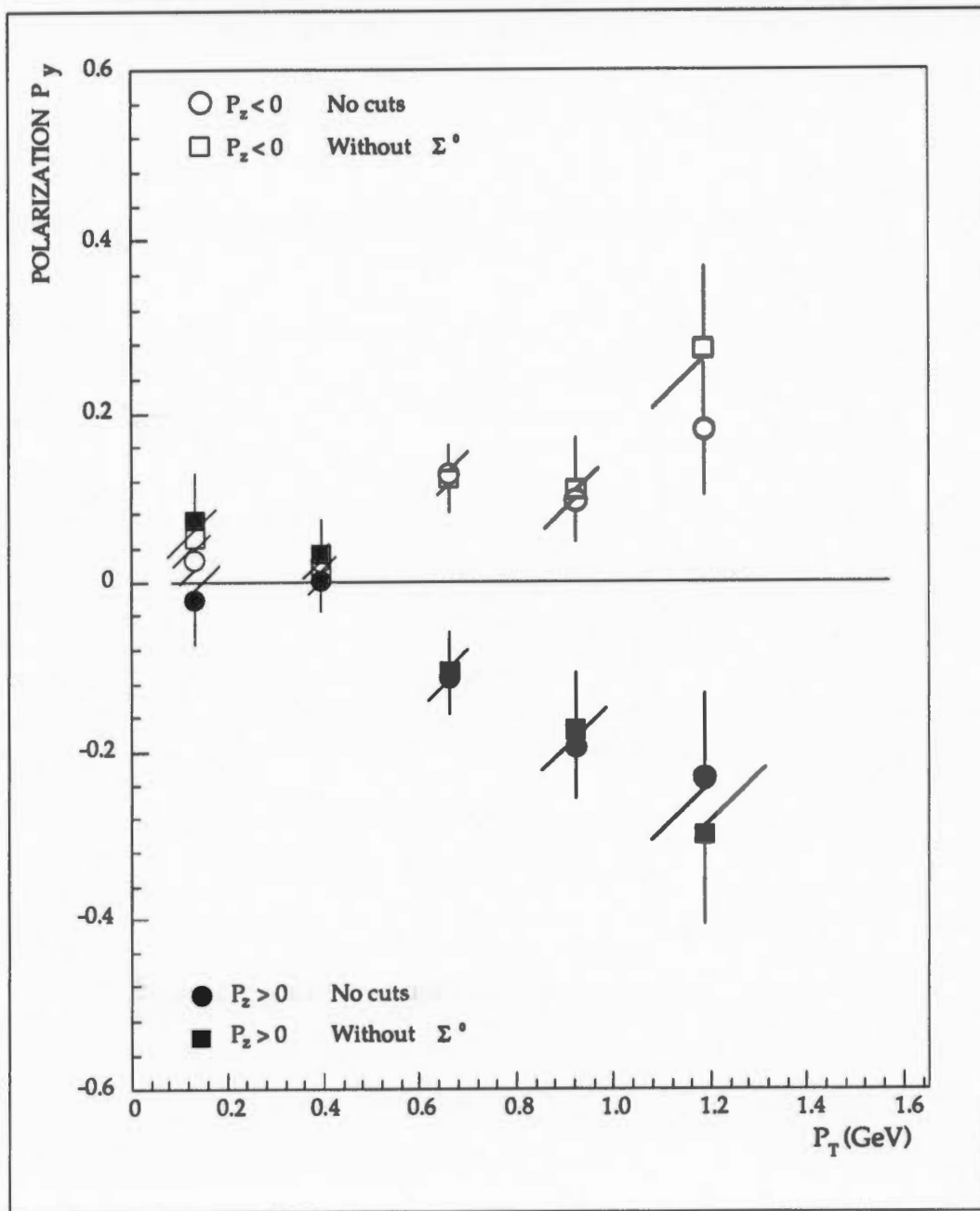
**FIGURE 24.** $\Lambda^0$ polarization, for the 8 track final state sample, without $\Lambda^0$ from $\Sigma^0 \to \Lambda^0 \gamma$. We compare with that from the 8 track final state sample.

138
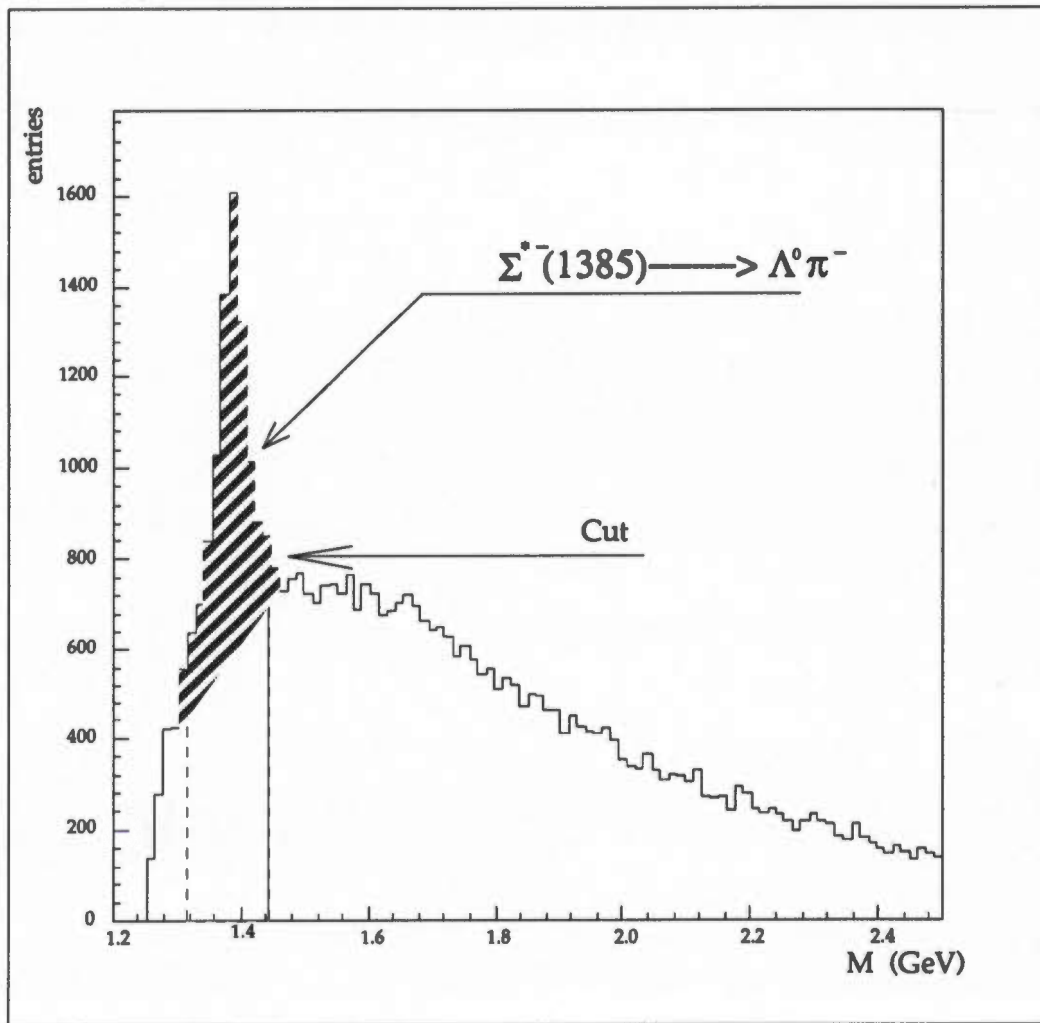
**FIGURE 25.** Invariant mass of $\Lambda^0\pi^-$ combinations from the 8 track final state sample.
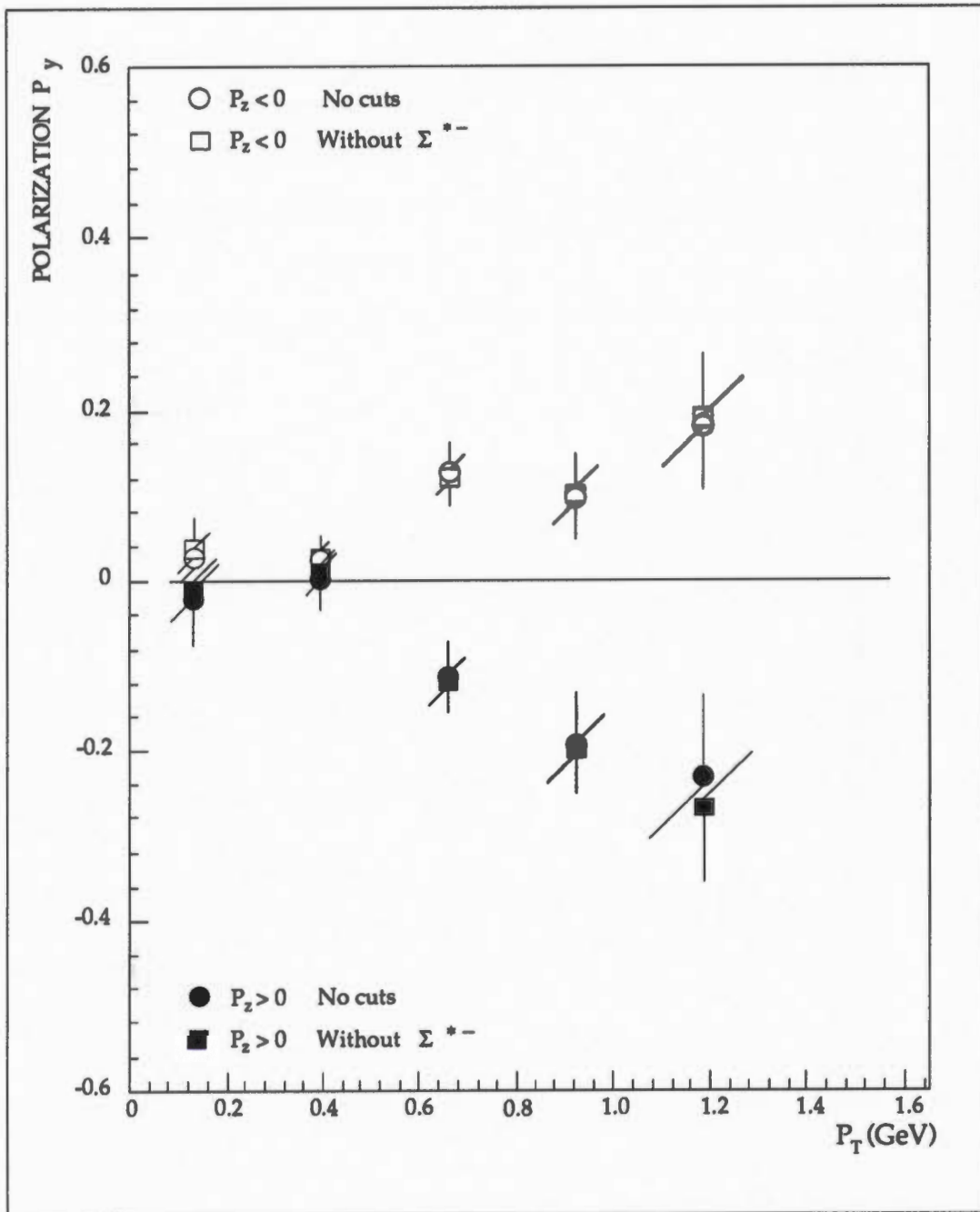
**FIGURE 26.** $\Lambda^0$ polarization, for the 8 track final state sample, without $\Lambda^0$ from $\Sigma^{*-} \to \Lambda^0 \pi^-$. We compare with that from the 8 track final state sample.

140
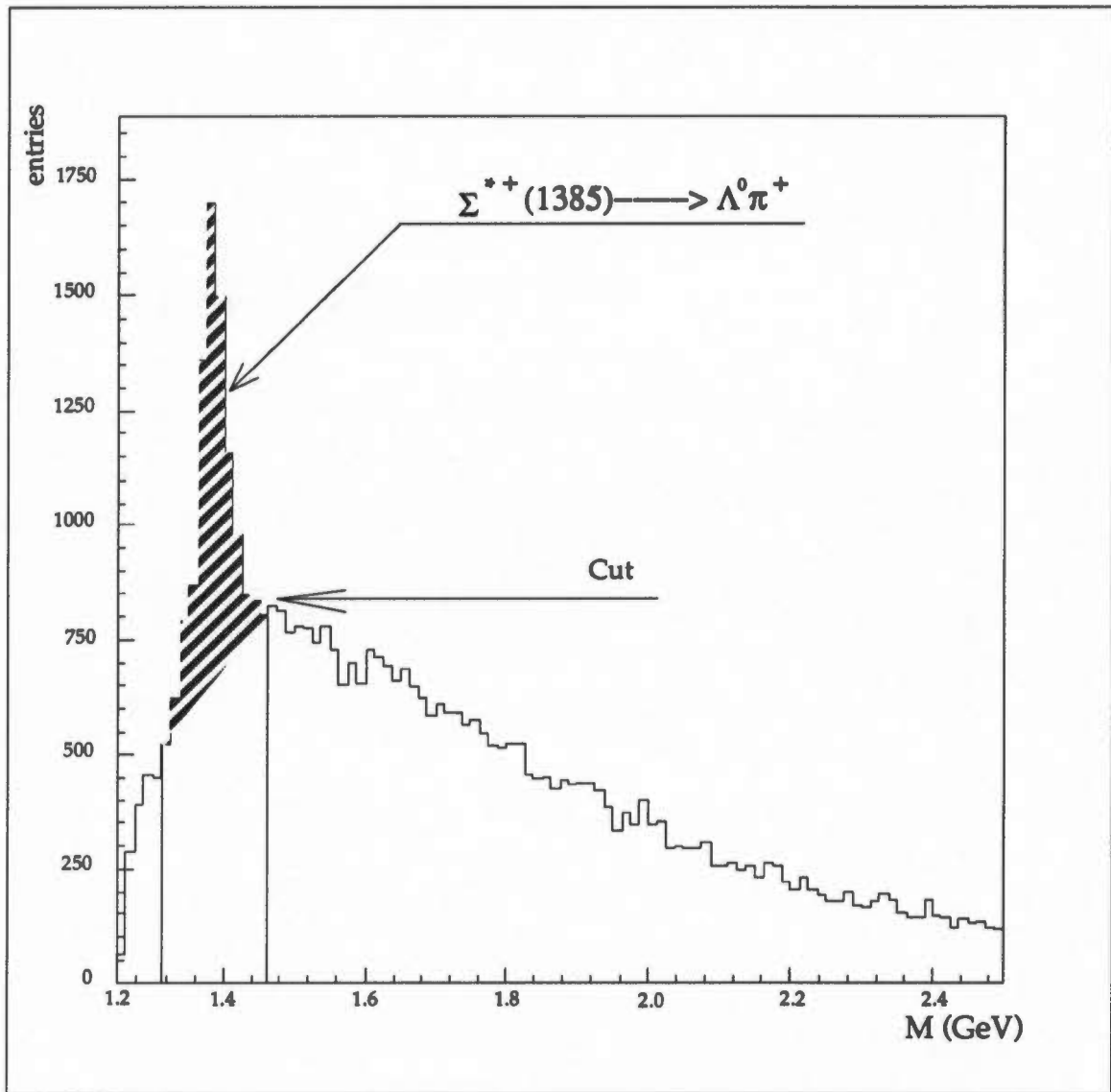
**FIGURE 27.** Invariant mass of $\Lambda^0 \pi^+$ combinations from the 8 track final state sample.

141
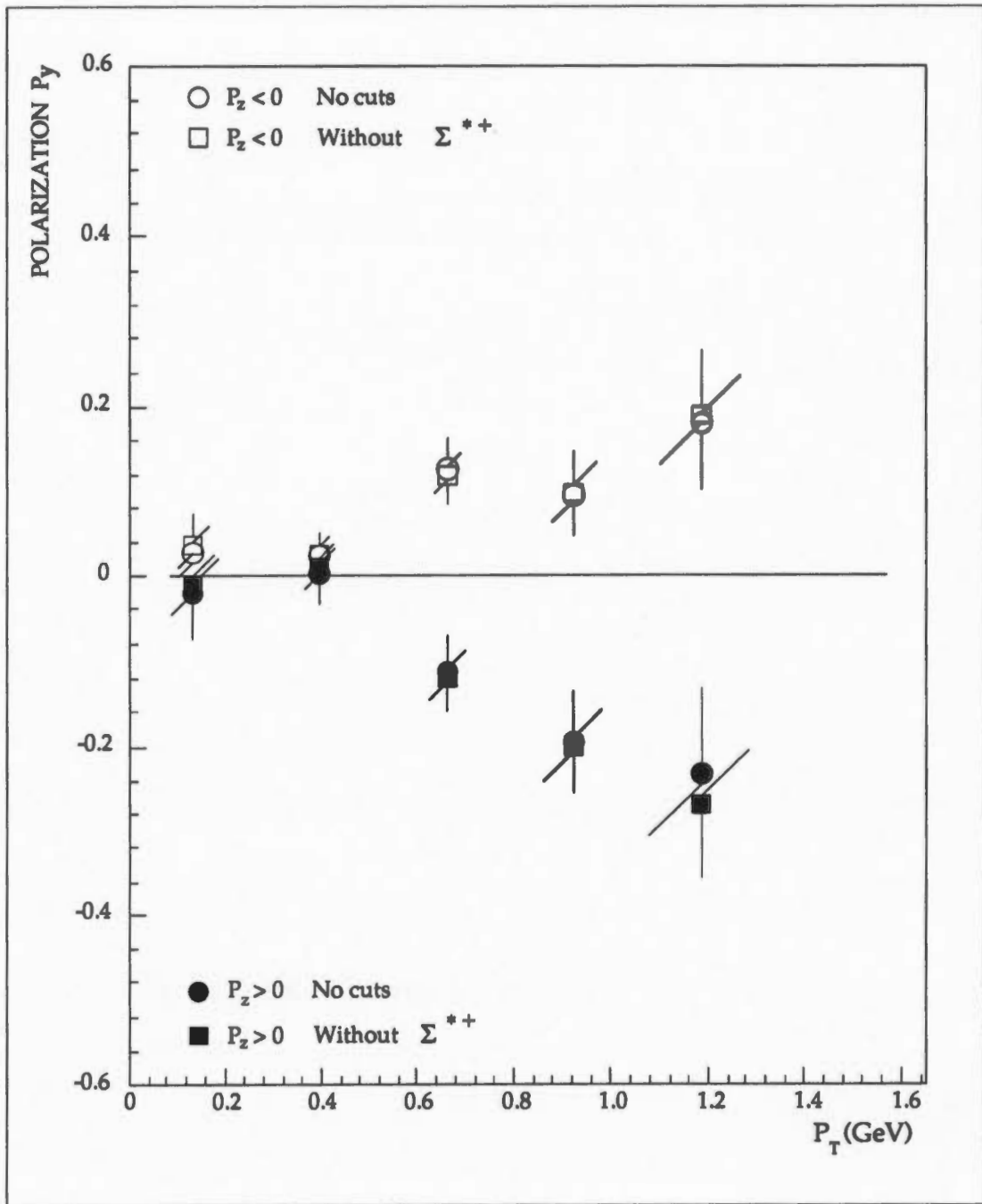
**FIGURE 28.**  $\Lambda^0$ polarization, for the 8 track final state sample, without $\Lambda^0$ from $\Sigma^{*+} \rightarrow \Lambda^0 \pi^+$. We compare with that from the 8 track final state sample.

142
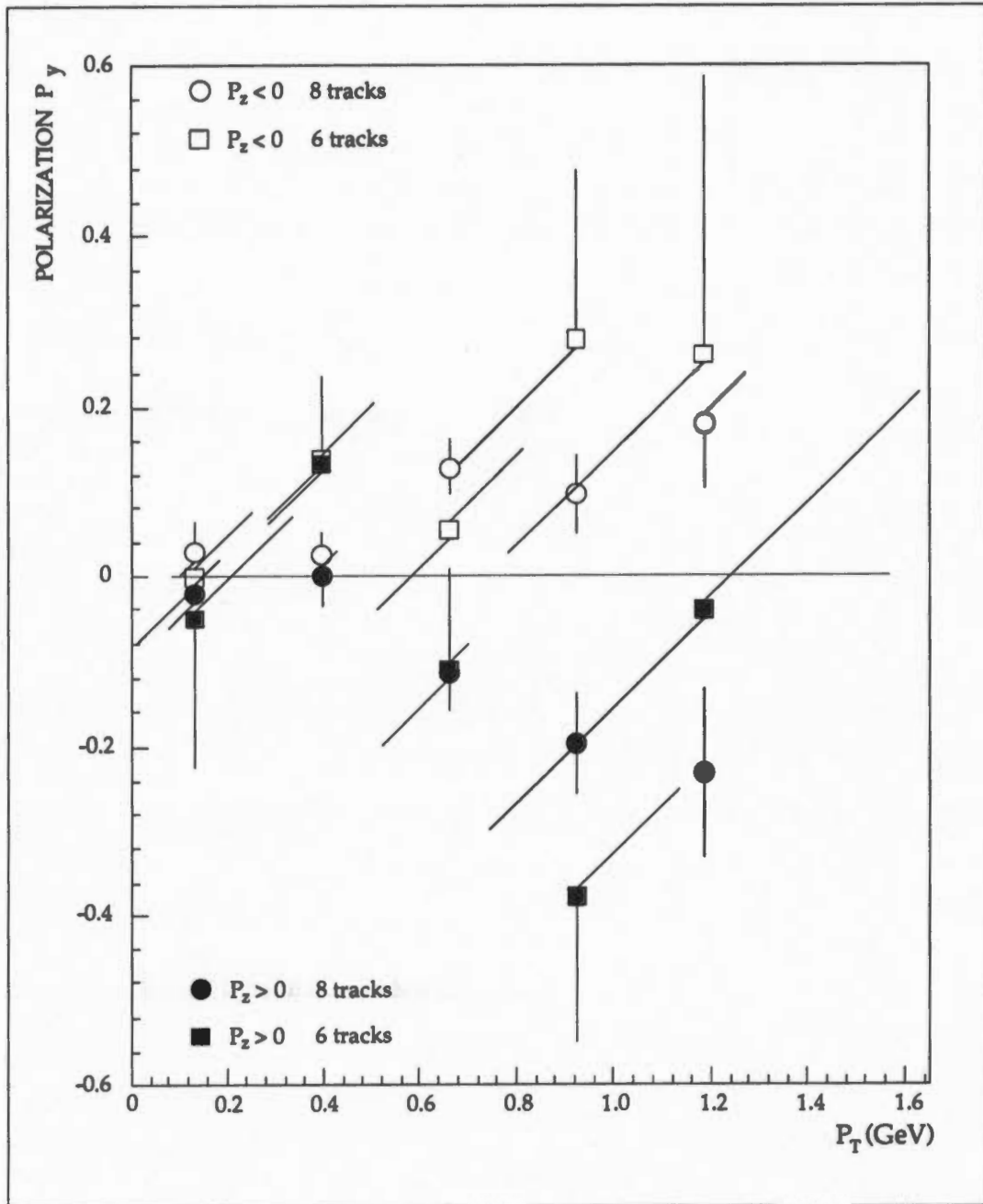
**FIGURE 29.** $\Lambda^0$ polarization, for the 6 track final state sample. We compare with that from the 8 track final state sample.

143
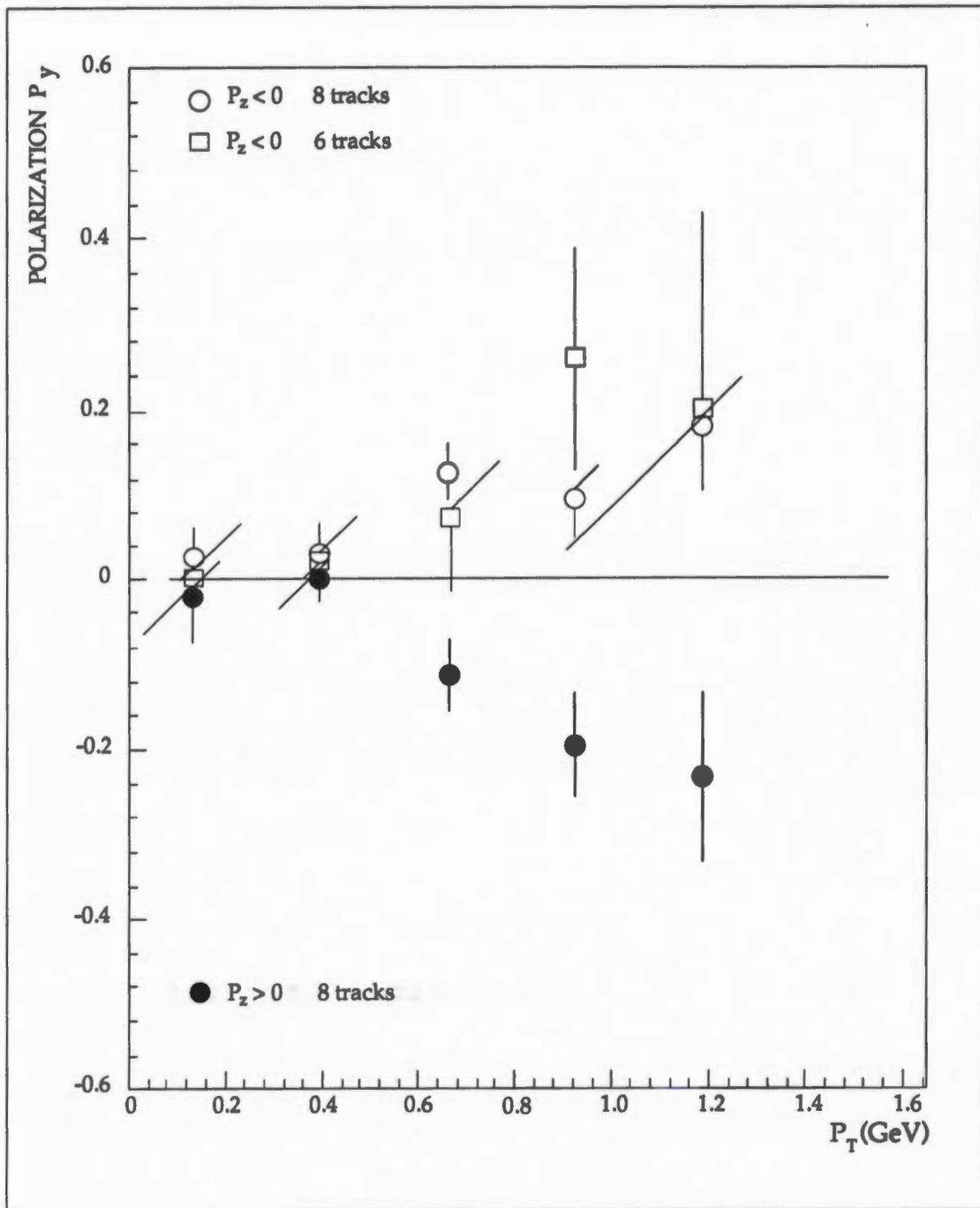
**FIGURE 30.** $\Lambda^0$ polarization, for the 6 track final state sample, combining both hemispheres. We compare with that from the 8 track final state sample.
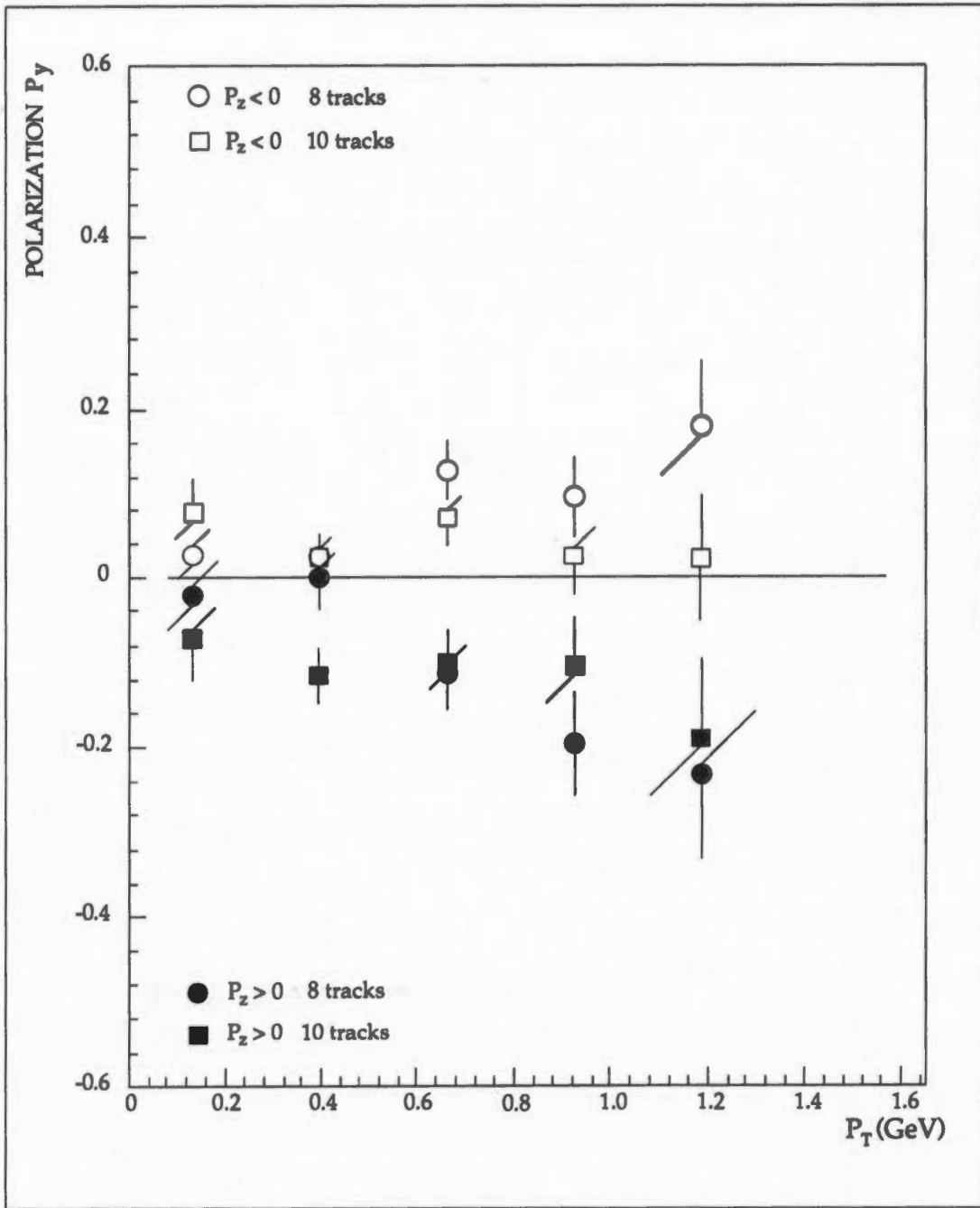
**FIGURE 31.** $\Lambda^0$ polarization, for the 10 track final state sample. We compare with that from the 8 track final state sample.
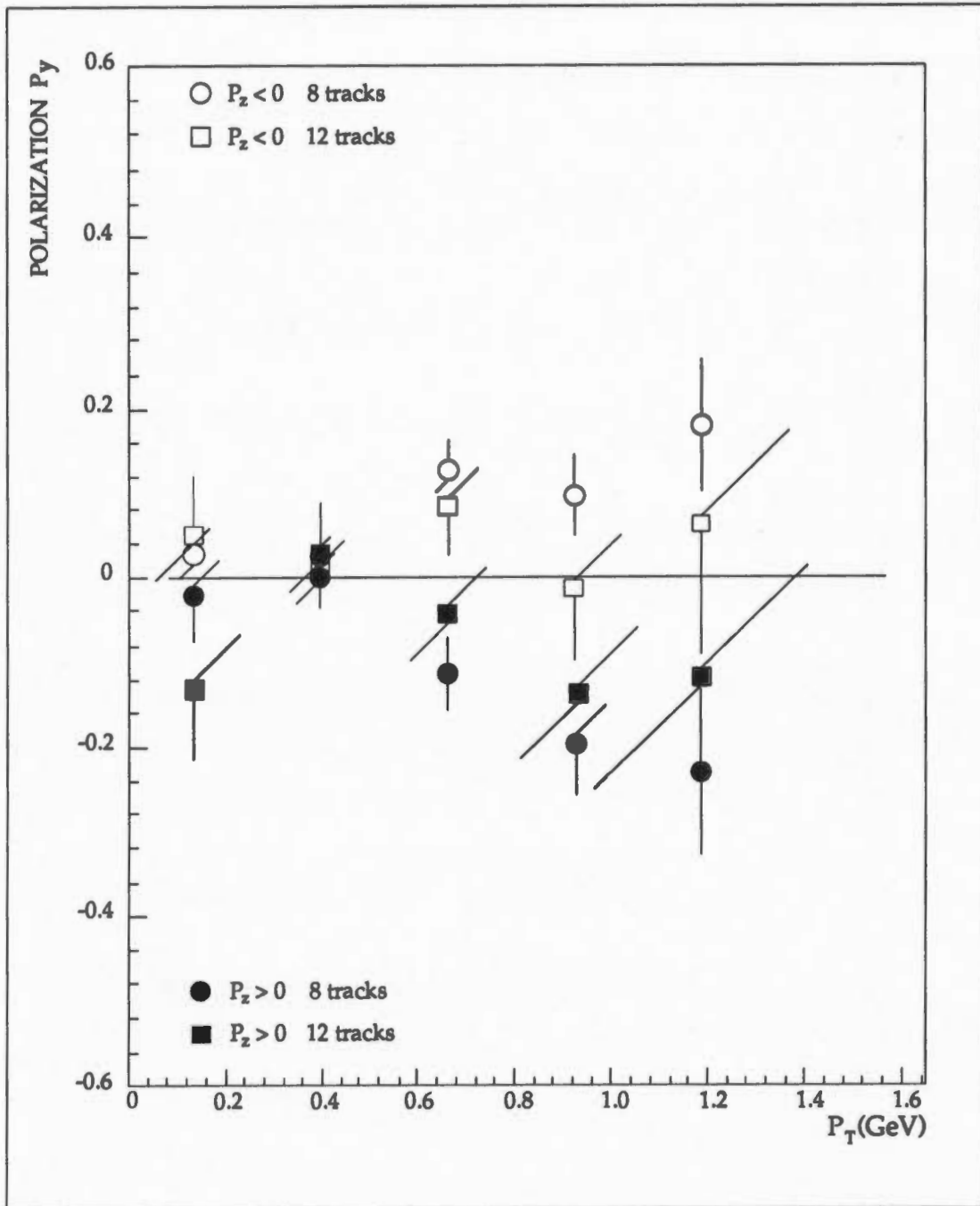
**FIGURE 32.** $\Lambda^0$ polarization, for the 12 track final state sample. We compare with that from the 8 track final state sample.

146
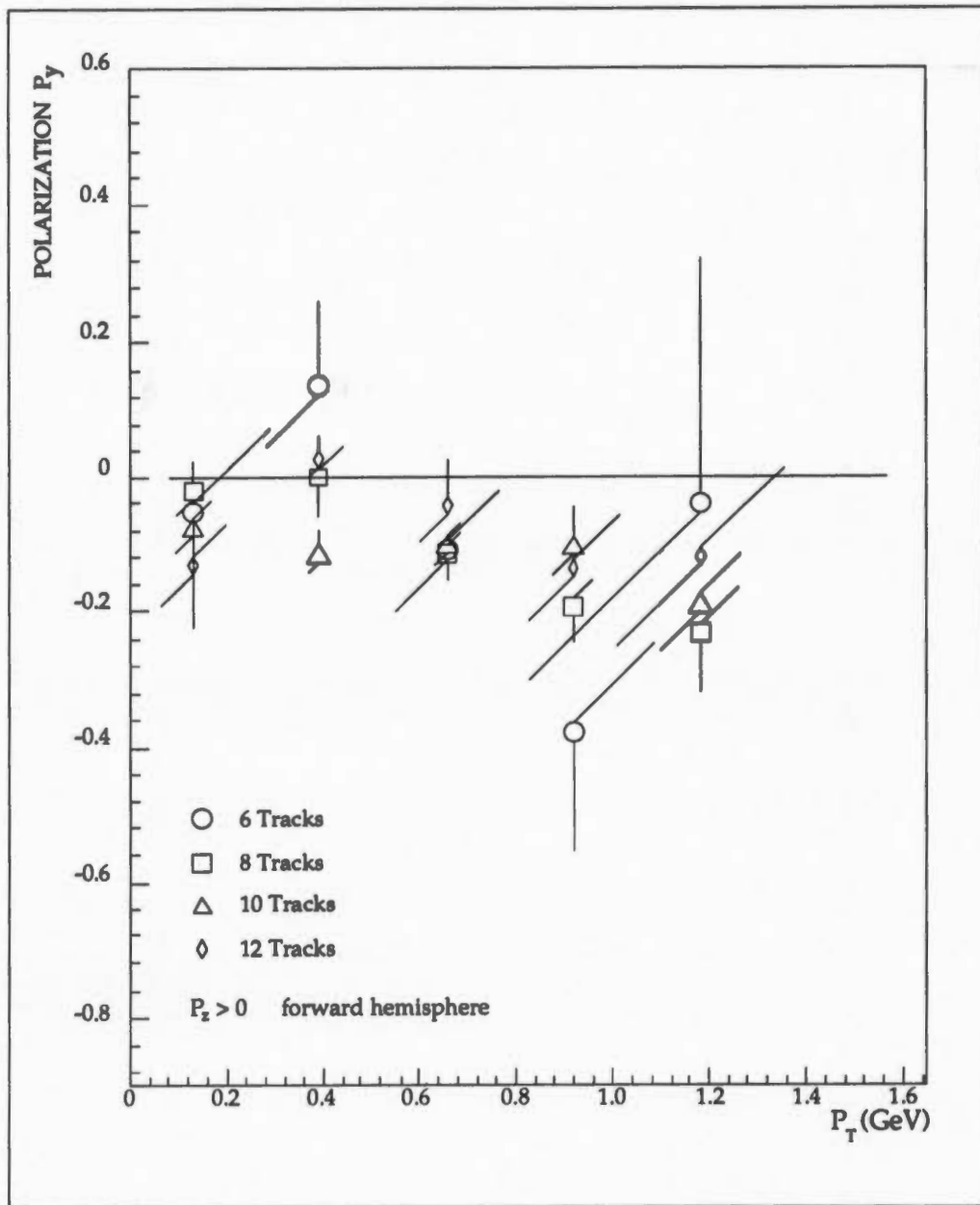
**FIGURE 33.** Comparison between $P_z > 0$ $\Lambda^0$ polarization for the 6 track, the 8 track, the 10 track, and the 12 track final state samples.
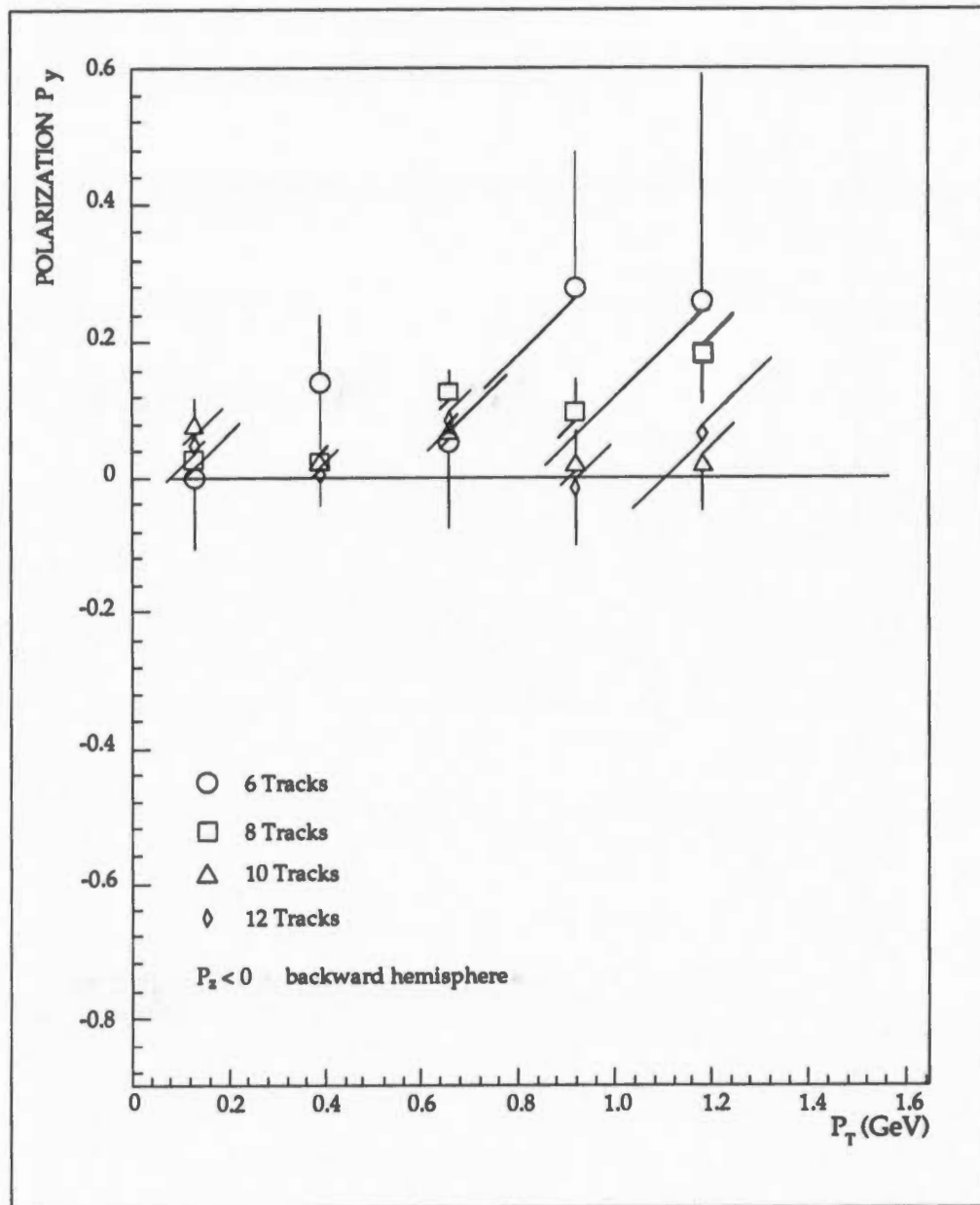
**FIGURE 34.** Comparison between $P_z < 0$ $\Lambda^0$ polarization for the 6 track, the 8 track, the 10 track, and the 12 track final state samples.

148
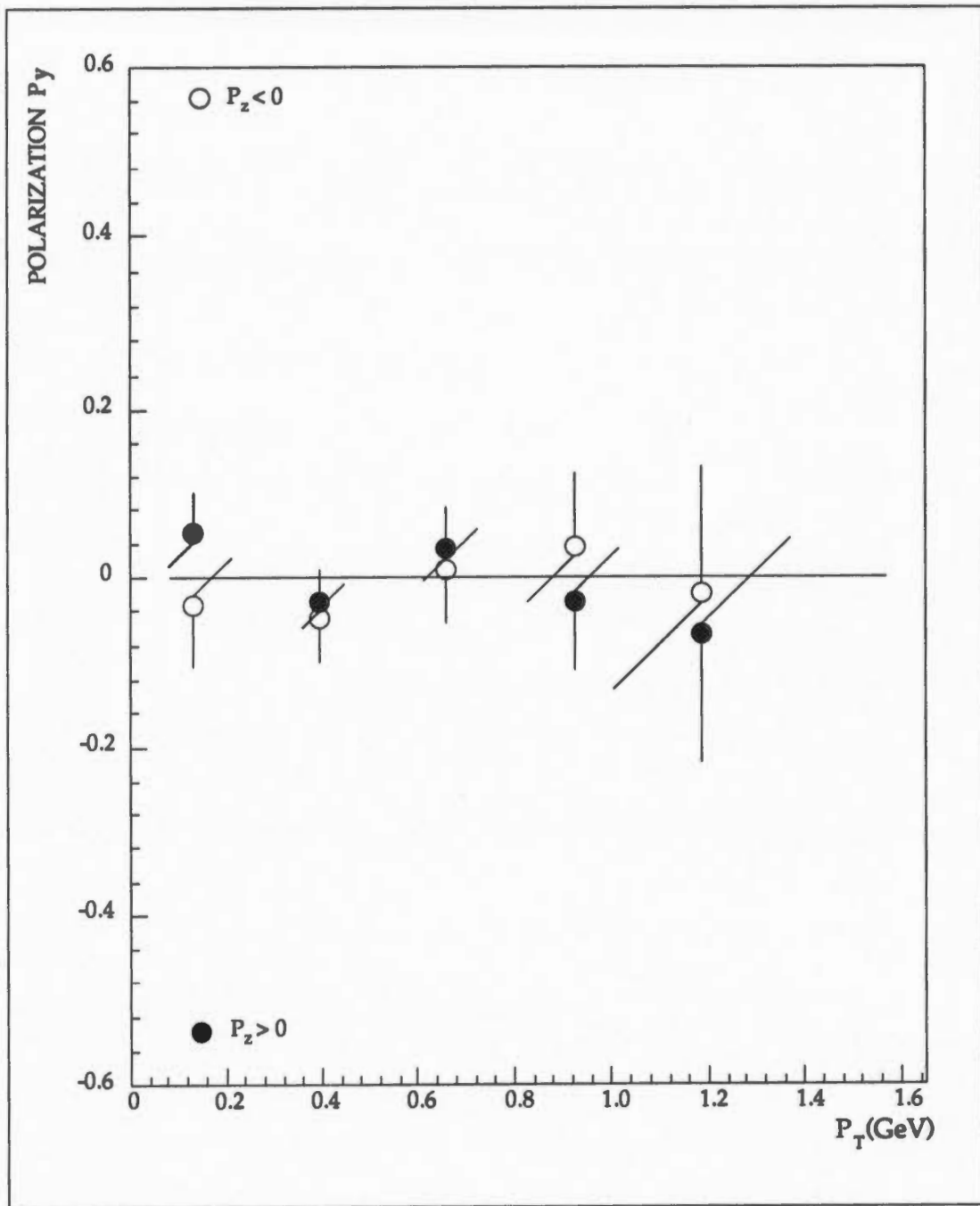
**FIGURE 35.** $K_s^0$ polarization, for the 8 track final state sample.
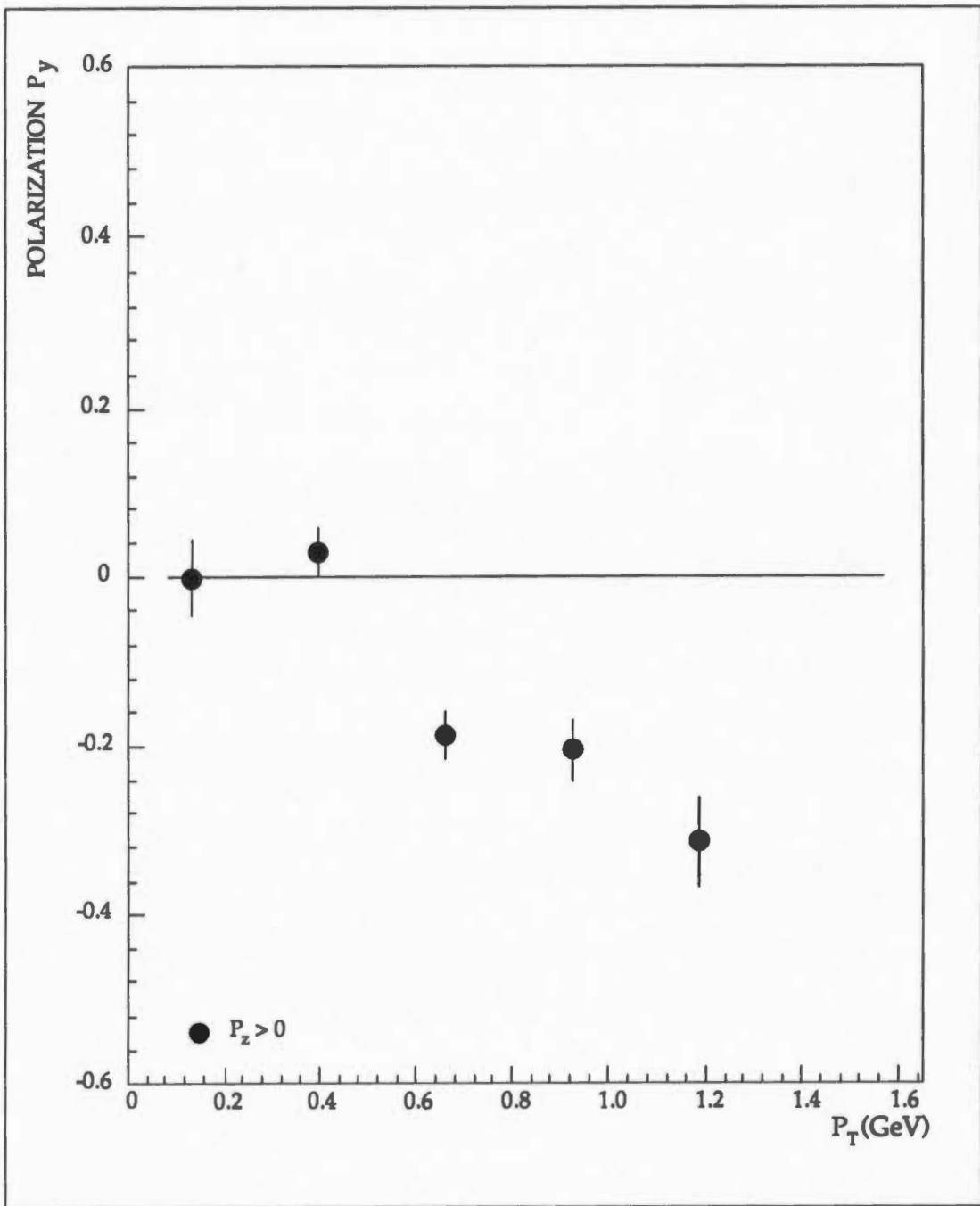
**FIGURE 36.** $\Lambda^0$ polarization, for the Monte Carlo 8 track final state sample.
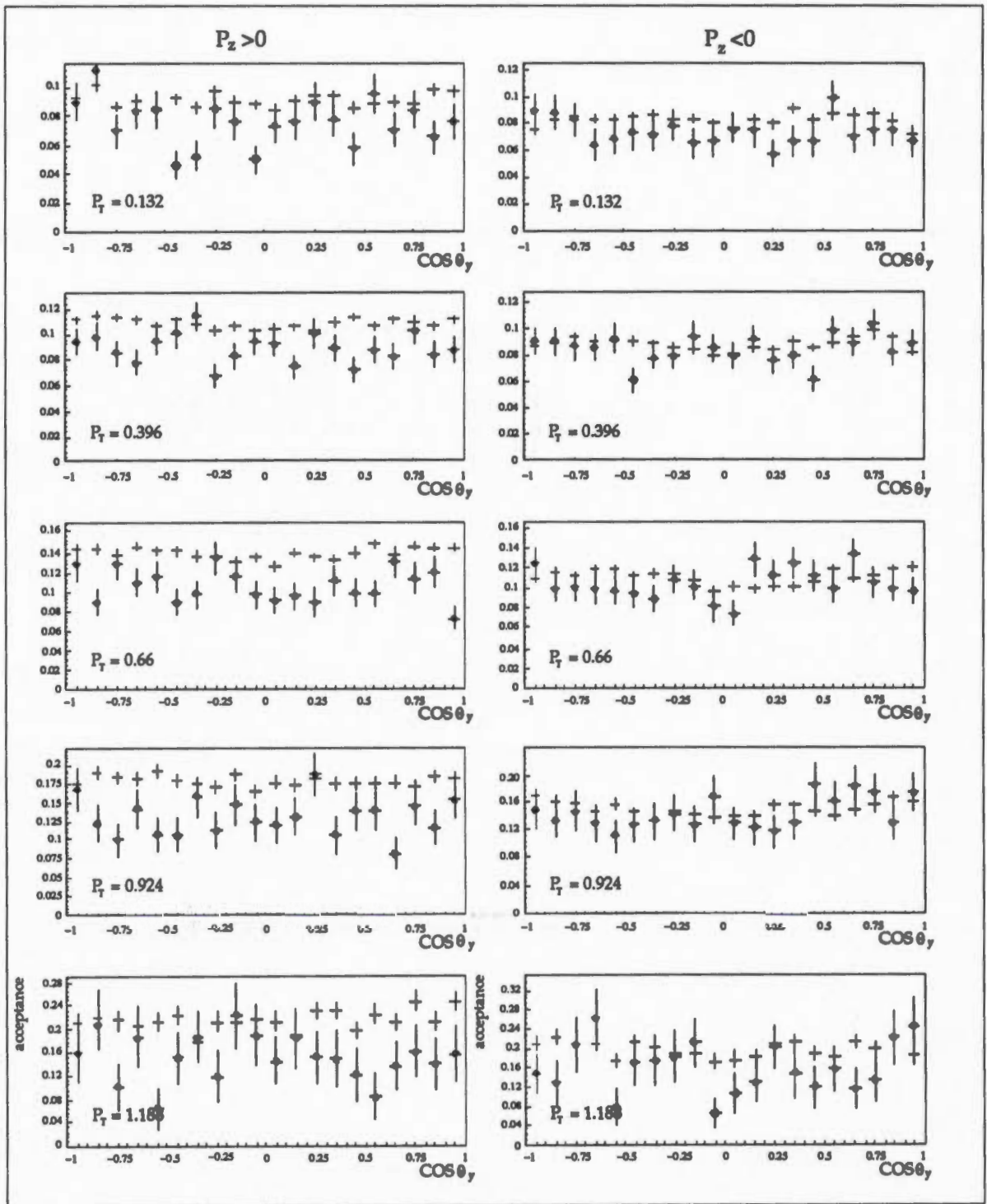
**FIGURE 37.** Acceptance $\cos\theta_y$ distributions, for the 8 track final state sample. ✦ - SS sample, + - BS sample.
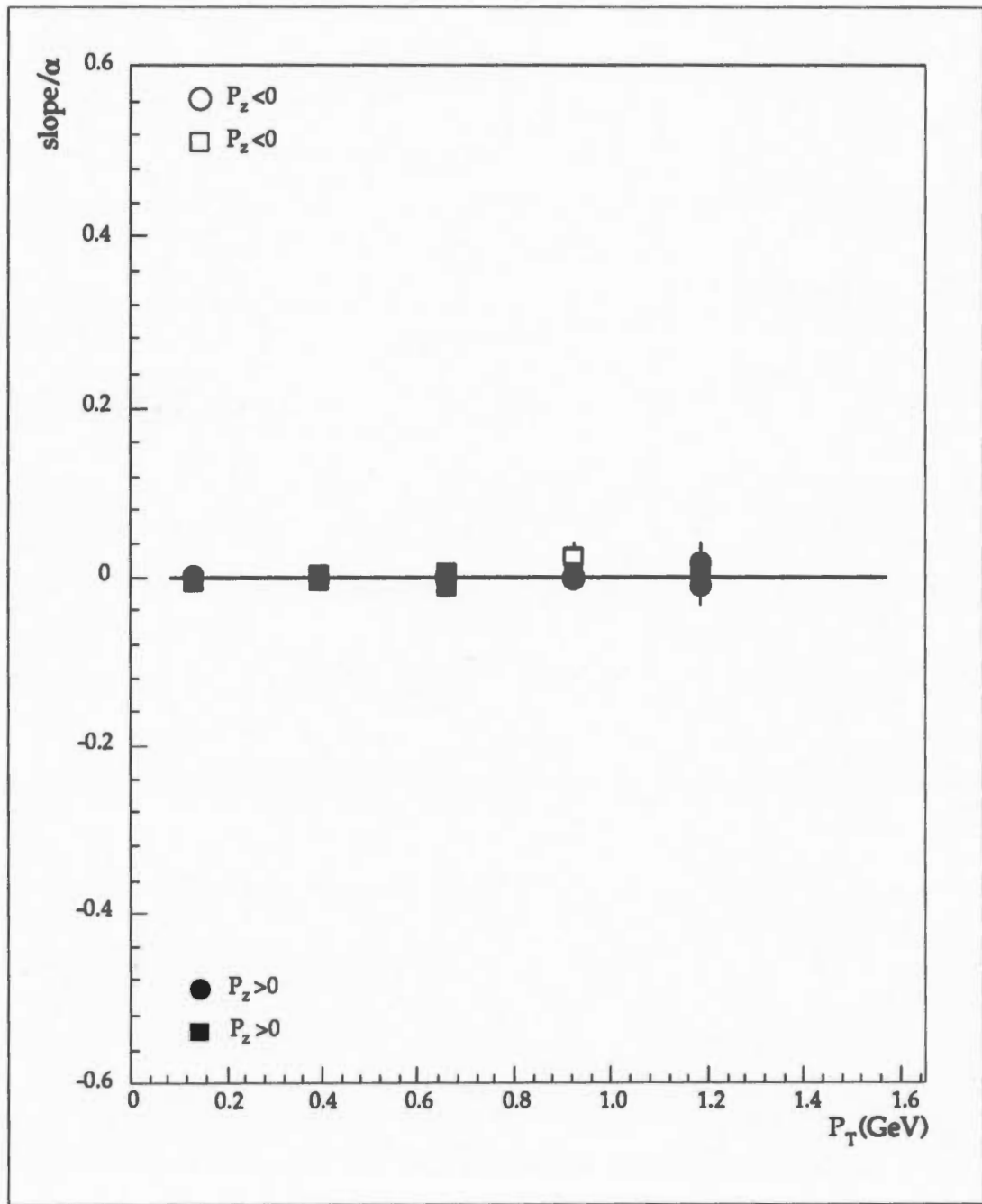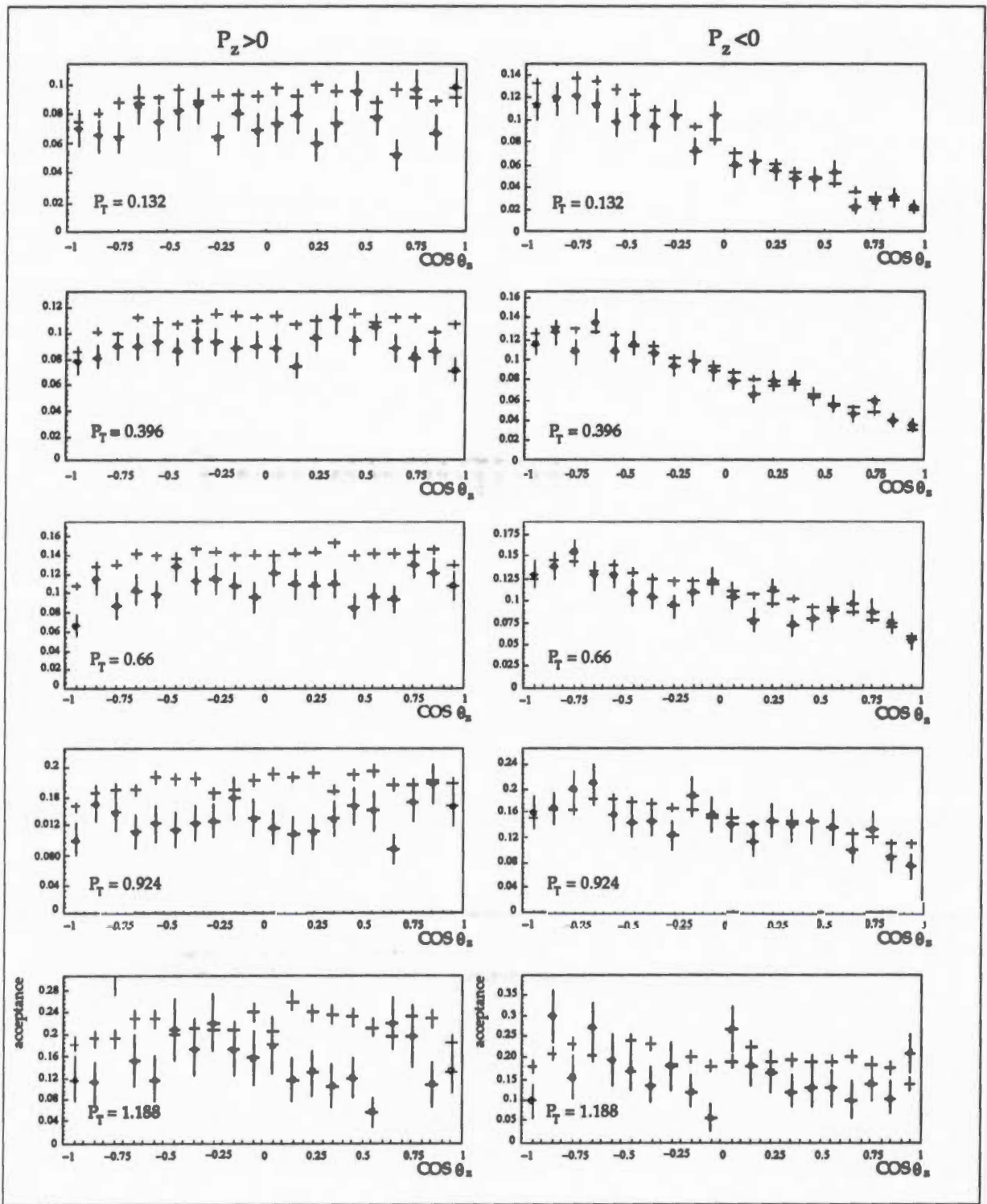
**FIGURE 38.** Comparison between the *slope*/α's for the straight line fits of the 8 track BS and SS samples.
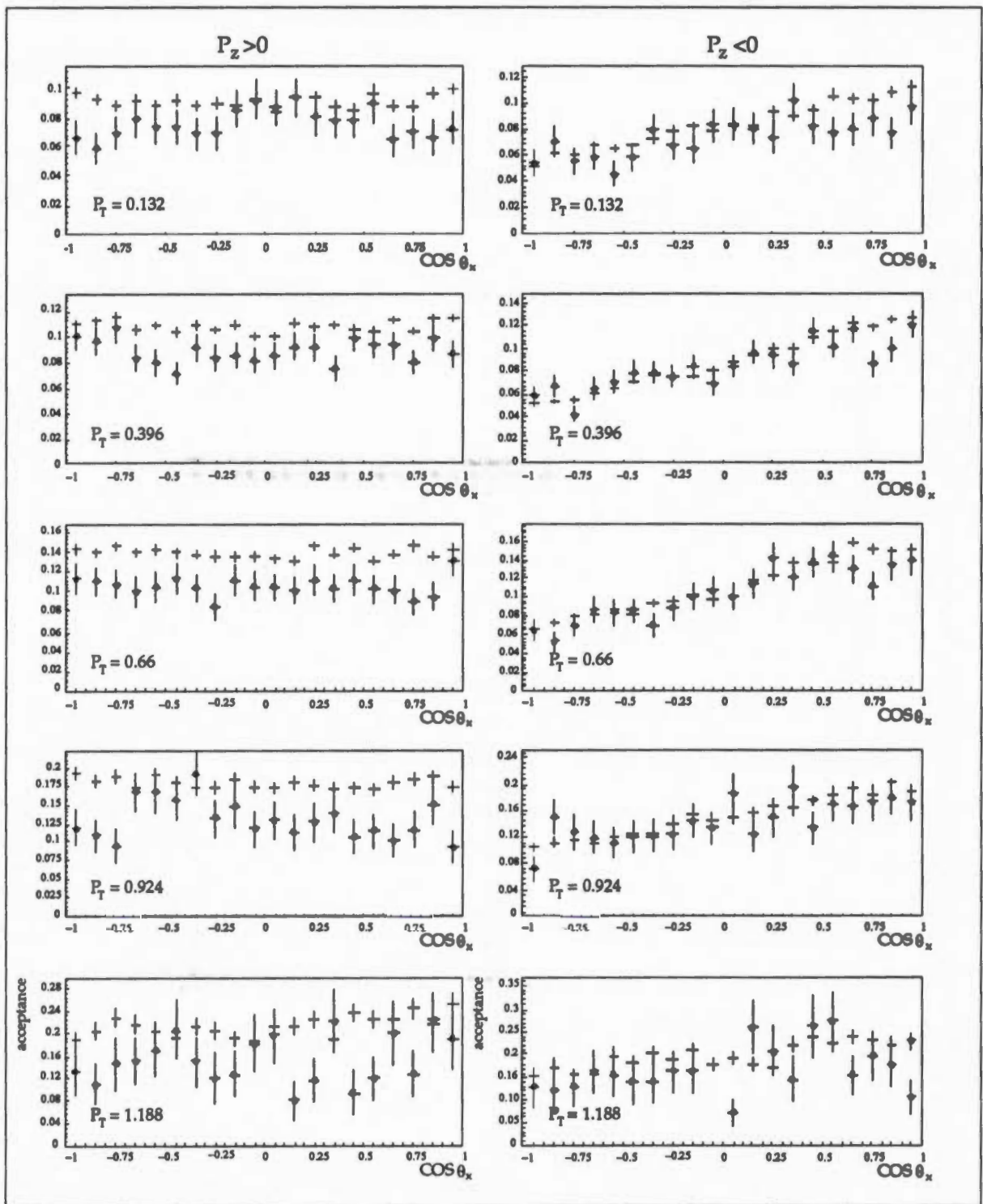
**FIGURE 39.** Acceptance $\cos\theta_x$ distributions, for the 8 track final state sample. ✦ - SS sample, ✛ - BS sample.

**FIGURE 40.** Acceptance $\cos\theta_z$ distributions, for the 8 track final state sample. ✦ - SS sample, ╂ - BS sample.
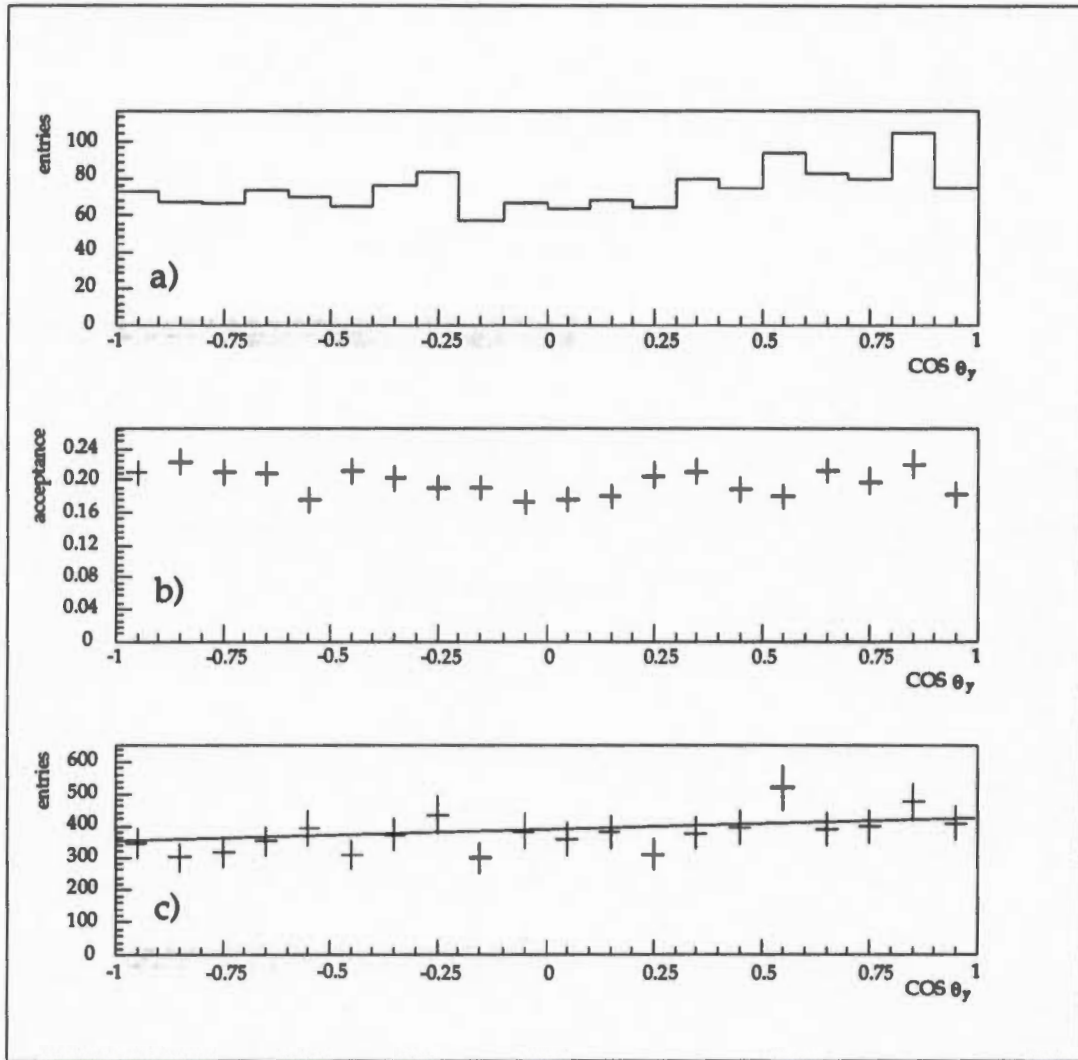
**FIGURE 41.** An example of $\cos\theta_y$ distribution, from the 8 track final state sample, in the backward hemisphere and $P_T = 1.188$ bin. a) raw distribution, b) acceptance distribution, and c) corrected distribution, (the straight line fit is shown).
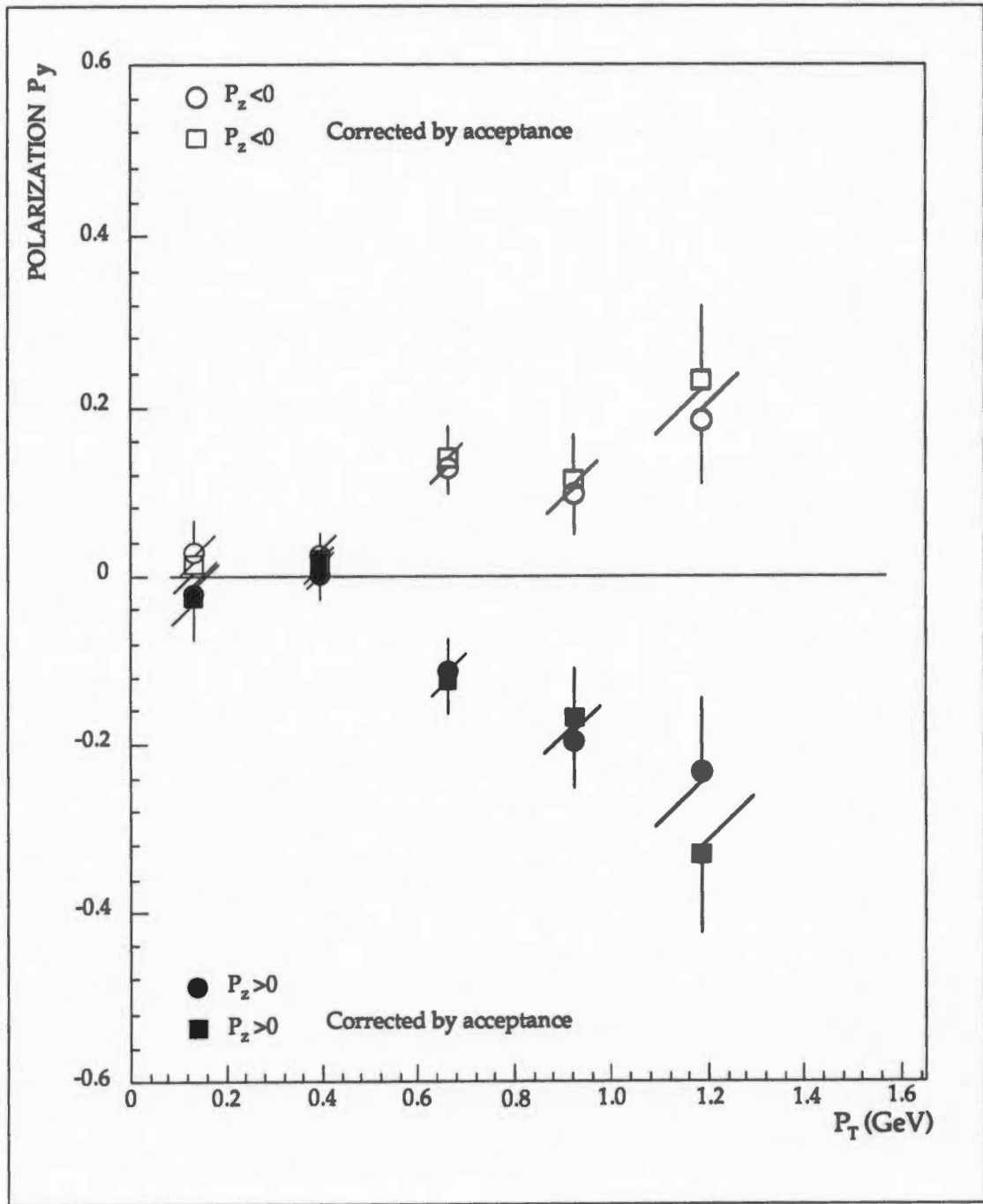
155

**FIGURE 42.** $\Lambda^0$ polarization, for the 8 track final state sample, not corrected by acceptance, compared with corrected one.
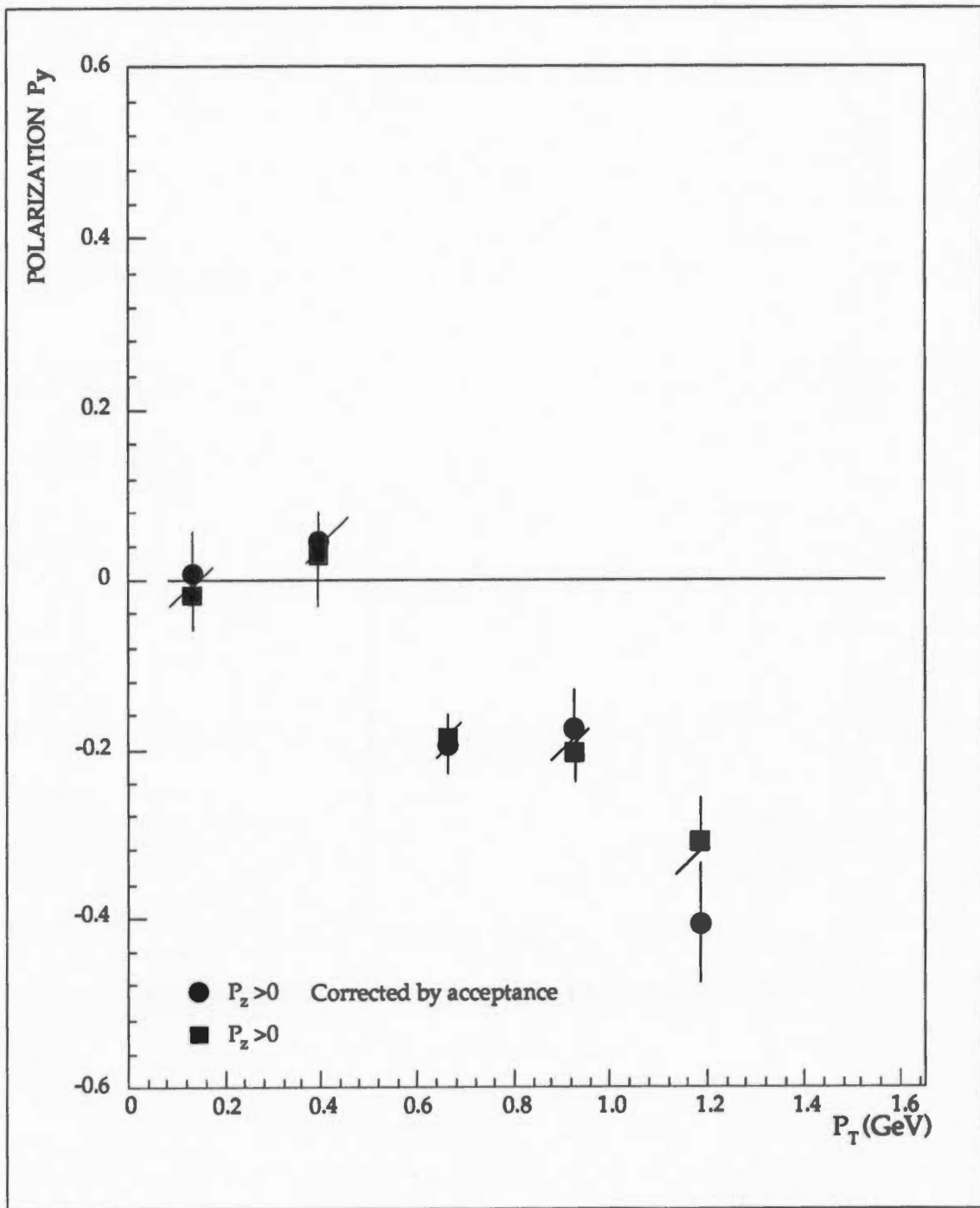
**FIGURE 43.** $\Lambda^0$ polarization, for the Monte Carlo 8 track final state sample, not corrected by acceptance, compared with corrected one.